CONTRIBUTED PAPER

Radar-Based Monitoring of Vital Signs: A Tutorial Overview

This article offers a tutorial overview of radar-based monitoring of vital signs while providing some essential tips for its use in a research laboratory.

By Giacomo Paterniani, Daria Sgreccia, Alessandro Davoli, *Graduate Student Member IEEE*, Giorgio Guerzoni, Pasquale Di Viesti, *Graduate Student Member IEEE*, Anna Chiara Valenti, Marco Vitolo, Giorgio M. Vitetta, *Senior Member IEEE*, and Giuseppe Boriani

ABSTRACT | In the last years, substantial attention has been paid to the use of radar systems in health monitoring, due to the availability of both low-cost radar devices and computationally efficient algorithms for processing their measurements. In this article, a tutorial overview of radar-based monitoring of vital signs is provided. More specifically, we first focus on the available radar technologies and the signal processing algorithms developed for the estimation of vital signs. Then, we provide some useful guidelines that should be followed in the selection of radar devices for vital sign monitoring and in their use. Finally, we illustrate various specific applications of radar systems to health monitoring and some relevant research trends in this field.

KEYWORDS | Health monitoring; multiple-input–multiple-output; radar; signal processing; vital signs.

Manuscript received 21 February 2022; revised 11 November 2022 and 3 February 2023; accepted 7 February 2023. Date of publication 22 February 2023; date of current version 7 March 2023. This work was supported by the University of Modena and Reggio Emilia under its Mission Oriented FAR program. *(Corresponding author: Giorgio M. Vitetta.)*
This research has involved only healthy adult volunteers; a consent has been acquired from each of them.
Giacomo Paterniani, **Alessandro Davoli**, **Giorgio Guerzoni**, **Pasquale Di Viesti**, and **Giorgio M. Vitetta** are with the Department of Engineering "E. Ferrari," University of Modena and Reggio Emilia, 41125 Modena, Italy, and also with the Consorzio Nazionale Interuniversitario per le Telecomunicazioni (CNIT), 43124 Parma, Italy (e-mail: giacomo.paterniani@unimore.it; alessandro.davoli@unimore.it; giorgio.guerzoni@unimore.it; pasquale.diviesti@unimore.it; giorgio.vitetta@unimore.it).
Daria Sgreccia, **Anna Chiara Valenti**, **Marco Vitolo**, and **Giuseppe Boriani** are with the Cardiology Division, Department of Biomedical, Metabolic and Neural Sciences, University of Modena and Reggio Emilia, 41125 Modena, Italy (e-mail: daria.sgreccia@gmail.com; annachiara.valenti@unimore.it; marco.vitolo@unimore.it; giuseppe.boriani@unimore.it).

Digital Object Identifier 10.1109/JPROC.2023.3244362

NOMENCLATURE

ADC	Analog-to-digital converter.
AD	Arctangent demodulation.
ANC	Adaptive noise cancellation.
API	Application programming interface.
ASIC	Application-specific integrated circuit.
AWGN	Additive white Gaussian noise.
BR	Breath rate.
BPF	Bandpass filtering.
CFAR	Constant false alarm rate.
CV	Correlation of variation.
CNN	Convolutional neural network.
CSD	Complex signal demodulation.
CPU	Central processing unit.
CW	Continuous wave.
CWT	Continuous wavelet transform.
DACM	Differentiate and cross-multiply.
DC	Direct current.
DFT	Discrete Fourier transform.
DSP	Digital signal processor.
DL	Deep learning.
DOA	Direction of arrival.
DT	Decision tree.
ECG	Electrocardiogram.
EMD	Empirical mode decomposition.
FMCW	Frequency-modulated continuous wave.
FOV	Field of view.
FPGA	Field-programmable gate array.
FFT	Fast Fourier transform.
GPU	Graphic processing unit.
HR	Heart rate.
HRV	Heart rate variability.

IDFT	Inverse DFT.
IFFT	Inverse FFT.
IMF	Intrinsic mode function.
IR-UWB	Impulse radio ultrawideband.
ISM	Industrial, scientific, and medical.
IWR	Industrial millimeter-wave radar.
K-NN	K-nearest neighbor.
LB	Learning based.
LDA	Linear discriminant analysis.
LNA	Low noise amplifier.
LO	Local oscillator.
LS	Least square.
LSTM	Long short-term memory.
MAE	Mean absolute error.
MEMS	Micro-electromechanical system.
MF	Matched filter.
MIMO	Multiple-input–multiple-output.
ML	Machine learning.
MMIC	Monolithic microwave integrated circuit.
NN	Normal to normal.
P2G	Position to go.
PA	Power amplifier.
PAE	Peak absolute error.
PCR	Pulsed coherence radar.
PRI	Pulse repetition interval.
RADAR	Radio detection and ranging.
RBM	Random body movement.
RF	Radio frequency.
RHS	Right-hand side.
RMSE	Root-mean-square error.
RMSSD	Root-mean-square successive difference.
RX	Receive.
SDNN	Standard deviation of normal to normal.
SFCW	Stepped frequency continuous wave.
STFT	Short-time Fourier transform.
SISO	Single-input–single-output.
SNR	Signal-to-noise ratio.
SVM	Support vector machine.
TDM	Time-division multiplexing.
TI	Texas Instrument.
TX	Transmit.
ULA	Uniform linear array.
URA	Uniform rectangular array.
UWB	Ultrawideband.
VA	Virtual antenna.
VGA	Voltage gain amplifier.
VCO	Voltage-controlled oscillator.
VHSIC	Very high-speed integrated circuit.
TRI	Triangular index.

I. INTRODUCTION

Monitoring human vital signs, such heart and respiration rates, represents a routine practice to detect patient deterioration. Changes in vital signs can reveal the existence of serious medical problems; for this reason, early identification of these changes can improve survival rates in several conditions [1]. Vital signs monitoring is often accomplished by means of wearable health devices [2]; this is due to the fact that these devices enable continuous monitoring during daily activities. However, in various situations, such as in the case of infected patients or of patients suffering from mental illness or affected by severe burns or injuries, the use of wearable sensors is not possible or recommended. In such cases, the use of noncontact monitoring devices, such as radar systems, can help healthcare professionals by providing critical information about patient state [3]. The application of radar devices to this field and, in particular, to the estimation of heart and respiration rates has become an active research area in recent years [4], [5], [6], [7]. Actually, the first experimental results in this field date back to 1975, when the use of short-range radar technology was proposed to noninvasively acquire respiratory information by comparing a microwave signal with its echo reflected from the chest of a patient [8], [9]. In the following years, the possibility of employing radar systems for the wireless detection of the physiological movements due to both heartbeat and respiration has been shown [10], [11], [12], [13]. This has motivated the investigation of the use of this technology in a number of medical applications, including adult and neonatal sleep monitoring [14], [15], [16], disaster medicine (e.g., in the detection of human vital signs under rubbles after earthquakes [17]), and lung cancer radiotherapy [18].

In the last two decades, a few review articles about radar-based monitoring of vital signs have been published [13], [19], [20], [21], [22], [23], [24]; however, they have a limited scope since they concern the use of specific technologies. In fact, on the one hand, works [13], [19], [20], [21], and [25] focus on CW Doppler radars, UWB, and radars equipped with a single TX/RX antenna (i.e., SISO and radars). On the other hand, work [22] takes into consideration radars equipped with antenna arrays (i.e., MIMO and radars) and illustrates the advantages they offer with respect to their SISO counterparts. This has motivated the writing of this article, which aims at offering a tutorial overview of radar-based monitoring of vital signs and at providing some essential tips for its use in a research laboratory. More specifically, in the remaining part of this article, we first provide essential information about radar-based monitoring, cardiovascular and respiration physiology, and the modeling of chest displacement. Then, we focus on the available radar technologies and describe various radar architectures and signal processing methods developed for radar-based estimation of vital signs; in our description, all the available options are taken into consideration, and their pros and cons are illustrated. This is followed by various technical considerations, formulated in the light of the experience acquired in our experimental activities on radar-based monitoring, and by the analysis of some numerical results based on the measurements we acquired through different radar devices; our considerations concern the essential technical requirements that radar devices employed in this field should have and

some essential guidelines to be followed in conducting experimental campaigns. The study of all this allows us to lay the foundations for understanding specific applications of radar-based monitoring and relevant research trends in this field.

This article is organized as follows. In Section II, the basic principles, challenges, and objectives of radar-based monitoring of vital signs are illustrated. In Section III, the physiological fundamentals of human cardiovascular and respiration activities are provided and simple mathematical models describing the dynamics of chest displacement due to these activities are described. Section IV is devoted to the four radar technologies employed in radar-based monitoring of vital signs, and to SISO and MIMO radar architectures; for each architecture, simple mathematical models are provided for the samples of the baseband signal received in the presence of a single point target. An overview of the most important deterministic and LB signal processing techniques employed for vital signs monitoring is offered in Section V. In Section VI, we illustrate some basic guidelines to be followed in conducting experimental activities in the considered field, analyze the problem of extracting hear rate from radar measurements, and comment on the assessment of estimation accuracy. The applications of the considered radar-based techniques for vital signs monitoring to heart and BR estimation, heart sound monitoring, and HR variability estimation are discussed in Section VII, whereas current research trends on radar-based monitoring of vital signs are illustrated in Section VIII. Finally, some conclusions are offered in Section IX.

II. RADARS FOR VITAL SIGNS MONITORING: BASIC PRINCIPLES, OBJECTIVES, AND CHALLENGES

A system for RADAR (i.e., briefly, a radar system) is an electronic system designed to estimate the frontal distance (together with the angular coordinates, if an MIMO system is employed) and/or the velocity of objects (called targets) that, due to their electrical conductivity, are able to reflect back the electromagnetic waves it generates. Any radar system consists of a transmitter and a receiver that, in the applications considered in this article, are integrated in the same electronic device. The transmitter generates radio waves with known properties and radiates them along a predetermined direction using a single TX antenna or multiple TX antennas (i.e., an antenna array), whereas the receiver captures the waves reflected back by the abovementioned targets.

The measurement of the distance (i.e., of the range) of any target from a given radar system is based on the estimation of the propagation delay of the received waves, whereas that of its velocity on some structural changes in such waves; for instance, if a target is approaching the radar or is moving away from it, a variation in the frequency of the received radio waves is observed because of the Doppler effect. Target range and velocity can be estimated by radar systems equipped with a single TX and single RX antenna. The measurement of the angular coordinates of any target requires, instead, the availability of at least two RX antennas, that is of an antenna array at the RX side, since it is equivalent to the estimation of the DOA of the electromagnetic waves impinging on the radar receiver; note that, in general, the use of a larger number of antenna elements forming the RX array results in a better angular resolution, i.e., in more accurate estimates of the angular coordinates of the surrounding targets (and, consequently, in more detailed radar images). Modern radars, and especially those employed for vital signs monitoring, are quite small and compact in size[1] since they operate at very high frequencies and, in particular, in the microwave spectrum.[2] The basic components of these devices are a digital control board and an RF front end, whose implementation is usually based on an MMIC and small-sized patch antennas [26]. If microwave frequencies are used, small-size TX and RX antennas are implemented and electromagnetic signals characterized by a very large bandwidth and small wavelength are radiated; the last features make it possible to achieve an excellent range solution and detect small movements.

Radar-based monitoring of vital signs is based on the idea that the chest wall of human bodies reflects the electromagnetic waves generated by a radar placed in front of it and that its quasi-periodic vibrations, resulting from respiration and heartbeat, modulate such waves. Therefore, in principle, essential information about vital signs, i.e., HR and BR, can be extracted from the reflected electromagnetic waves [27], [28], [29] and a fundamental objective, namely, contactless monitoring of vital signs, can be achieved. Note also that, compared with traditional methods, such as pneumotachography and electrocardiography, radar systems make continuous and timely BR and HR monitoring possible without entailing an additional work load for nurses. For these reasons, radars represent a favorable option for hospital monitoring, especially in the case of severe burn or infectious disease patients, sudden infant death syndrome monitoring, sleep apnea monitoring, elderly home healthcare, and psychology studies. Moreover, radar signals can be processed to extract more refined medical information and, in particular, to detect anomalous alterations in the sequence of heart beats.

[1]The size of a commercial MIMO radar device for vital signs monitoring mainly depends on that of its RF front end, which contains all its RF components and, in particular, its TX/RX antenna arrays. The distance between adjacent antennas of the same array is typically equal to half the transmission wavelength, i.e., to approximately 2 mm at 77 GHz. The average front-end area of MIMO radars operating at that frequency and equipped with tens of TX/RX patch antennas is on the order of 100 cm^2 (corresponding to the area of a square whose side is 10 cm; see, e.g., Fig. 17). It is also worth mentioning that the front-end area of SISO radar devices is substantially smaller, being on the order of 4 cm^2 (see, e.g., Fig. 18).

[2]This portion of electromagnetic spectrum is often defined as the interval of frequencies ranging from 1 to 100 GHz (corresponding to wavelengths between 0.3 m and 3 mm).

Even if the usefulness of radar systems in vital signs monitoring is now globally recognized and a wide literature about such systems is available, various challenges concerning signal processing techniques for vital signs extraction are still open in this research field; here, we limit to mention the following.

1) *The estimation of HR:* As illustrated in Section III-B, the vibrations due to heartbeat are significantly weaker than those originating from respiration. For this reason, the contribution of the first phenomenon to the radar signal may be hidden by that related to the second (and much stronger) one. This makes the task of estimating HR much harder than that of estimating BR; additional details about this issue can be found in Sections VI-C and VII-A.
2) *The identification of anomalous alterations of heart beats:* This challenge concerns the possibility of estimating HRV and detecting heart sounds; these issues are discussed in Sections VII-C and VIII-B, respectively.
3) *The simultaneous observation of the vital signs of multiple people:* In principle, MIMO radar systems can be exploited to detect and estimate the vital signs of multiple people located in a restricted area (e.g., in the same room; see Section V-B for further details). However, experimental results supporting the feasibility of this idea and involving a significant number of people are still missing in the technical literature (see, e.g., [22, Table 1, Sec. IV]).

Finally, it is worth mentioning that the experimental results available in the technical literature about radar-based monitoring of vital signs concern heterogeneous radar technologies and that there is not a broad consensus on the best technology to be adopted in real-world systems. For this reason, it is important to analyze the pros and cons of each option available on the market; this issue is discussed in Section IV.

III. PHYSIOLOGICAL FUNDAMENTALS AND MATHEMATICAL MODELING

In this section, we first provide readers with the physiological fundamentals of heart and lung functions. Then, we concentrate on the movements of the chest surface in human beings and illustrate some mathematical models describing them.

A. Basics of Cardiovascular and Respiration Physiology

The human heart is made of two separated systems, called left and right sides. Each side consists of two chambers, namely, an atrium and a ventricle, which are separated and connected by an atrioventricular valve. The main function of the left side is to pump oxygenated blood through the aorta and the other arteries to peripheral tissues and organs. The right side, instead, is in charge of pumping deoxygenated blood through pulmonary arteries to lungs. Each side is connected to arteries through the so-called semilunar valves.

The cardiac cycle consists of a rhythmic sequence of contractions (systoles) and relaxations (diastoles) of the heart; these events occur simultaneously in the left and right sides. During each cardiac cycle, sounds are generated by the action of the heart muscle and the vibrations of the cardiac valves. In the case of a healthy adult heart, two heart sounds are detected. The first one is caused by the contraction of the ventricular muscle during systoles and the closing of atrioventricular valves. The second heart sound, instead, is due to the closure of aortic and pulmonary valves. Hemodynamic properties and HR can be determined by recording heart sounds. As a matter of fact, such sounds can help the physician in the diagnosis of potential cardiovascular diseases [30], [31]. The physiologic HR at rest is 60 up to 100 beats per min (bpm); values below this range (above it) characterize the so-called bradycardia (tachycardia).

A breathing cycle consists of two consecutive phases, known as inspiration and expiration. In the first phase, due to the contraction of the diaphragm and the intercostal muscles, the thoracic volume increases; this results in a subatmospheric pressure that allows air to flow through the airways into the lungs. Then, air oxygen is absorbed into the blood and carbon dioxide is transferred from the blood to the inhaled air through the alveolar-capillary membrane. Expiration, instead, is caused by the elastic recoil of the lungs and relaxing muscles. In this phase, the deoxygenated air can flow out of the lungs by increased pressure [32], [33]. The physiologic BR at rest is 12 up to 25 acts per minute, whereas values below this range (above it) characterize the so-called bradypnea (tachypnoea).

B. Modeling of Chest Displacement

Let us focus now on the problem of modeling the chest displacement of an arbitrary patient. As illustrated in Section III-A, his/her inspiration (expiration) phase produces an expansion (compression) of the thoracic wall. Moreover, the vibrations due to his/her heart beat overlap with the thoracic breathing movement. In principle, the time evolution of both the thoracic breathing movement and the cardiac vibrations of the considered patient can be measured by a radar system placed in front of his/her chest at a fixed distance. In the absence of random and large-scale body movements, the displacement $\Delta R(t)$ of the chest surface measured by the radar system at the instant t can be modeled as [34]

$$\Delta R\left(t\right) \triangleq R\left(t\right) - R_0 = \delta_b\left(t\right) + \delta_h\left(t\right) \tag{1}$$

where $R(t)$ (R_0) is the radar–chest distance at time t (distance in the absence of respiration) and $\delta_b(t)$ ($\delta_h(t)$) represents the breath (heart) contribution to $\Delta R(t)$. It is important to stress that the following conditions hold.

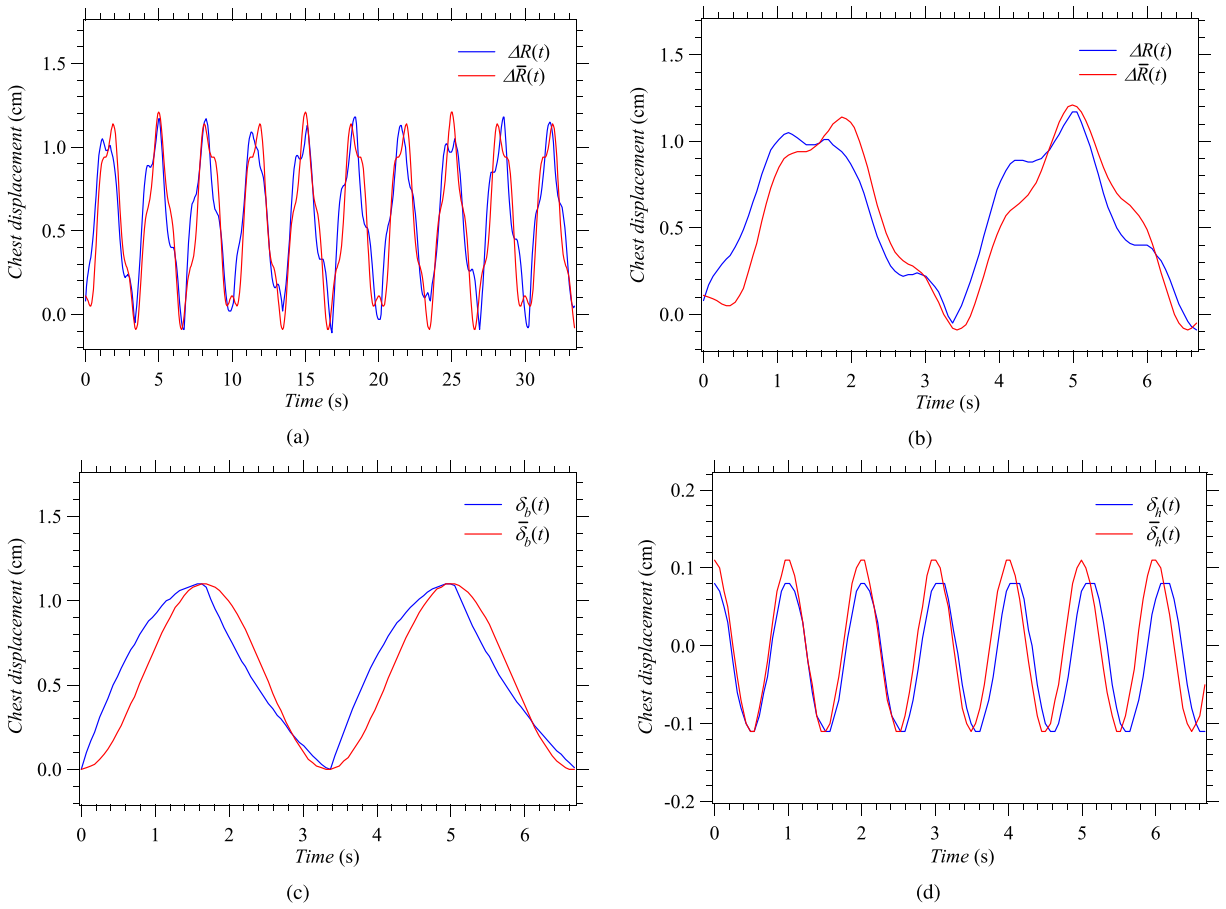

Fig. 1. ***Representation of (a) computer-generated chest displacement (multiple periods of breathing activity are considered), (b) computer-generated chest displacement (a couple of consecutive periods of breathing activity are considered), (c) contributions of breathing activity to the chest displacement shown in (b), and (d) contributions of heart activity to the chest displacement shown in (b). In all these figures, a blue (red) line is used to identify the signals generated based on (1) [see (6)].***

1) The displacement $\delta_b(t)$ ($\delta_h(t)$) is usually assumed to be periodic with period $T_{\rm BR}$ ($T_{\rm HR}$), with $T_{\rm BR} > T_{\rm HR}$.
2) The contribution of $\delta_h(t)$ to the displacement $\Delta R(t)$ is usually small with respect to that due to $\delta_b(t)$; in fact, if $\delta_{b,M}$ ($\delta_{h,M}$) denotes the maximum absolute value of $\delta_b(t)$ ($\delta_h(t)$), it is known that $1 \leq \delta_{b,M} \leq 5$ cm and $1 \leq \delta_{h,M} \leq 9$ mm [35], [36].

A simple mathematical model describing the breath displacement $\delta_b(t)$ within each period has been proposed in [37]. According to this model, the displacement in the inspiration phase is described by the parabolic profile

$$\delta_b(t) = -\frac{\delta_{b,M}}{T_i\,T_e}(t-t_0)^2 + \frac{\delta_{b,M}T_{\rm BR}}{T_i\,T_e}(t-t_0) \qquad (2)$$

with $t \in [t_0, t_0+T_i)$, whereas that in the expiration phase by the exponential profile

$$\delta_b(t) = \frac{\delta_{b,M}\exp\left(-\frac{T_e}{\tau}\right)}{1-\exp\left(-T_e/\tau\right)}\left[\exp\left(-\frac{(t-t_0)-T_{\rm BR}}{\tau}\right)-1\right] \qquad (3)$$

with $t \in [t_0+T_i, t_0+T_{\rm BR})$; here, t_0 is the initial instant of the considered breathing period, T_i (T_e) is the duration of the inspiration (expiration) phase, and τ is the time constant of the expiratory profile; note that $T_{\rm BR} = T_i + T_e$. The displacement due to the cardiac activity, instead, can be modeled as [34]

$$\delta_h(t) = \delta_{h,M}\cos\left(w_1(t-t_1)+\gamma_h(t)\right) \cdot \exp\left(-\frac{\left((t-t_1)-a_2\right)^2}{a_3}\right) \qquad (4)$$

with

$$\gamma_h(t) = a_1\sin\left(w_2(t-t_1)\right) \qquad (5)$$

and $t \in [t_1, t_1+T_{\rm HR})$; here, t_1 is the initial instant of the considered heartbeat, and $\{a_k;\ k=1,2,3\}$ and $\{w_l;\ l=1 \text{ and } 2\}$ are tunable and fixed parameters, respectively. Note that the function $\gamma_h(t)$ is periodic but can be easily modified to account for HRV, i.e., for the changes in the time interval between consecutive beats.[3]

The minimum and maximum values of all the parameters appearing in (2)–(5) are listed in the second row and

[3] Additional details about HRV are provided in Section VIII-B.

the third row, respectively, of Table 1; note that, given T_{HR} and T_{BR}, w_1 and w_2 can be computed as $w_1 = 2\pi/T_{\mathrm{HR}}$ and $w_2 = 2\pi/T_{\mathrm{BR}}$, respectively, and both parameters are expressed in rad/s.

The chest displacement resulting from the mathematical model expressed by (1)–(4), given the values of its parameters[4] listed in the fourth row of Table 1, is exemplified in Fig. 1, where the contributions due to breathing and cardiac activities are also shown for a couple of consecutive periods of breathing activity [see Fig. 1(a) and (d)]. Note that, in generating these numerical results, $t_0 = (k_b - 1)T_{\mathrm{BR}}$ (with $k_b = 0, 1, \ldots, N_b - 1$ and $N_b = \lfloor T_F/T_{\mathrm{BR}} \rfloor$) and $t_1 = (k_h - 1)T_{\mathrm{HR}}$) (with $k_h = 0, 1, \ldots, N_h - 1$ and $N_h = \lfloor T_F/T_{\mathrm{HR}} \rfloor$) have been selected, where T_F is the duration of the whole observation interval; moreover, the values adopted for the model parameters have been selected based on the results obtained in our experimental campaign.

Although the models illustrated above are accurate, a simpler representation of the heart and breathing profile has been adopted by various researchers [28], [38], [39]. More specifically, if T_i is assumed to be equal T_e, the approximate model

$$\Delta R(t) \approx \Delta \bar{R}(t) = \bar{\delta}_b(t) + \bar{\delta}_h(t) \tag{6}$$

with

$$\bar{\delta}_b(t) \triangleq \frac{\delta_{b,M}}{2}\left[1 - \cos(w_b t)\right] \tag{7}$$

and

$$\bar{\delta}_h(t) \triangleq \delta_{h,M}\cos(w_h t) \tag{8}$$

can be employed in place of that expressed by (1); here, $w_b = 2\pi/T_{\mathrm{BR}}$ ($w_h = 2\pi/T_{\mathrm{HR}}$) represents the HR (BR). An example of chest displacement generated according to (6) is shown in Fig. 1, where the contributions due to breathing and cardiac activities are also shown. From this figure, it can be easily inferred that the results obtained on the basis of the models (1) and (6) are not so different; however, we should not forget that model (6) is unable to account for the presence of both HRV and all the frequency components[5] observed in the spectrum of the received signal.

Finally, it is worth mentioning that various sensors, such as pressure belts, fiber Bragg gratings, and inertial sensors, can be exploited to monitor chest surface motion (some examples of commercial wearable sensors are described in Section VI-B); however, all these sensors require to be worn by the patient under test. In a measurement campaign for radar-based monitoring, one of these sensors can be used as reference; this allows to separate the cardiac activity from the dominant breathing dynamics. In fact, as already mentioned above, the contribution of heart beats to surface chest motion is relatively small due to respiration. Moreover, the spectral components of heart motion may overlap with the respiratory harmonics; this makes separating the former contribution from the latter one really challenging.

[4]These values have been selected based on the data acquired in our measurement campaigns.

[5]The spectral contribution due to respiration is represented by a few relevant harmonics, as evidenced by our numerical results shown in Section VI-C.

IV. RADAR SYSTEMS: TECHNOLOGIES AND ARCHITECTURES

In this section, after providing a classification of the radar technologies employed for vital signs monitoring, some architectures of radar systems equipped with single and multiple TX/RX antennas are illustrated.

A. Radar Technologies and Classification

Radar systems can be divided into two categories based on the mechanism according to which the waveform they radiate is generated; more specifically, the first category is made of the CW radars, whereas the second one is made of the so-called pulsed radars. In a CW radar, the radiated signal is transmitted continuously, whereas, in a pulsed radar, it is sent over short periods of time. In both cases, the transmitted signal can be modulated or unmodulated; for this reason, radar systems can also be classified based on the modulating waveform. In the technical literature on vital sign estimation, the use of the following types of radar systems has been investigated: 1) CW Doppler radar; 2) FMCW radar; 3) SFCW radar; and 4) IR-UWB radar. In the remaining part of this section, a brief description of each type is provided.

CW Doppler radars radiate a CW radio signal, characterized by a known stable frequency, and are commonly employed for their hardware simplicity. In these radar systems, the chest displacement due to heart and breathing activities results in a variation of the phase of the received signal. Such a variation is inversely proportional to the wavelength of the signal; therefore, reducing the wavelength of the transmitted wave (i.e., increasing its frequency) results in larger changes in the observed phase and, consequently, allows to detect smaller displacements. One of the main limitations of these radar systems is represented by the fact that they are unable to measure the frontal distance, i.e., the range between the radar and any subject detected by it.

FMCW radars and SFCW radars radiate wideband frequency-modulated signals. The main difference between these systems is represented by the fact that, in the former case, the frequency of the transmitted wave evolves over time in a linear manner, whereas, in the latter one, it changes in a stepwise manner. However, in both systems, the propagation delay is extracted from the phase variations observed in the received signal.

Table 1 Minimum and Maximum Values of the Parameters Appearing in (1)–(5). The Values Selected for Generating the Simulation Results Shown in Fig. 1 Are Also Listed

Params	T_{BR} (s)	T_{HR} (s)	T_i (s)	T_e (s)	$\delta_{b,\mathrm{M}}$ (cm)	$\delta_{h,\mathrm{M}}$ (cm)	τ (s)	a_1 (cm)	a_2 (s)	a_3 (s)
Minimum	1.5	0.3	0	0	1	0.1	0	0	0	0
Maximum	6	1.2	T_{BR}	T_{BR}	5	0.9	T_{BR}	1	1	1
Simulation	3	1	$0.5T_{\mathrm{BR}}$	$0.5T_{\mathrm{BR}}$	1.1	0.11	$0.5T_{\mathrm{BR}}$	0.2	0.5	0.8

IR-UWB radars radiate wideband frequency-modulated signals. In these systems, the chest distance is estimated by assessing the delay experienced by sub-nanosecond pulses, being this delay proportional to the distance between the radar and any detected subject.

The abovementioned radar systems can also be classified based on their wavelength or their maximum measurable range. In fact, in the first case, they are divided into microwave radars, characterized by a wavelength of few centimeters, and millimeter-wave (mm-wave) radars, if their central frequency is equal to 77 GHz or, in general, greater than 30 GHz [40]. In the second case, instead, they can be divided into (see, e.g., [41, p. 24, Table 1]): 1) short-range radars, which are able to measure a maximum range of about 30 m; 2) medium-range radars, which are characterized by a maximum range of about 100 m; 3) long-range radars, which achieve the largest maximum range (of the order 250 m).

Each of the considered radar systems is endowed with a single antenna or an antenna array at its TX and/or RX sides. An SISO radar system employs a single antenna at both its sides; note that, most of the CW and IR-UWB radars considered in the technical literature on the monitoring of human vital signs are of SISO type. MIMO radar systems, instead, employ antenna arrays in their transmission and reception; various FMCW and SFCW radars of this type are already available on the market and their use in vital signs monitoring is currently being investigated. It is also important to keep in mind that an SISO radar can estimate the range and/or the distance of single/multiple targets, whereas an MIMO radar makes the estimation of its/their angular coordinates possible.

MIMO radar systems can be divided into statistical radars [42], [43] and colocated radars [44], [45] based on the distance between their TX and RX arrays. In practice, the TX and RX antennas of statistical radar systems are widely separated. On the contrary, the TX antennas of colocated radar systems are close to the RX ones and, in particular, are usually placed on the same shield. The last feature allows to develop compact devices; this explains why all the MIMO radars currently being considered for vital signs monitoring are of this type.

In an MIMO radar system, the signals radiated by distinct TX antennas are orthogonal. The simplest strategy to synthesize orthogonal waveforms is represented by TDM [46]. Adopting this strategy means that distinct TX antennas are activated over disjoint time intervals so that the signals they radiate do not overlap in the time domain.

In selecting a radar system of a specific type, the following relevant features must be considered.

1) *Its maximum detection distance:* This depends on the power radiated by the radar device, on the gain of its antennas, and on the signal processing accomplished at both its TX and RX sides. If commercial radar devices operating at the same power level are considered, FMCW and IR-UWB devices are usually found to achieve a higher value of maximum detection distance than their CW and SFCW counterparts. Note also that colocated MIMO radars benefit from the availability of antenna arrays. In fact, increasing the overall number of radiating elements in their TX and RX arrays results in a larger overall gain and, consequently, in an increase of the maximum detection distance, independently of the adopted modulation format.
2) *The accuracy it can achieve in range estimation:* The highest level of accuracy is attained by MIMO radars (of FMCW, SFCW, or IR-UWB types), due to the fact that the SNR level at their RX side is higher than that of their SISO counterparts [44].
3) *Its ability to detect multiple subjects characterized by different DoAs:* This ability is offered by MIMO radars only[6] since their RX array allows to separate signals received from different directions [46].
4) *Its overall complexity:* In general, SISO radars are significantly simpler than their MIMO counterparts. In the category of SISO radar devices, the CW type is undoubtedly the one having the simplest architecture. In the category of MIMO radar devices, instead, MIMO FMCW radars usually have the largest complexity.
5) *Its cost:* In general, the cheapest radar devices are the ones of CW type. For a given radar type, the cost of commercial MIMO devices is at least twice that of their SISO counterparts. The cost gap between SISO and MIMO devices mainly depends on the size of the employed antenna arrays and, in particular, increases when the overall number of the antenna elements (i.e., the overall number of RF chips) gets larger.

B. Architecture of SISO Radar Systems

In this section, a brief description of the architecture of the radar systems employed for vital signs monitoring

[6]In principle, an SISO radar can be used to detect the vital signs of multiple subjects, provided that their ranges are different (see, e.g., [47]). However, it is unable to estimate their angular coordinates.

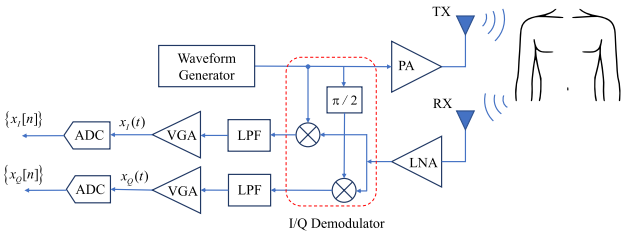

Fig. 2. ***Block diagram of a CW radar.***

is provided. All the considered systems are equipped with single TX and RX antennas. Moreover, in illustrating their baseband processing at the RX side, it is always assumed that the chest of the monitored subject, placed in front of the radar system, can be represented as a single point target for simplicity.[7]

1) CW Radars: Let us focus first on CW radar systems. The architecture[8] of a radar system of this type is represented in Fig. 2. In its transmitter, the RF signal produced by a waveform generator (and characterized by the carrier frequency f_0) feeds a PA, whose response is applied to the TX antenna; this antenna is placed in front of the chest of a human being. The received signal is amplified by an LNA, whose response undergoes frequency down-conversion to extract its in-phase and quadrature (I/Q) components, denoted $x_I(t)$ and $x_Q(t)$, respectively; this task is accomplished by a couple of mixers, each followed by the cascade of a low-pass filter (LPF) with a VGA. The output of each VGA is sampled by an ADC, operating at the frequency $f_s = 1/T_s$, where T_s is the sampling period. The nth sample of $x_I(t)$ ($x_Q(t)$) is denoted $x_I[n] \triangleq x_I(nT_s)$ ($x_Q[n] \triangleq x_Q(nT_s)$); note that the mathematical expression of these samples depends on the transmitted waveform. Further mathematical details are provided in the following for each of the three types of CW radars introduced in Section IV-A.

a) CW Doppler radar: In this case, the waveform generator appearing in Fig. 2 consists in an LO generating a tone at the frequency f_c. The nth sample of $x_I(t)$ and $x_Q(t)$ can be expressed as (see, e.g., [54, Sec. II, eqs. (1) and (2)])

$$x_I[n] = a\cos(\psi[n]) + w_I[n] \tag{9}$$

and

$$x_Q[n] = a\sin(\psi[n]) + w_Q[n] \tag{10}$$

respectively, with $n = 0, 1, \ldots, N-1$; here, n is the fast time index, N represents the overall number of samples acquired in the considered observation interval, a represents the amplitude of the useful signal component, and $w_I[n]$ ($w_Q[n]$) is the contribution of the AWGN affecting the in-phase (quadrature) component

$$\psi[n] \triangleq \psi_0 + \Delta\psi[n] \tag{11}$$

$$\psi_0 = 4\pi\frac{R_0}{\lambda} \tag{12}$$

is a constant phase shift[9] due to the (fixed) distance R_0 between the chest of the considered subject and the radar, and

$$\Delta\psi[n] = \frac{4\pi}{\lambda}\Delta R[n] \tag{13}$$

is the phase variation due to the chest displacement $\Delta R(t)$ [see (1)]; here, $\Delta R[n] \triangleq \Delta R(t = nT_s)$, $\lambda = c/f_0$ is the wavelength of the radiated signal, c is the speed of light, and T_s is the sampling period. From the mathematical results illustrated above, it can be easily inferred that the chest displacement can be assessed by estimating the phase variations over consecutive samples of the complex sequence $\{x[n]; n = 0, 1, \ldots, N-1\}$, where

$$x[n] \triangleq x_I[n] + jx_Q[n] = a\exp(j\psi[n]) + w[n] \tag{14}$$

and

$$w[n] \triangleq w_I[n] + jw_Q[n] \tag{15}$$

is the noise contribution to $x[n]$ (14).

b) FMCW radar: The waveform generator employed in the transmitter of an FMCW radar (and appearing in Fig. 2) consists in a VCO, characterized by the free running frequency f_0 and fed by a periodic ramp generator. The frequency of the transmitted signal evolves periodically and, within each period, changes linearly; this linear frequency sweep is known as chirp. The evolution of the instantaneous frequency over a frame consisting of N_c consecutive chirps is shown in Fig. 3; here, T_0, T, and T_R represent the chirp duration, the ramp time period, and

[7] As a matter of fact, the chest of the monitored subject is usually much larger than the resolution of the employed radar sensor (and, for this reason, should be represented as a cloud of point targets) and absorbs a significant fraction of the incident power at its skin surface [48]. All this is usually neglected in the technical literature.

[8] Note that a different architecture is adopted by CW self-injection-locked radars and CW radars employing super-regenerative oscillators; further details about this topic can be found in [49], [50], [51], [52], and [53].

[9] The phase shift ψ_0 is called DC offset. In vital sign monitoring, this quantity depends on the distance between the employed radar and the chest wall in front of it; however, this term may be influenced by other factors, such as the reflections from stationary targets or from other parts of the human body, and the noise of electronic components.

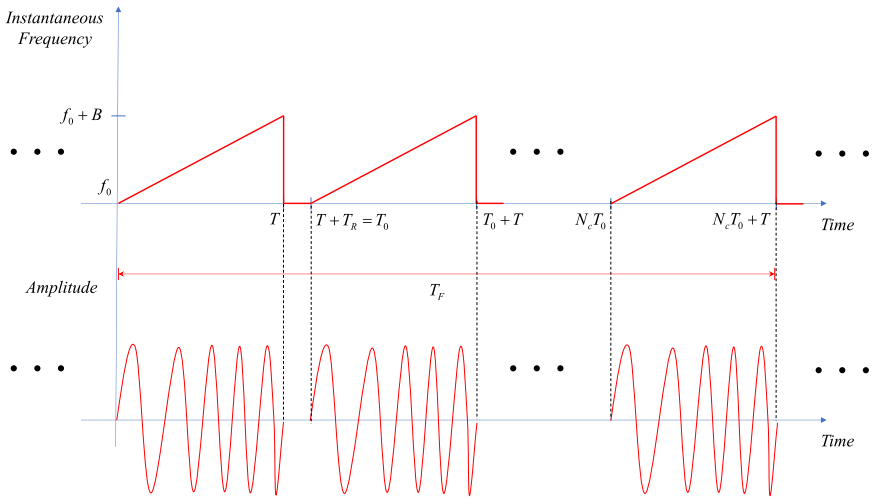

Fig. 3. ***Representation of the instantaneous frequency of the RF signal transmitted in an FMCW radar system.***

the reset time, respectively, so that

$$T_0 = T + T_R \tag{16}$$

and the overall duration of the frame is $T_F = N_c T_0$. Note that each chirp is characterized by the chirp slope

$$\mu \triangleq \frac{B}{T} \tag{17}$$

where B is the width of the swept frequency interval (i.e., the radar bandwidth).

The kth sample of the I/Q components acquired in the nth chirp interval can be expressed as (see, e.g., [41, Sec. 2.1.2, eq. (5)])

$$x_I[k,n] = a\cos(2\pi k f_n T_s + \psi[n]) + w_I[k,n] \tag{18}$$

and

$$x_Q[k,n] = a\sin(2\pi k f_n T_s + \psi[n]) + w_Q[k,n] \tag{19}$$

respectively, with $k = 0, 1, \ldots, N-1$ and $n = 0, 1, \ldots, N_c - 1$; here, N is the overall number of samples acquired over a single chirp

$$T_s \triangleq \frac{T}{N} \tag{20}$$

is the sampling period, k (n) denotes the fast time (slow time) index, $w_I[k,n]$ ($w_Q[k,n]$) is the contribution of the AWGN affecting the in-phase (quadrature) component of the useful signal, a represents the amplitude of the useful signal component

$$f_n \triangleq \mu \tau_n \tag{21}$$

is a frequency proportional to the delay

$$\tau_n \triangleq \frac{2R_n}{c} \tag{22}$$

R_n is the distance of the radar system from the chest (i.e., the target range) in the nth chirp interval. Note that the phase term $\psi[n]$ appearing in the RHS of (18) and (19) is assumed constant within a single chirp and, therefore, it is still expressed by (11).

In the considered radar system, the complex sequence

$$\begin{aligned} x[k,n] &\triangleq x_I[k,n] + j x_Q[k,n] \\ &= a\,\exp(j(2\pi k f_n T_s + \psi[n])) + w[k,n] \end{aligned} \tag{23}$$

is processed to generate an estimate of the frequency f_n, from which an estimate of the target range R_n is easily computed on the basis of (21) and (22); here, $w[k,n] \triangleq w_I[k,n] + j w_Q[k,n]$. Consequently, range estimation is equivalent to the estimation of the normalized frequency

$$F_n \triangleq f_n T_s \tag{24}$$

of a complex exponential sequence.

c) SFCW radar: The transmitter of an SFCW radar is similar to that of an FMCW radar, the only difference being represented by the fact that the ramp generator of the last system is replaced by a staircase waveform generator. Therefore, the instantaneous frequency of the signal generated by the VCO employed in an SFCW radar changes in a stepwise manner within each radiated frequency sweep. The time evolution of the instantaneous frequency of the signal generated by the VCO over a single frame is shown in Fig. 4. In this figure, T_0, T, and T_R represent the frequency sweep duration, the sampling time, and the reset

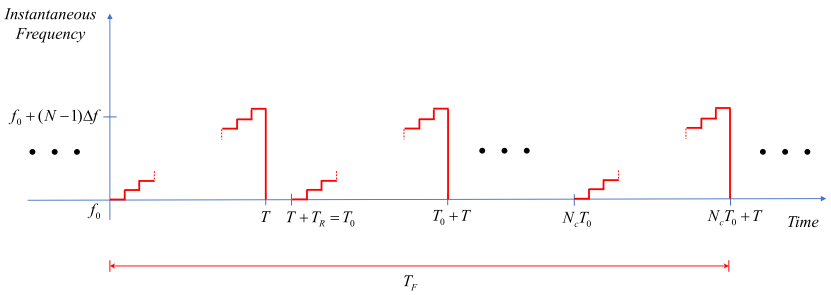

Fig. 4. *Representation of the instantaneous frequency of the RF signal transmitted by an SFCW radar system.*

time, respectively, whereas N and Δf represent the overall number and the width of each frequency step, respectively. Note that, if N_c denotes the overall number of frequency sweeps forming a single frame, each frame lasts $T_F = N_c T_0$ s.

If we assume that the sampling interval T_s is equal to the duration of each frequency step (i.e., the sampling frequency $f_s \triangleq 1/T_s$ is equal to Δf), a single complex sample is acquired at the RX side within each single frequency step. Moreover, in this case, the kth sample of the I/Q components available in the nth frequency sweep interval can be expressed as (see, e.g., [55, Sec II-B, eq. (13)])

$$x_I[k,n] = a\cos(2\pi k\Delta f\tau_n + \psi[n]) + w_I[k,n] \tag{25}$$

and

$$x_Q[k,n] = -a\sin(2\pi k\Delta f\tau_n + \psi[n]) + w_Q[k,n] \tag{26}$$

respectively; here, k, n, a, $\psi[n]$, τ_n $w_I[k,n]$, $w_Q[k,n]$, and N have the same meaning as the one illustrated for the corresponding terms appearing in (18) and (19).

In the considered radar system, the complex sequence $\{x[k,n];\, k = 0, 1, \ldots, N-1\}$, where

$$\begin{aligned} x[k,n] &\triangleq x_I[k,n] + jx_Q[k,n] \\ &= a\exp(-j(2\pi k\Delta f\tau_n + \psi[n])) + w[k,n] \end{aligned} \tag{27}$$

for any n, is processed to generate an estimate of the normalized delay

$$F_n \triangleq \Delta f\tau_n. \tag{28}$$

Since the last quantity can also be interpreted as the normalized frequency of a complex exponential sequence, the frequency estimation algorithms developed for FMCW radar systems can also be employed in SFCW systems; in doing so, we must keep in mind that the only difference between (23) and (27) is represented by the sign of the argument of complex exponential appearing in their RHSs. Finally, it is worth stressing that this similarity can be considered as a form of time–frequency duality [56]; from this viewpoint, an SFCW radar system can be seen as the dual of an FMCW radar system, as evidenced in [57].

Finally, it is worth mentioning that, since, in principle, the useful component of the baseband signal available at the RX side in a CW radar system is a complex exponential [see (14), (23), and (27)], the overall quality of that signal can be assessed by representing its time evolution on a Cartesian plane; this leads to the so-called I/Q constellation graph. In general, these graphs represent a useful way to visualize the baseband output of a CW radar and check whether there is any distortion or I/Q imbalance. An example of I/Q constellation graph referring to the FMCW IWRxx43 radar system described in Section VI-A is shown in Fig. 5. Note that the fluctuations observed in the amplitude of the represented curve are mainly due to the fact that the human chest cannot be modeled as a point target, as assumed in the derivation of the signal model (23); consequently, the received signal results from the superposition of multiple echoes of the radiated waveform.

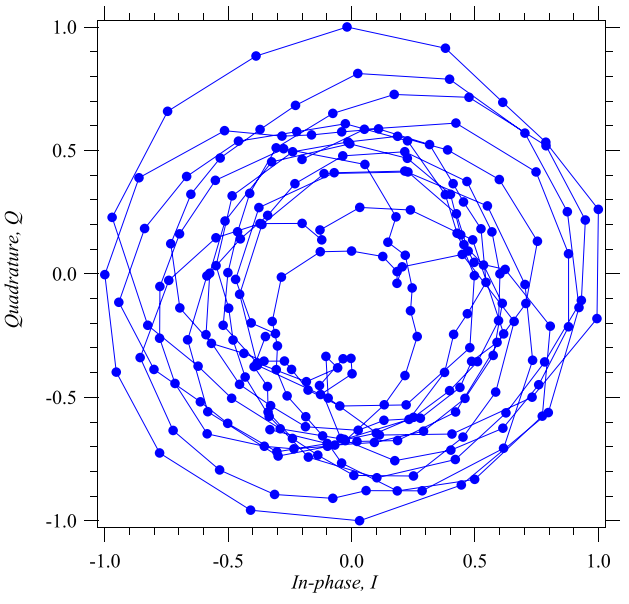

Fig. 5. *I/Q constellation graph generated based on our experimental data.*

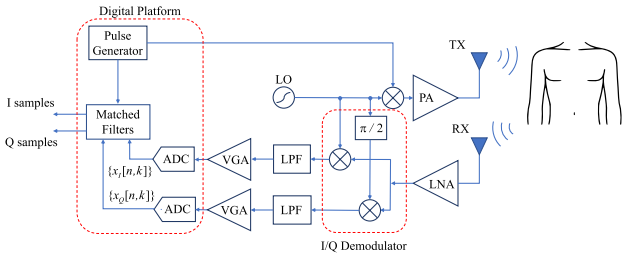

Fig. 6. ***Block diagram of an IR-UWB radar.***

2) IR-UWB Radar: The architecture of an IR-UWB radar is represented in Fig. 6. At the TX side, a tunable Gaussian pulse generator, triggered by a square wave generator, is employed to generate the (baseband) output signal

$$s(t) = \sum_n p(t - nT_0) \tag{29}$$

where $p(t - nT_0)$ represents the nth transmitted pulse and T_0 is the PRI. Note that, if T denotes the duration of each pulse,[10] the interval T_0 is expressed by (16), where T_R is the so-called reset time. The time evolution of $s(t)$ is exemplified in Fig. 7, where N_c consecutive pulses are represented; such pulses form a transmission frame, whose duration is $T_F = N_c T_0$ s.

The signal $s(t)$ (29) undergoes frequency upconversion (accomplished by means of a mixer and an LO operating at the frequency[11] f_0) and power amplification before its transmission.

Since the pulses forming $s(t)$ (29) are not overlapped, we can focus our attention on the echo generated by the chest in response to the kth pulse. At the RX side, the RF signal conveying this pulse is amplified by an LNA and downconverted[12] to extract its I/Q components. Then, these components undergo analog-to-digital conversion at the frequency $f_s = 1/T_s$, where T_s is the sampling period. If τ_n denotes the delay experienced by the considered pulse, the kth sample of the I/Q components associated with it can be expressed as (see, e.g., [58, Sec. II, eq. (4)])

$$x_I[k,n] = a\,p[k,n]\cos(\psi[n]) + w_I[k,n] \tag{30}$$

and

$$x_Q[k,n] = a\,p[k,n]\sin(\psi[n]]) + w_Q[k,n] \tag{31}$$

respectively, with $k = 0, 1, \ldots, N-1$ and $n = 0, 1, \ldots, N_c - 1$; here, a represents the amplitude of the useful signal component

$$p[k,n] \triangleq p(kT_s - \tau_n - nT_0) \tag{32}$$

n, k, and $\psi[n]$ have the same meaning as the one illustrated for the corresponding terms appearing in (18) and (19), $w_I[k,n]$ and $w_Q[k,n]$ represent noise contributions (they correspond to the samples $w_I[n]$ and $w_Q[n]$ contained in the RHS of (9) and (13), respectively), and N is the overall number of samples acquired over each PRI (briefly, of fast time samples). Each of the sequences $\{x_I[k,n]\}$ and $\{x_Q[k,n]\}$ is sent to a digital MF, that is, to a digital filter whose impulse response is the sequence $\{p(T - kT_s); k = 0, 1, \ldots, N-1\}$. The responses of the MFs fed by the samples of the I/Q components are denoted $\{\hat{x}_I[k,n]; k = 0, 1, \ldots, N-1\}$ and $\{\hat{x}_Q[k,n]; k = 0, 1, \ldots, N-1\}$, respectively. If the chest displacement $\Delta R(t)$ is approximately constant within a single PRI, i.e.,

$$\Delta R(kT_s + nT_0) \cong \Delta R(nT_0) \tag{33}$$

for $k = 0, 1, \ldots, N-1$ and any n, matched filtering allows to maximize the output SNR, i.e., the ratio between the energy of the useful component available at the MF output and the average power of the noise component affecting it. The target delay τ_n is estimated by identifying the position of the main peak appearing in the MF response.

Finally, it is useful to point out that the following conditions hold.

1) Equations (30) and (31) can be condensed in the complex signal model

$$\begin{aligned} x[k,n] &\triangleq x_I[k,n] + jx_Q[k,n] \\ &= a\,p[k,n]\exp(j\psi[n]) + w[k,n] \end{aligned} \tag{34}$$

where $w[k,n] \triangleq w_I[k,n] + jw_Q[k,n]$ is the noise component.

2) In IR-UWB radar systems, the presence of clutter, i.e., of reflections from other stationary targets, may affect the estimation of vital signs. The presence of clutter in the received signal can be modeled as DC offset or small amplitude variations in the slow time dimension in (30) and (31).

The received signal models and range formulas provided above for the different types of radar systems are summarized in Table 2.

C. Architecture of MIMO Radar Systems

An MIMO radar system is equipped with a TX and an RX antenna array, consisting of N_T and N_R elements, respectively. As already mentioned above, in a colocated MIMO radar, TX antennas are close to the RX ones and are usually placed on the same shield. It is important to keep in mind that the elements of the TX array are employed to

[10] In practice, T is on the order of hundreds of picoseconds.
[11] This frequency usually belongs to the ISM band.
[12] The downconversion scheme is the same as that shown in Fig. 2.

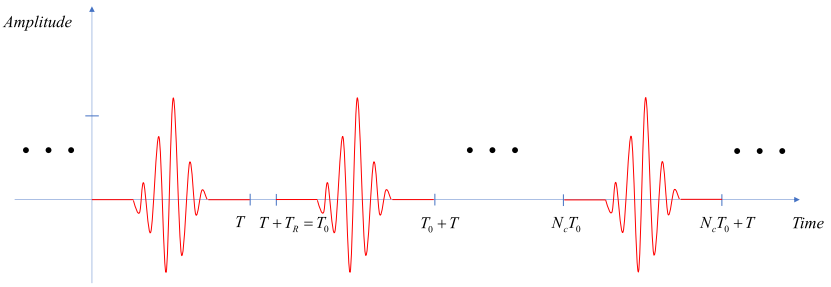

Fig. 7. ***Example of the baseband signal s(t) (29) produced by the pulse generator of the IR-UWB radar system represented in Fig. 6.***

radiate orthogonal waveforms, whereas the RX elements receive distinct replicas of the electromagnetic echoes generated by multiple targets. In these conditions, any couple of physical TX and RX antennas generates independent measurements; for this reason, each of the

$$N_V \triangleq N_T \cdot N_R \tag{35}$$

couples of TX/RX antennas can be replaced by a single VA of an equivalent SISO radar. The abscissa x_v and the ordinate y_v of the vth VA element associated with the pth TX antenna and the qth RX antenna (briefly, the (p, q) VA) are computed as[13] (see, e.g., [59, Paragraph II.A, eq. (1)])

$$x_v = \frac{x_p + x_q}{2} \tag{36}$$

and

$$y_v = \frac{y_p + y_q}{2} \tag{37}$$

respectively, with $p = 0, 1, \ldots, N_T - 1$, $q = 0, 1, \ldots, N_R - 1$, and $v = 0, 1, \ldots, N_V - 1$; thus, a physical array characterized by N_T (N_R) TX (RX) elements is equivalent to a virtual array constituted by N_V channels.

Two physical arrays and the associated virtual arrays are shown in Fig. 8(a) and (b). More specifically, in Fig. 8(a), the 1-D virtual array associated with the given physical array is a ULA since it consists of $N_V = 1 \cdot 4 = 4$ equally spaced and aligned virtual elements [see (35)]; note that, in this case, $y_v = 0$ [see (37)], because of the geometry of the physical array and the selected reference systems, and that the distance between two adjacent VAs is equal to d. Putting together multiple parallel ULAs leads to 2-D URA, such as the one shown in Fig. 8(b). The last array is made of $N_V = 5 \cdot 7 = 35$ VAs [see (35)] or, equivalently, of $N_{\mathrm{VULA}} = 5$ ($N_{\mathrm{HULA}} = 7$) horizontal (vertical) ULAs (one of them is highlighted by a black dashed rectangle), each composed of seven (five) VAs. Note also that, in Fig. 8, the distance between two adjacent horizontally aligned (vertically aligned) VAs is denoted d_{VH} (d_{VV}) and that $d_{\mathrm{VH}} = d_{\mathrm{VV}}$ is assumed. The distance between two adjacent physical elements is usually equal to $\lambda/2$, where λ is the wavelength characterizing the radiated waveforms; consequently, the distances d, d_{VV}, and d_{VH} are all equal to $\lambda/4$. In the following, we will focus only on uniform (linear or rectangular) arrays. However, readers should keep in mind that other array geometries, characterized by a nonuniform antenna spacing, can be employed to achieve the desired tradeoff between resolution and array complexity [60].

Let us focus now on a radar system employing the ULA represented in Fig. 8(a) and assume that: 1) L point targets are detected by this system and 2) the position of the ith target (with $i = 0, 1, \ldots, L - 1$) can be deemed constant in the frame interval in which it is detected (i.e., over an interval lasting T_F s). In this case, the useful component of the received signal consists of the superposition of L contributions, each associated with a different target. More specifically, the contribution given by the ith target is given by

$$x_i^{(v)}[n] = a_i^{(v)} \exp\left(j\psi_i^{(v)}[n]\right) \tag{38}$$

[13]Note that these formulas apply to antenna arrays of arbitrary shapes; their validity is not affected by antenna spacing but requires the detectable targets to be in the far-field zone of the considered radar system. It is also worth mentioning that, in a part of the technical literature (see, e.g., [59, Paragraph 4.3.1, pp. 159–161]), the RHS of (36) and (37) is multiplied by two. When this occurs, all the formulas involving the coordinates of the VAs must be changed accordingly.

Table 2 Received Signal Model and Range Formulas for the Considered Radarsystems

Radar type	Waveform	Received signal model	Target range
Continuous wave	Sine wave	$x[n] = a\exp(j\psi[n])$	unavailable
	Linear frequency modulation	$x[k,n] = a\exp\left(j\left(2\pi k f_n T_s + \psi[n]\right)\right)$	$R_n = f_n \cdot c/(2\mu)$
	Stepped frequency modulation	$x[k,n] = a\exp\left(-j\left(2\pi k \Delta f \tau_n + \psi[n]\right)\right)$	$R_n = \tau_n \cdot c/2$
Impulse-radio	Gaussian pulse	$x[k,n] = a\,p[k,n]\exp\left(j\psi[n]\right)$	$R_n = \tau_n \cdot c/2$

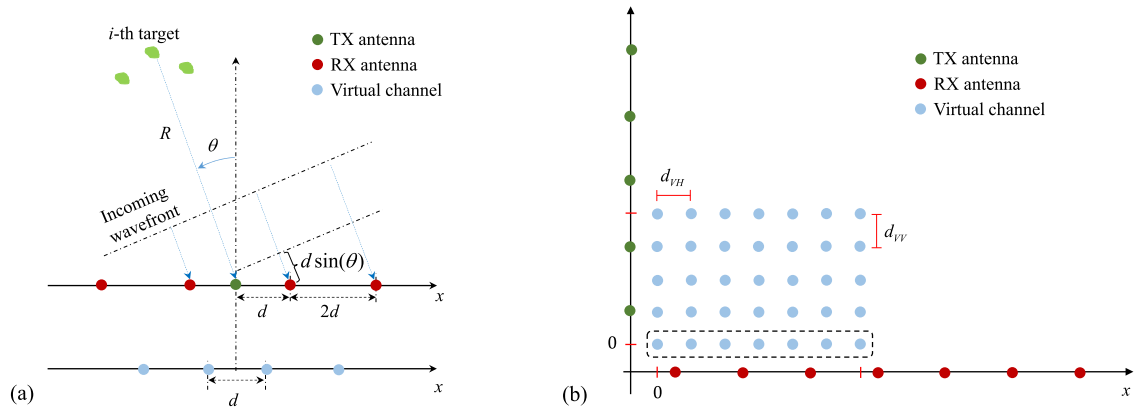

Fig. 8. ***Representation of (a) ULA and (b) URA. In both cases, the physical array and the associated virtual array are considered.***

for the CW radar system described in Section IV-B1.a [see (14)]

$$x_i^{(v)}[k,n] = a_i^{(v)} \exp\left(j\left(2\pi k f_i^{(v)} T_s + \psi_i^{(v)}[n]\right)\right) \tag{39}$$

for the FMCW radar system described in Section IV-B1.b [see (23)]

$$x_i^{(v)}[k,n] = a_i^{(v)} \exp\left(-j\left(2\pi k \tau_i^{(v)} \Delta f + \psi_i^{(v)}[n]\right)\right) \tag{40}$$

for the SFCW radar system described in Section IV-B1.c [see (27)] and

$$x_i^{(v)}[k,n] = a_i^{(v)} p\left(kT_s - \tau_i^{(v)} - nT_0\right) \exp\left(j\psi_i^{(v)}[n]\right) \tag{41}$$

for the IR-UWB radar system described in Section IV-B2 [see (34)]. In (38)–(41), it is assumed that the following conditions hold.

1) The integer v denotes the index of the selected VA (we assume that $v = 0, 1, \ldots, N_V - 1$).
2) The positive real $a_i^{(v)}$ is the amplitude of the contribution due to the ith target and observed on the vth VA.
3) The phase $\psi_i^{(v)}[n]$ can be expressed as

$$\psi_i^{(v)}[n] = \psi_{0,i}^{(v)} + \Delta\psi_i[n] \tag{42}$$

where

$$\psi_{0,i}^{(v)} = \frac{4\pi}{\lambda}\left(R_{0,i} + v\, d \sin(\theta_i)\right) \tag{43}$$

$\Delta\psi_i[n]$ is still expressed by (13), θ_i is the azimuth of the ith target, and $R_{0,i}$ is the range of the ith target assuming zero chest displacement.

4) The frequency $f_i^{(v)}$ is given by

$$f_i^{(v)} = \mu \tau_i^{(v)} \tag{44}$$

whereas the delay $\tau_i^{(v)}$ can be approximated as

$$\tau_i^{(v)} \approx \frac{2}{c}\left(R_{0,i} + v\, d \sin(\theta_i)\right) \tag{45}$$

if we assume that $R_{0,i}$ is much larger that the variations experienced by the ith target range in the considered frame interval [see (1)].

Finally, it is important to point out that, in CW and IR-UWB radar systems, the azimuth of a given target influences the phase of the received signal component associated with it, whereas in FMCW (SFCW) radar systems, it influences also the normalized frequency (normalized delay) characterizing that component. However, in any case, an estimate of the DOA of the electromagnetic echo originating from a given target is computed based on the phases referring to that target and observed over multiple antennas of the same RX array.

V. SIGNAL PROCESSING ALGORITHMS FOR VITAL SIGNS MONITORING

In this section, we first describe the most important deterministic and LB processing methods that can be employed to extract vital signs from the measurements provided by the SISO radar systems described in Section IV. Then, we provide essential information about the processing accomplished in colocated FMCW and SFCW MIMO radars for estimating the vital signs of multiple people. Finally, we illustrate some numerical results generated by applying some of the considered methods to a synthetically generated dataset.

A. Deterministic Detection and Estimation Algorithms for SISO Radars

The majority of the radar-based methods for vital signs monitoring appeared in the technical literature have the

following features: 1) they are deterministic [i.e., model-based (MB)] since their derivation is based on our prior knowledge about the structure of radar echoes and 2) they extract vital signs from the phase of the received signal. As far as the last point is concerned, it is useful to focus first on an SISO CW Doppler radar for simplicity and to reconsider the phase expression [see (11)]

$$\psi[n] \triangleq \psi_0 + \Delta\psi[n] \tag{46}$$

provided in Section IV-B1.a for the nth received signal sample (where n denotes the fast time index). As already illustrated in in Section IV-B1.a, the constant ψ_0 appearing in (46) represents the so-called DC offset, whereas [see (13)]

$$\Delta\psi[n] = \frac{4\pi}{\lambda}\Delta R[n] \tag{47}$$

is a time-varying term related to the body movement induced by breath and cardiac activities and, consequently, conveys the information we are interested in. This explains why the first step accomplished by the deterministic methods developed for CW Doppler radars consists in extracting the phase of the received signal sequence $\{x[n]\}$, as shown in Fig. 9, where a block diagram is represented to describe the overall processing they accomplish. As shown in this figure, phase extraction is carried out by the first block, which generates the N_r-dimensional vector

$$\hat{\boldsymbol{\psi}} \triangleq [\hat{\psi}[0], \hat{\psi}[1], \ldots, \hat{\psi}[N_r - 1]]^T \tag{48}$$

on the basis of the sample sequence $\{x[n]\}$ (whose elements are collected in the vector **x** appearing in Fig. 9); here, N_r is the overall number of measurements and $\hat{\psi}[n]$ represents an estimate of $\psi[n]$ (46), i.e., of the phase of the complex sample $x[n]$ (which is expressed by (14) in the case of a single point target). Given the vector $\hat{\boldsymbol{\psi}}$ (48), estimates of the BR and HR can be evaluated by applying the so-called periodogram method [61], i.e., by identifying the dominant frequency components in the amplitude spectrum of $\{\hat{\psi}[n]\}$. In fact, it is known that: 1) the highest peak in the abovementioned spectrum is found at the breath frequency in normal respiration conditions and 2) the HR is higher than the BR (at least more than two times higher). For these reasons, an estimate $\hat{f}_b$ of the BR f_b (expressed in acts/s) can be computed as

$$\hat{f}_b = \hat{b}\, f_r \tag{49}$$

where

$$\hat{b} = \arg \max_{\tilde{b} \in \{0,1,\ldots,N_0/2\}} |Y_{\tilde{b}}| \tag{50}$$

$$Y_{\tilde{b}} \triangleq \frac{1}{N_r} \sum_{n=0}^{N_r-1} \hat{\psi}[n] \exp\left(-j2\pi n\, \tilde{b}\, /N_0\right) \tag{51}$$

$$N_0 \triangleq M\, N_r \tag{52}$$

M is the oversampling factor and

$$f_r \triangleq \frac{1}{N_0 T_s} \tag{53}$$

for the CW Doppler radar system described in Section IV-B. Note that: 1) $Y_{\tilde{b}}$ (51) represents the $\tilde{b}$th element of an order N_0 DFT of $\hat{\boldsymbol{\psi}}$ (48) and can be efficiently computed by adopting an FFT algorithm of the same order, as shown in Fig. 9; 2) the strategy expressed by (50) aims at identifying the dominant spectral component in the spectrum of the sequence $\{\hat{\psi}[n]\}$; and 3) for a given M, the adoption of a larger N_r (i.e., of a longer observation time) allows to achieve a better spectral resolution.

A similar procedure can be employed for estimating the HR f_h. However, in this case, FFT processing is preceded by BPF to cancel all the spectral components whose frequency falls outside the interval in which the heart frequency is expected (see Fig. 9). Then, an estimate $\hat{f}_h$ of f_h can be evaluated as

$$\hat{f}_h = \hat{h}\, \bar{f}_r \tag{54}$$

where

$$\bar{f}_r \triangleq \frac{1}{\bar{N}_0 T_s} \tag{55}$$

$$\hat{h} = \arg \max_{\tilde{h} \in \{0,1,\ldots,\bar{N}_0/2\}} |Z_{\tilde{h}}| \tag{56}$$

$Z_{\tilde{h}}$ (51) represents the $\tilde{h}$th element of an order

$$\bar{N}_0 \triangleq \bar{M}\, N_r \tag{57}$$

DFT of the BPF output vector (whose size is equal to N_r) and $\bar{M}$ denotes the adopted oversampling factor. It is worth pointing out that the following conditions hold.

1) Since some prior knowledge about the minimum and maximum BRs to be detected is usually available, the search interval in the RHS of (50) can be restricted to reduce the overall computational cost of the search for the maximum over the set $\{|Y_{\tilde{b}}|\}$. Similar considerations hold for (56) since $\{|Z_{\tilde{h}}|\}$ takes on significant values in a restricted frequency range because of the employed BPF.
2) The topology and order of the bandpass filter employed in HR estimation depend on the required selectivity; for instance, a fourth-order digital bi-quad filter and a fifth-order low-pass Butterworth filter have been adopted in [62] and [63], respectively. The

main problem in filter design is represented by the selection of its passband since the spectral components due to BR (HR) should not fall inside (out of) it. In general, the lower limit f_L and the upper limit f_U of the filter passband should be selected in a way that $f_L \geq 2/T_{\mathrm{BR}}$ and $f_U \leq 3/T_{\mathrm{HR}}$, where T_{BR} (T_{HR}) is the breath (heart) period (see Section III-A).

3) Generally speaking, the evaluation of an order N_0 ($\bar{N}_0$) FFT in BR (HR) estimation leads to partitioning the frequency interval in N_0 ($\bar{N}_0$) frequency bins, all having the same size. The quantity $\hat{b}$ (50) [$\hat{h}$ (56)] represents an estimate of the index of frequency bin inside which the fundamental frequency of respiration (heart) signal falls, whereas f_r (53) [$\bar{f}_r$ (55)] is the bin size.
4) Since the phase vector $\hat{\boldsymbol{\psi}}$ is real, the FFT output vectors **Y** and **Z** are Hermitian symmetric; this explains why only a portion of their elements is involved in the search required by (50) and (56) .

Let us focus now on the extraction of phase information in CW Doppler radars [64], [65], [66]. This is usually accomplished by means of the AD technique. This means that the nth element of the vector $\hat{\boldsymbol{\psi}}$ (48) is evaluated as[14]

$$\hat{\psi}[n] = \arctan\left(\frac{x_Q[n]}{x_I[n]}\right) \tag{58}$$

for $n = 0, 1, \ldots, N_r - 1$. If $x_I[n]$ or $x_Q[n]$ are equal to zero, the last equation is replaced by

$$\hat{\psi}[n] = \arcsin\left(x_Q[n]\right) \tag{59}$$

and

$$\hat{\psi}[n] = \arccos\left(x_I[n]\right) \tag{60}$$

respectively. It is important to point out that the following conditions hold.

1) CW radar systems suffer from a DC offset,[15] which is due to the direct coupling between TX/RX antennas; the reflections from stationary objects surrounding the considered subject, and the self-mixing of the LO employed in the radar system. A large DC offset may saturate the baseband amplifier and clip its output signal. The contribution of a DC offset and potentially strong low-frequency components to the received signal phase is commonly suppressed by a coupling capacitor inserted between the radar mixer and the baseband amplifier following it; however, this may affect the useful signal component if the detected target is moving slowly or stops for some time. To overcome this limitation, a DC coupled radar system has been proposed in [68]. Other techniques have been proposed in [70], [69], and [67] and are based on polynomial fitting and on an LS approach.
2) The estimated phase sequence $\{\hat{\psi}[n]\}$ may exhibit some discontinuities. In fact, a discontinuity appears in the extracted phase whenever the condition[16] [see (47)]

$$\Delta\hat{\psi}_{n+1,n} \triangleq |\hat{\psi}[n+1] - \hat{\psi}[n]| = \frac{4\pi}{\lambda}\Delta R_{n+1,n} \geq 2\pi \tag{61}$$

is met; here, $\Delta R_{n+1,n} \triangleq |\hat{R}[n+1] - \hat{R}[n]|$. This means that, whenever the range variation $\Delta R_{n+1,n}$ observed over two consecutive sampling epochs exceeds half a wavelength, the value of the estimated phase becomes ambiguous. Note that this problem becomes more relevant as the frequency f_0 of the radiated signal increases (for instance, if $f_0 = 77$ GHz, any displacement exceeding 2 mm produces a phase ambiguity).
3) The phase sequence $\{\hat{\psi}[n]\}$ always undergoes a transformation known as unwrapping; unwrapping aims at ensuring that the variation between two consecutive elements of this sequence does not exceed π. In practice, this result is achieved by adding a multiple of 2π to some of the elements of the sequence $\{\hat{\psi}[n]\}$. However, the use of unwrapping may introduce errors in the presence of abrupt phase variations. In this case, the extended differentiate and cross-multiply (DACM) algorithm proposed in [71] or its modified version [72] should be employed to achieve precise phase unwrapping.

Finally, it is worth mentioning that an alternative to the arctangent method is represented by the CSD technique. This technique is based on the idea that the received signal can be seen as a frequency-modulated waveform [see (6) and (47)]. Therefore, an approximate model, based on the first-order Bessel functions, can be derived for it [73]. This allows to separate the contribution due to the periodic movement of the chest from the one associated with the position of the body [i.e., with the term ψ_0; see (12)]. In particular, the Fourier analysis can be directly applied to the sequence $\{x[n]\}$ [see (14)] to estimate both BR and HR.

The architecture of the deterministic methods developed for FMCW, SFWC, and IR-UWB radars can also be represented through the block diagram in Fig. 9. However, in these cases, the following changes are made.

1) The parameter T_s appearing in the RHSs of (53) and (55) is replaced by the PRI T_p in the case of

[14]The $\arctan(\cdot)$ operator can also be replaced by the $\arctan2(\cdot)$ operator in order to extend the codomain from $(-\pi/2, \pi/2)$ to $(-\pi, \pi)$.

[15]The presence of a DC offset can be detected by representing the I/Q constellation graph of the baseband received signal (see, e.g., [67, p. 54962, Fig. 4]).

[16]In the derivation of the following result, the $\arctan2(\cdot)$ operator is assumed in place of the simpler $\arctan(\cdot)$.

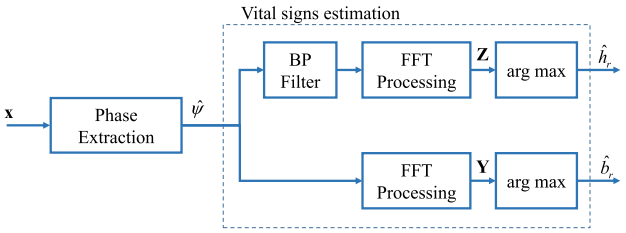

Fig. 9. ***Representation of the signal processing chain characterizing various deterministic methods for vital sign estimation.***

IR-UWB radar system and by the chirp (i.e., by the frequency sweep) duration T_0 in the case of an FMCW (SFCW) radar system.

2) The algorithm for extracting phase estimation [i.e., for generating the vector $\hat{\psi}$ (48)] is more complicated.

As far as the last point is concerned, further details are provided in the following.

1) FMCW and SFCW Radars: Let us concentrate first on the simplest method that can be adopted in an FMCW radar system for the extraction of the abovementioned phase information. This method processes the received signal samples acquired over a single transmission frame (made of N_c consecutive chirps; see Section IV-B) and consists of the following steps.

1) The $N_0' \times N_c$ complex matrix $\mathbf{X} = [X[l,n]]$ is computed; here,

$$X[l,n] \triangleq \frac{1}{N}\sum_{k=0}^{N-1} x[k,n]\exp\left(-j2\pi nl/N_0'\right) \tag{62}$$

with $l = 0,1,\ldots,N_0'-1$ and $n = 0,1,\ldots,N_c-1$. Note that $X[l,n]$ represents the lth coefficient of an order N_0' DFT of the signal samples acquired over the nth chirp of the considered transmission frame.

2) The index of the frequency bin

$$\hat{l} \triangleq \arg\max_{\tilde{l}\in\{0,1,\ldots,N_0'-1\}} \left|X\left[\tilde{l},n\right]\right| \tag{63}$$

associated with the target (i.e., with the chest of the subject under test) is identified.

3) Phase extraction is accomplished through the AD method (followed by phase unwrapping) but does not involve the time-domain samples of the received signal (i.e., the samples $\{x[k,n]\}$). In fact, the samples $x_I[n]$ and $x_Q[n]$ are replaced by $\Re\{X[\hat{l},n]\}$ and $\Im\{X[\hat{l},n]\}$, respectively, in (58)–(60) (here, $\Re\{x\}$ and $\Im\{x\}$ denote the real part and the imaginary part of x, respectively).

It is important to point out that the following conditions hold.

1) The procedure described above generates, as a by-product, an estimate of the range of the target, i.e., of the distance between the radar and the chest wall of the subject under test. In fact, given $\hat{l}$ (63), such an an estimate is given by

$$\hat{R}_0 = \hat{l}K_m \tag{64}$$

where, in the case of an FMCW radar system

$$K_m \triangleq \frac{c}{2\mu N_0' T_s} \tag{65}$$

is the bin-to-meters conversion factor. Based on (17) and (20) (with $N = N_r$), the last formula can be easily put in the form

$$K_m \triangleq \frac{cN_r}{2N_0'B} \tag{66}$$

where B is the radar bandwidth. The last formula and (64) lead to the conclusion that a larger bandwidth leads to a better granularity in range estimation, i.e., results in a better range resolution (see also Section VI-A).

2) Some methods, similar to the ones described above for CW Doppler radars, are available for the compensation of a DC offset or of large movements; in fact, they are based on filtering techniques or on polynomial fitting [21], [67], [69].

3) If the distance between the chest wall and the radar is known with a certain accuracy (e.g., when the radar is employed for monitoring the vital signs of a patient in a bed), a procedure for reducing the region of interest (ROI) can be implemented to simplify the estimation of $\hat{l}$. In particular, $\hat{l}$ can be searched in the ordered set $\{l_m, l_m+1,\ldots,l_M\}$, made of $l_M - l_m + 1$ elements; here, $l_m = \lfloor R_m/K_m \rfloor$, $l_M = \lceil R_M/K_m \rceil$, and R_m (R_M) is the minimum (maximum) expected range.

The method illustrated above for an FMCW radar system can also be employed for an SFCW radar system because of the duality relating such systems (see Section IV-B1.c). The only difference is represented by the fact that the definition (62) is replaced by

$$X[l,n] \triangleq \frac{1}{N}\sum_{k=0}^{N-1} x[k,n]\exp\left(j2\pi nl/N_0'\right) \tag{67}$$

with $l = 0,1,\ldots,N_0'-1$ and $n = 0,1,\ldots,N_c-1$. This means that an N_0' DFT is replaced by an IDFT of the same order, which is efficiently evaluated through an IFFT.

2) IR-UWB Radars: The AD method described in Section V-A can also be employed for phase extraction in IR-UWB radar systems. In this case, however, the samples

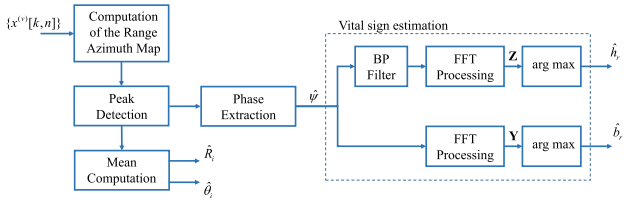

Fig. 10. ***Representation of the signal processing described in Section V-B and employed for estimating the position (range and azimuth) and the vital signs (HR and BR) of multiple people by means of a colocated MIMO radar.***

$x_I[n]$ and $x_Q[n]$ appearing in the RHS of (58) are replaced by $x_I[\hat{k},n]$ and $x_Q[\hat{k},n]$ [see (30) and (31)], respectively, with $n=0,1,\ldots,N_c-1$; here, $\hat{k}$ denotes the value of the fast time index k corresponding to the main peak detected at the MF response.[17] Note also that phase estimation is followed by phase unwrapping and that, given $\hat{k}$, an estimate $\hat{\tau}$ of the delay characterizing the detected target can easily computed; this allows to evaluate the estimate $\hat{R}_0=\hat{\tau}\,c/2$ of the distance R_0 between the radar and the chest of subject under test [see (12)].

Finally, it is worth mentioning that the following conditions hold.

1) The clutter contribution to the samples $\{x[k,n]\}$ can be removed by applying a high-pass filter to this sequence. However, if the clutter produces small fluctuations along the slow-time axis, algorithms based on polynomial fitting can be employed for its removal [67].
2) The SNR of the received signal can also be improved by resorting to noise reduction techniques. An example of such techniques is provided in [74, Sec. 3.2], where the EMD is exploited for noise mitigation. In this case, the sequence $\{x[k,n]\}$ is decomposed into a superposition of intrinsic subsignals, defined at precise instantaneous frequencies and called IMFs. This method allows to retain only the most important frequency components of the input signal and to filter out the oscillations associated with noise components.

Some alternatives to the FFT-based estimation method described above are also available in the technical literature. These are based on the evaluation of a fourth-order cumulant [75] or of a CWT; note that the use of the CWT in place of the FFT allows to analyze how the frequency components of the received signal phase evolve over time [74].

B. Estimation of Vital Signs of Multiple Subjects Through MIMO Radars

In the last few years, increasing attention is being paid to MIMO radar systems, mainly because they make range and DOA estimation of multiple targets possible. The use of MIMO FMCW, IR-UWB, and CW radar systems for the monitoring of vital signs has been investigated in [62], [76], [77], [78], [79], [80], [81], and [82]. More specifically, the use of MIMO FMCW radars operating at 77 and 120 GHz has been studied in [62], [76], [77], and [79], whereas the simultaneous use of two FMCW radars, each endowed with single ULA, but one operating at 24 GHz and the other one at 77 GHz, has been investigated in [78]. Nosrati et al. [82], instead, focused on the use of beamforming in MIMO CW radar systems.

Let us illustrate now some key concepts that are useful to understand the processing accomplished at the RX side of an MIMO radar system. To begin, we focus on an FMCW MIMO radar equipped with N_T TX and N_R RX antennas [and, consequently, with $N_V=N_T\,N_R$ VAs; see (35)]. Under the assumptions illustrated in Section IV-C, the signal samples acquired in a single frame through the N_V VAs can be collected in $N\times N_V\times N_c$ matrix $\mathbf{x}\triangleq\{x^{(v)}[k,n]\}$, where

$$x^{(v)}[k,n]\triangleq\sum_{i=0}^{L-1}A_{i,n}^{(v)}\exp\left(j2\pi k\,F_{i,n}^{(v)}\right)+w^{(v)}[k,n] \quad (68)$$

with $k=0,1,\ldots,N-1$, $n=0,1,\ldots,N_c-1$, and $v=0,1,\ldots,N_V-1$; here, L is the overall number of targets, and $A_{i,n}^{(v)}$ ($F_{i,n}^{(v)}=f_{i,n}^{(v)}T_s$) is the complex amplitude (the normalized version of the frequency $f_{i,n}^{(v)}$) characterizing the ith target observed on the vth VA in the nth chirp interval. A processing method that can be adopted in this case to estimate the range, the DOA, and the vital signs of multiple people in the considered radar system is described by the block diagram represented in Fig. 10. Such a method consists in the four steps listed as follows.

1) *Computation of the range–azimuth map:* A size $N_0'\times N_A$ 2D-FFT of the $N\times N_V$ input matrix $\mathbf{x}[n]=[x^{(v)}[k,n]]$ (with $k=0,1,\ldots,N-1$ and $v=0,1,\ldots,N_V-1$) is computed in the nth chirp interval (with $n=0,1,\ldots,N_c-1$); this produces the $N_0'\times N_A$ matrix

$$\mathbf{X}_n=\left[X^{(n)}[l,m]\right] \quad (69)$$

with $l=0,1,\ldots,N_0'-1$ (see Section V-A1) and $m=-N_A/2,\,-N_A/2+1,\ldots,N_A/2-1$. Then, the nth range–azimuth map is evaluated as

$$\mathbf{J}[n]\triangleq\left[|X^{(n)}[l,m]|\right] \quad (70)$$

with $n=0,1,\ldots,N_c-1$. Note that $N_0'=NM$ ($N_A=N_VM_V$), where M (M_V) denotes the oversampling factor adopted in the fast time (VA) domain.
It is worth mentioning that, in the technical literature on radar systems (see, e.g., [41, Sec. "Velocity estimation"]), the first step in the signal processing

[17] It is assumed that $\hat{k}$ does not change in the considered frame interval for simplicity.

chain at the RX side often consists in the computation of a range-Doppler map, in place of the considered range–azimuth map; this aims at jointly estimating the range and velocity of all the targets detectable in the considered propagation environment. However, in vital signs monitoring, the presence of one or more static subjects is usually assumed. For this reason, on the one hand, Doppler estimation is not meaningful; on the other hand, the localization of the monitored subject in a room or a bed is required to generate accurate estimates of his/her vital signs.

2) *Peak detection:* The peaks appearing in the nth range–azimuth map $\mathbf{J}[n]$ are detected by means of a proper method (for instance, the so-called CFAR method can be adopted [83]) since each of them reveals the presence of a potential target. Let us assume that, independently of n, $\hat{L}$ peaks are detected in the nth range–azimuth map $\mathbf{J}[n]$ and that the position of the ith peak (with $i = 0, 1, \ldots, \hat{L}-1$) is identified by the couple $(\hat{l}_i[n], \hat{m}_i[n])$ (with $n = 0, 1, \ldots, N_c - 1$). Then, the estimate

$$\hat{R}_i[n] = K_m \hat{l}_i[n] \tag{71}$$

of the range and the estimate

$$\hat{\theta}_i[n] = \arcsin\left(\hat{m}_i[n]\, f_r\right) \tag{72}$$

of the azimuth are evaluated for the target associated with the ith peak; here, K_m is expressed by (65) and $f_r = 2/N_A$ [see (21), (22), and (53)]. Given the set $\{(\hat{l}_i[n], \hat{m}_i[n]);\, i = 0, 1, \ldots, \hat{L}-1\}$, the $\hat{L} \times N_c$ matrix

$$\bar{\mathbf{X}} = [\bar{X}[i, n]] \tag{73}$$

is generated; here,

$$\bar{X}[i, n] = X^{(n)}\left[\hat{l}_i[n],\, \hat{m}_i[n]\right] \tag{74}$$

with $i = 0, 1, \ldots, \hat{L}-1$ and $n = 0, 1, \ldots, N_c - 1$.

3) *AD and phase unwrapping:* In this step, the ith row of the matrix $\bar{\mathbf{X}}$ (73) undergoes AD followed by phase unwrapping (with $i = 0, 1, \ldots, \hat{L}-1$); this produces the phase vector

$$\hat{\boldsymbol{\psi}}_i \triangleq [\psi_i[0], \psi_i[1], \ldots, \psi_i[N_c - 1]]^T. \tag{75}$$

4) *BR and HR estimation:* The phase vector $\hat{\boldsymbol{\psi}}_i$ undergoes FFT processing (with $i = 0, 1, \ldots, \hat{L}-1$); this produces the N_m-dimensional spectrum $\bar{\boldsymbol{Y}}_i$ [whose $\tilde{b}$th element is expressed by (51)]. Then, an estimate $\hat{b}_r[i]$ ($\hat{h}_r[i]$) of the BR (HR) associated with the ith target is evaluated on the basis of (50) [see (56)].

At the end of the procedure described above, the range estimate

$$\hat{R}_i = \frac{1}{N_c} \sum_{n=0}^{N_c-1} \hat{R}_i[n] \tag{76}$$

and the azimuth estimate

$$\hat{\theta}_i = \frac{1}{N_c} \sum_{n=0}^{N_c-1} \hat{\theta}_i[n] \tag{77}$$

can be computed for the ith target by averaging the corresponding estimates evaluated over each of the N_c chirps forming the considered transmission frame (with $i = 0, 1, \ldots, \hat{L}-1$).

Finally, it is important to point out that the procedure illustrated above for an MIMO FMCW radar system can be easily adapted to MIMO IR-UWB and SFCW radars; in the last case, FFTs must be replaced by IFFTs.

C. Numerical Results

In this section, we show some numerical results generated by applying various estimation methods illustrated above to a set of synthetically generated data. We first focus on an SISO FMCW radar and an SISO SFCW radar, both placed in front of the chest of a single subject at the distance $d = 0.5$ m. The following assumptions have been made in generating our dataset.

1) The model described by (1)–(4) is adopted for the chest displacement of the monitored subject (modeled as a single point target for simplicity); its parameters are the same as those listed in the fourth row of Table 1).
2) The signal models expressed by (23) and (27) for FMCW and SFCW radars, respectively, have been employed. Moreover, the following values have been selected for their parameters: carrier frequency $f_0 = 77$ GHz (the corresponding wavelength is $\lambda = c/f_0 = 3.9$ mm); bandwidth $B = 2$ GHz; number of samples $N = 256$ (in the time domain for each chirp of the FMCW radar, in the frequency domain for each frequency-modulated pulse of the SFCW radar); chirp (pulse) repetition period $T_0 = 0.06$ s for the FMCW (SFCW) radar; number of chirps/frame (pulses/frame) $N_c = 1034$ for the FMCW (SFCW) radar; and ADC sampling frequency $f_s = 9$ MHz ($f_s = 7.8$ MHz) for the FMCW (SFCW) radar. Moreover, the ramp parameters of the FMCW are: reset time $T_R = 0$, ramp time $T = N/f_s = 28$ μs, and chirp slope $\mu = 70.312$ MHz/μs.
3) In both systems, the frame duration is $T_F = N_c T_0 \cong 60$ s; this parameter represents also the duration of our observation interval.

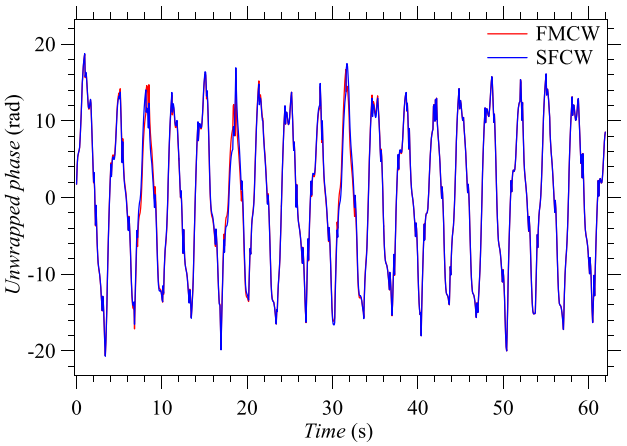

Fig. 11. *Representation of the elements of the phase vector $\hat{\psi}$ (48) resulting from synthetically generated measurements. Both FMCW and SFCW radar systems are considered.*

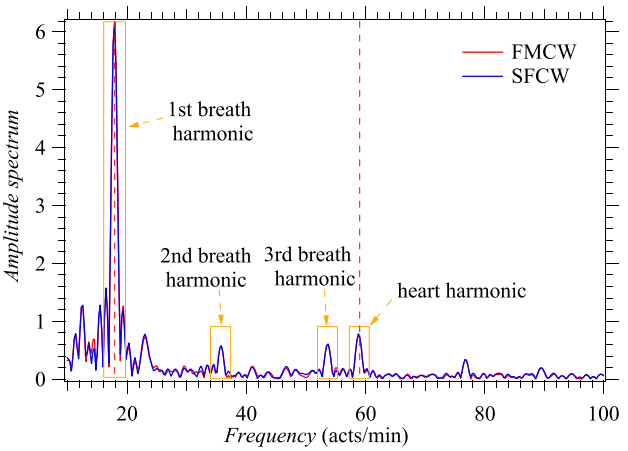

Fig. 12. *Representation of the amplitude spectrum referring to the phase vector $\hat{\psi}$ shown in Fig. 11. The dashed vertical lines identify the exact values of BR and HR. Both FMCW and SFCW radar systems are considered.*

4) The real and imaginary parts of the AWGN noise samples $\{w[k,n]\}$ appearing in the RHS of (23) and (27) have zero mean and variance $\sigma_n^2 = 0.1$.

Our synthetically generated data have been processed by means of the deterministic method described in Section V-A: its overall architecture is represented in Fig. 9. The AD method followed by phase unwrapping has been used for phase estimation and the following choices have been made: 1) DFT orders $N_0' = 512$ and $N_0 = \bar{N}_0 = MN_c = 4 \cdot 1034 = 4136$; 2) $K_m = 31$ [bin-to-meters conversion factor; see (65)]; and 3) the bandpass filter employed in HR estimation is a fourth-order Butterworth filter and the lower (upper) limit of its passband is $f_L = 50/60 \cong 0.83$ Hz ($f_U = 100/60 \cong 1.7$ Hz), so that its bandwidth is $B_{BP} = f_U - f_L \cong 0.87$ Hz.

The elements of the phase vector $\hat{\psi}$ (48) obtained for the FMCW and SFCW radar systems are represented in Fig. 11. The amplitude spectrum obtained at the output of the slow-time FFT (IFFT) executed for phase estimation in the FMCW (SFCW) radar system is shown in Fig. 12, whereas the amplitude spectrum evaluated after BPF of the phase vector is shown in Fig. 13. The results obtained for the considered radar systems are similar and deserve the following comments.

1) The phase signal does provide information about the dynamics of chest displacement; in fact, comparing Fig. 11 with Fig. 1 leads to the conclusion that its evolution is similar to that characterizing the chest displacement in the considered scenario.
2) The peaks appearing in the amplitude spectrum shown in Fig. 12 are associated not only with the BR and the HR but also with the harmonics of the BR. Note, in particular, that the third harmonic falls inside the passband of the filter and that its presence may lead to a wrong estimate of the HR.
3) Based on the available spectra, the estimates $\hat{b}_r = 17.9$ acts/min and $\hat{h}_r = 58.8$ acts/min evaluated for the BR and the HR, respectively, are very accurate since the exact values of these rates are $b_r = 18$ acts/min and $h_r = 60$ acts/min, respectively.

Let us focus now on an MIMO FMCW radar system placed in front of the chest of three static subjects (the ith subject is denoted S_i, with $i = 1$, 2, and 3), whose range (R), azimuth (θ), HR (h_r), and BR (b_r) are listed in Table 3. In this case, the following assumptions have been made in synthetically generating our dataset.

1) The chest displacement characterizing each person is modeled by (1)–(4); moreover, the values of all the model parameters are the same as those employed in Sections III-B and V-A.
2) The signal models expressed by (39) and (40) have been adopted.

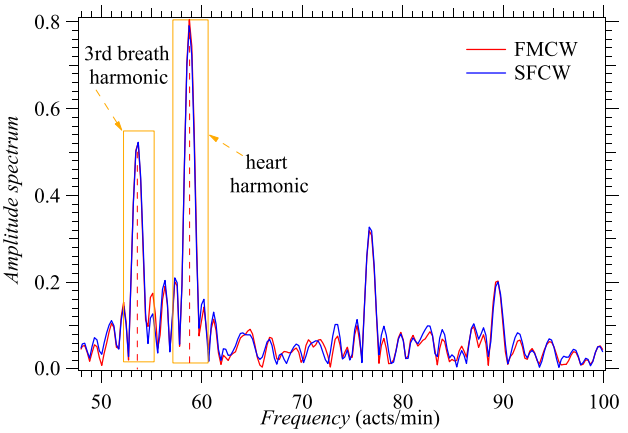

Fig. 13. *Representation of the amplitude spectrum of the sequence generated through BPF of the phase vector $\hat{\psi}$ shown in Fig. 11. The dashed vertical lines identify the exact values of BR and the third harmonic of HR. Both FMCW and SFCW radar systems are considered.*

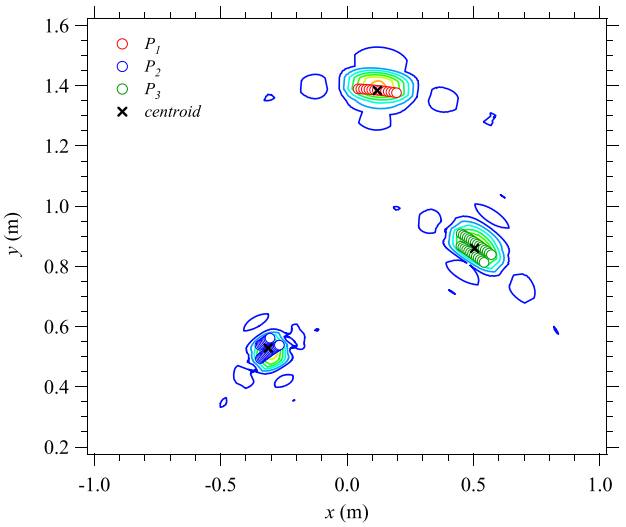

Fig. 14. ***Contour plot of the range–azimuth map generated based on our synthetically generated data (an MIMO radar system is considered). The peaks P_1, P_2, and P_3 detected by the CFAR algorithm are identified by small circles, whereas black crosses indicate the position of the centroid of each cluster of peaks.***

3) The values of the parameters f_0, B, N, T_0, N_c, f_s, T_R, and μ of the MIMO radar are the same as those listed for the SISO FMCW radar considered above.
4) The MIMO radar is endowed with a virtual ULA like the one shown in Fig. 8(b); the overall number of VAs forming this array is $N_V = 16$, whereas the distance between adjacent virtual elements is $d = \lambda/4$.

Our data have been processed by the deterministic algorithm illustrated in Section V-B; $N_0' = 2$ and $N_A = 4$ have been selected in the computation of the 2D-FFT output $\mathbf{X}_n$ (69). The range–azimuth map $\mathbf{J}[0]$ generated based on the measurements acquired through the MIMO radar in the first chirp interval is represented in Fig. 14. The peaks detected by the CFAR algorithm are indicated by small circles, whereas black crosses are used to identify the centroids[18] of each cluster of adjacent peaks. The elements of the phase vector $\hat{\psi}$ (48) and of its amplitude spectrum in correspondence of the centroid obtained for the first (closest to the radar) target are shown in Fig. 15(a) and (b), respectively, whereas the estimates of the positions of the three subjects together with the estimates of their BR and HR are listed in Table 3. From these results, the following conclusions can be easily inferred that the following conditions hold.

1) The range–azimuth map allows to detect all the subjects and estimate their position.
2) The phase vector associated with each centroid provides important information about the dynamic of the chest displacement of the subject associated with it.
3) The position and vital signs estimated for each subject are reasonably accurate.

[18]Note that each centroid represents the position estimated for one of the subjects.

Table 3 Exact Values and Corresponding Estimates of the Range (R), Azimuth (θ), BR (b_r), and HR (h_r) of Three Distinct Subjects

Person	R (m)	$\hat{R}$	θ (°)	$\hat{\theta}$	b_r acts/min	$\hat{b}_r$	h_r acts/min	$\hat{h}_r$
S_1	0.60	0.61	-30	-30.5	14.0	13.8	70	66.8
S_2	1.00	1.01	30	30.3	17	16.9	66.0	63.1
S_3	1.40	1.39	5	4.9	20.0	19.8	57.0	55.6

D. Detection and Estimation Algorithms Exploiting LB Methods

Various deterministic algorithms may fail in complicated, highly dynamic, and time-varying scenarios [55]. In such cases, LB methods and, in particular, ML and DL techniques [84], may be extremely useful since they are able to: 1) learn the regularities characterizing the raw data acquired by radar systems and 2) automatically extract information from them. Note that, on the one

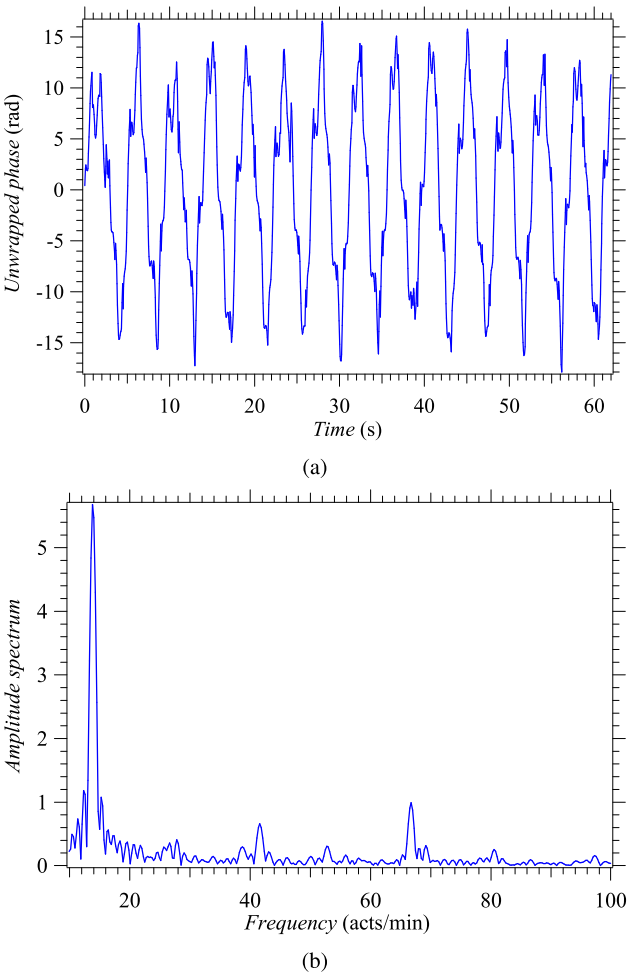

Fig. 15. ***Representation of (a) elements of a phase vector generated on the basis of the measurements acquired through an MIMO FMCW radar during a single chirp interval and (b) its amplitude spectrum. The target closest to the radar is considered.***

hand, ML techniques exploit a customized set of features, manually extracted from the available raw data by means of different processing techniques. On the other hand, DL techniques can learn specific data patterns and extract useful information directly from the same data through the use of neural networks; this approach requires limited expertise on signal analysis in radar systems. Each class of methods includes supervised and unsupervised learning techniques. Generally speaking, supervised techniques, mainly used for solving classification or regression problems, are based on the idea of exploiting a labeled dataset for learning from them through a specific procedure, called training. Training aims at the identification of the model, i.e., at estimating of the probability density function (also called predictive distribution) on the basis of which the available dataset has been generated. Given the model learned during training (i.e., the predictor), the label associated with a completely new observation or the value of a continuous variable related to it can be predicted in a way that a specific loss (known as generalization loss) is minimized; such tasks are known as classification and regression. The well-known ML methods for classification are the K-NN, the SVM, and the ensemble classifier [85].

Unsupervised methods, instead, do not require a labeled dataset and learn some specific properties of the mechanism on which the generation of the considered dataset is based. They can be exploited to solve specific technical problems, such as data clustering, dimensionality reduction, and feature selection. In practice, data clustering aims at partitioning the available dataset in a number of groups such that data points in the same group are dissimilar from the data points belonging to all the other groups. Dimensionality reduction is employed to generate a reduced dimensionality representation of the observations, whereas feature selection consists in deriving a vector-valued function that produces a useful and lower dimensional representation of the available feature.

In general, the dataset employed to train a specific LB method contains N_t couples, each of which consists of a D_r-dimensional real vector of features and a D_t-dimensional real vector of labels. The size N_t of the dataset can be reasonably small in the case of ML (say, between a few dozen and a few hundred) but is substantially larger in the case of DL (say, at least one thousand). In the case of radar-based monitoring of vital signs, a vector of customized features can be obtained from the phase vector $\hat{\psi}$ (48) through a procedure called feature extraction and can be processed for classification purposes. For instance, different breathing diseases could be recognized based on several features, such as the breathing frequency, the chest displacement, and the variability of the breathing frequency in short and long observation times. Generally speaking, for all the radar topologies, the extracted features can be grouped into three different classes, namely, time, short-term, and time–frequency domain features. Time features are represented by various characteristics of the evolution of the elements of the phase vector $\hat{\psi}$,

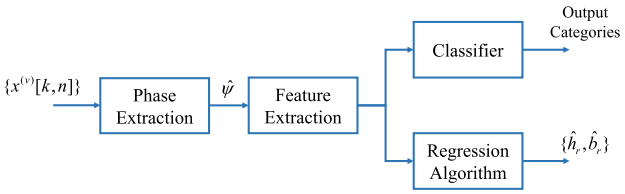

Fig. 16. ***Block diagram representing the signal processing chain of a radar-based system employing an LB method for vital signs monitoring.***

such as their average (or maximum) peak amplitude, the variability of their amplitude, and the number of peaks. Short-time features (time–frequency domain features),[19] instead, allow to monitor how the energy (the spectral content) of the elements of the phase vector $\hat{\psi}$ evolves over time. The abovementioned features can be employed for both classification and regression, as exemplified in Fig. 16, where the overall signal processing chain of a radar system employing an LB method is illustrated.

An alternative to ML methods is provided by DL methods. In the last case, feature extraction is automatically accomplished by a neural network and, if classification is required, a softmax layer is employed to evaluate the probability that a certain observation is associated with one of the given classes.

A limited literature on the use of ML and DL methods in radar-based monitoring of vital signs is available. The use of ML methods in CW Doppler radar systems for vital signs monitoring has been investigated in [86], [87], [88], and [89], while an unsupervised method for DC offset and clutter suppression using FMCW radars has been investigated in [90]. Moreover, an HR estimation technique based on a CNN has been developed in [91] for an IR-UWB radar system. In particular, supervised methods have been exploited for classifying breathing disorders, heart sound classification and for removing the high-order harmonics from the phase vector ψ (48) in [87], [89], and [86], respectively. An artificial neural network (ANN) for the reliable detection of heartbeats through a CW Doppler radar has been proposed in [88]. The adopted ANN is composed by a cascade of multiple layers with a different number of neurons and its architecture is quite simple; its main drawback is represented by its inability to cope with time series, i.e., to extract features related to the time evolution of the observed signal.

VI. SOME CONSIDERATIONS ON RADAR SELECTION AND ON ITS USE IN EXPERIMENTAL CAMPAIGNS

In this section, we illustrate some important lessons that we have learned from our experimental work conducted on healthy adult volunteers in the laboratories of the Department of Engineering "Enzo Ferrari" and of the Car-

[19]Different tools for time–frequency analysis, such as the CWT and the STFT, can be employed to extract these features.

diology Division, Department of Biomedical, Metabolic and Neural Sciences, University of Modena and Reggio Emilia, Modena, Italy. First, we focus on the essential requirements that radar devices employed for vital signs monitoring should meet. Then, we provide some guidelines for developing an experimental setup and illustrate some numerical results about the estimates of vital signs extracted from our experimental measurements. Finally, we comment on how to assess estimation accuracy in vital signs monitoring.

A. Fundamental Requirements of Radar Devices

Nowadays, a number of compact radar devices, not explicitly developed for medical applications and operating in the mm-wave spectrum, are available on the market at various prices. A radar system employed for vital signs monitoring needs to satisfy various technical requirements that are influenced by the environment in which measurements are acquired [92]. These requirements concern: 1) the maximum distance of the radar from the body of the subject under test; 2) its bandwidth and its operating frequency f_0; 3) its displacement resolution; and 4) its angular resolution. Different values of the parameters mentioned above may have a substantial impact on the achievable accuracy, as illustrated in the following.

The maximum distance at which a radar should operate depends on the considered application. If long-range detection is required, a high transmission power and/or highly directive antennas should be employed to guarantee a proper SNR at the RX side [93]. The power radiated by colocated MIMO radars employed in vital signs monitoring is small; however, in this case, beamforming techniques can be employed to constructively combine the signals received by multiple antennas, thus enhancing the overall SNR. It is also important to keep in mind that any radar system, independently of its antennas and maximum radiated power, is characterized by a maximum unambiguous range (denoted $R_{\max}$), that is, by a maximum distance beyond which target range is not correctly estimated. In the case of FMCW or SFCW radars, $R_{\max}$ can be expressed as[20]

$$R_{\max} = N\frac{c}{4B} \tag{78}$$

where B is the bandwidth of the radiated signal and N is the overall number of samples acquired in a chirp interval (frequency sweep) by an FMCW (SFCW) radar. Then, for a given bandwidth, $R_{\max}$ can be raised by increasing N, i.e., by adopting a higher sampling rate at the RX side.

The bandwidth of the radiated signal plays a fundamental role in radar-based monitoring of vital signs. In fact, a larger bandwidth results in a better range resolution, i.e., in an improved ability to discriminate multiple targets in range as well as to generate a more detailed image of an extended target. Since the bandwidth is usually a fraction of the carrier frequency, this consideration has motivated the adoption of operating frequencies that fall in the mm-wave spectrum, i.e., that belong to the frequency range[21] (30, 300) GHz. The selection of a higher operating frequency (i.e., of a shorter wavelength λ) has various implications. First, it leads to a higher phase sensitivity, that is, to faster changes in the received signal phase observed in the presence of the small movements to be detected in vital signs monitoring [see (11)–(13)]. This is certainly beneficial, provided that the phase ambiguity problem does not arise (i.e., that the observed phase variations remain within the range $(-\pi, \pi)$). The last problem can be circumvented by increasing the sampling rate of the received signal; this has also a beneficial effect on the maximum range at which a target can be detected, as already mentioned above. A change in the operating frequency of the radar has also a significant impact on the penetration depth of the radiated EM waves through human tissues [21]. Readers should keep in mind that: 1) microwave signals are partially reflected and partially absorbed by the human skin [94]; 2) the attenuation of the reflected EM field increases with its frequency; 3) the penetration through human skin, instead, decreases with frequency (for instance, the skin penetration depth is 2.7 mm at 10 GHz and just 0.5 mm at 60 GHz [95], [96]); 4) the EM wave reflection due to body tissues becomes stronger as the operating frequency increases; and 5) the quality of the echo of an mm-wave radar is negligibly affected by the thickness of the clothes of the monitored subject [97]. Based on these results, we can state that, when an mm-wave radar device is employed in vital signs monitoring of a still subject, the phase and amplitude fluctuations observed in its received signal really originate from the chest and skin displacement stimulated by his/her cardiopulmonary activity.

The displacement resolution can be defined as the minimum measurable displacement over two consecutive frames transmitted by the considered radar device (such frames are separated by a time interval lasting T_0 s, see Section IV-B). Based on (61), the displacement $\Delta R_{k,k+1}$ experienced by a point target between the kth frame and the subsequent (i.e., the $(k+1)$th) frame can be expressed as

$$\Delta R_{k,k+1} = \frac{\lambda}{4\pi}\Delta\psi_{k,k+1} \tag{79}$$

where $\Delta\psi_{k,k+1}$ is the phase variation observed in the electromagnetic echo. If $\delta_{b,M}$ denotes the maximum chest displacement due to breathing (see Section III-B), the inequality

$$\frac{\Delta R_{k,k+1}}{T_0} \geq \frac{2\delta_{b,M}}{T_{\mathrm{BR}}} \tag{80}$$

[20] If an FMCW radar system is considered, this result originates from the fact that the frequency f_n (21) can be unambiguously estimated if it does not exceed half the sampling frequency $f_s \triangleq 1/T_s$.

[21] The corresponding wavelengths range from 1 and 10 mm.

should be satisfied to achieve a sufficient resolution in detecting chest movements. The last inequality can be rewritten as

$$T_0 \leq \frac{T_{\mathrm{BR}}}{2\delta_{b,M}} R_{k,k+1} \tag{81}$$

or, equivalently, as

$$T_0 \leq \frac{T_{\mathrm{BR}}}{2\delta_{b,M}} \frac{\lambda}{4\pi} \Delta\hat{\psi}_{k,k+1} \tag{82}$$

due to (79). If we assume that $\delta_{b,M}$ is equal to 4λ (where $\lambda \cong 4$ mm, if the employed radar system operates at 77 GHz) and keep in mind that[22] the inequality $\Delta\psi_{k,k+1} < 2\pi$ must be satisfied to avoid any phase ambiguity, from (82), it is easily inferred that

$$\frac{1}{T_0} > \frac{16}{T_{\mathrm{BR}}} \tag{83}$$

so that the selected frame rate must be substantially higher than the breathing frequency. Similar considerations can be formulated for the displacement due to heart activity; the only difference is represented by the fact that T_{BR} is replaced by T_{HR}. Then, achieving sufficient accuracy in the estimation of BR and HR requires the selection of a proper frame rate $1/T_0$. In practice, as already mentioned in Section III-A, the typical values of BR at the rest range from 10 to 25 acts/min (i.e., from 0.2 and 0.4 Hz), whereas those of HR from 50 to 100 acts/min (i.e., from 1 to 1.67 Hz); under stress conditions, the BR and HR increase up to 40 acts/min (0.67 Hz) and 180 acts/min (3 Hz), respectively. Therefore, based on (83), the frame rate should be on the order of 25 Hz at rest and 45 Hz under stress. It is also worth mentioning that, whatever the selected frame rate, a sufficiently long observation time is required to generate reasonably accurate estimates of vital signs through spectral analysis. In practice, using a commercial MIMO radar, such estimates should be extracted from the radar measurements acquired on a time interval that covers at least three periods of breathing (and, consequently, about ten periods of heartbeat), i.e., lasting at least 10 s at rest; this unavoidably introduces some latency in vital sign estimation.

Let us focus now on the angular resolution. This parameter plays an important role when an MIMO radar is employed to detect the vital signs of multiple people, characterized by different angular coordinates. The achievable angular resolution is strictly related to the number of virtual channels N_V made available by the employed radar system. If this system is endowed with a single ULA characterized by N_V equally spaced channels, the angular resolution $\Delta\theta$ can be evaluated as

$$\Delta\theta = \frac{\lambda}{2d\,(N_V - 1)} \frac{180^\circ}{\pi} \tag{84}$$

where d is the distance between two adjacent virtual elements; for instance, if $d = \lambda/4$, the resolution is equal to $2/(N_V - 1)$ rad.

In our measurement campaigns performed in a hospital environment (see Section VI-B), two colocated FMCW radars, namely, the IWRxx43 TI radar [98] and the P2G FMCW radar[23] [99], have been employed. The former device is manufactured by TI and operates at the frequency $f_0 = 77$ GHz, whereas the latter one is manufactured by Infineon and operates at the frequency $f_0 = 24$ GHz; the difference in their transmission frequencies allowed us to assess the potential advantages originating from the use of higher frequencies and/or from the exploitation of frequency diversity. The front end of these devices is shown in Fig. 17. It is important to note that in our application $T_F = 60$ s, i.e., the duration of each transmitted frame is equal to that of the whole observation interval and the chirp duration $T_0 = T + T_R$ is characterized by a long reset time since $T_R > T$.

The TI radar is endowed with an array composed by $N_T = 3$ ($N_R = 4$) TX (RX) antennas [see Fig. 17(a)]; therefore, it makes available a virtual array consisting of $N_V = 3 \cdot 4 = 12$ (virtual) antenna elements [see (35)]; these elements form two different horizontal ULAs composed by $N_{\mathrm{HULA}_1} = 8$ and $N_{\mathrm{HULA}_2} = 4$ virtual channels; therefore, only $N_{\mathrm{VULA}} = 2$ aligned channels are available along the vertical direction. The horizontal (i.e., azimuthal) resolution and the vertical (i.e., elevation) resolution are $\Delta\theta \simeq 16.6^\circ$ and $\Delta\phi = 45^\circ$, respectively [see (84)]. In our work, the following values of the radar parameters have been selected: 1) frequency slope $\mu = 86$ MHz/μs; 2) overall number of samples per chirp $N = 256$; 3) ADC sampling frequency $f_s = 9$ MHz; and 4) chirp duration $T_0 \approx 60$ ms. These choices entail that: 1) the

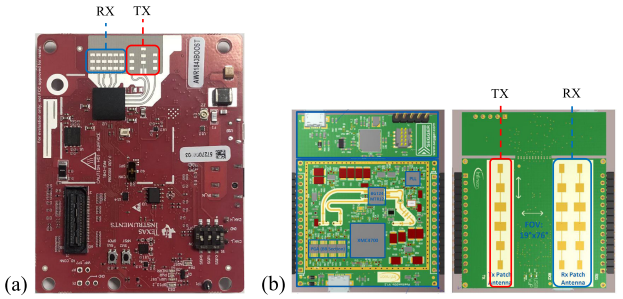

Fig. 17. ***Photographs of (a) IWRxx43 radar front end and (b) both sides of the P2G module.***

[22]This expression is valid if the $\arctan 2(\cdot)$ operator is employed, as illustrated in Section V-A.

[23]Detailed descriptions of these devices are available at https://www.ti.com/tool/IWR1843BOOST and at https://www.infineon.com/cms/en/product/evaluation-boards/demo-position2go/

Fig. 18. *Photographs of both sides of the XM112 UWB radar.*

bandwidth of the radiated signal is $B = \mu T \simeq 2.45$ GHz since the ramp-up time is $T = N/f_s = 18.4$ μs and 2) the maximum unambiguous distance is $R_{\max} \simeq 15.67$ m [see (78)].

The P2G radar is equipped with an array composed by $N_T = 1$ TX and $N_R = 2$ RX antennas (see Fig. 17(b)]. Therefore, a virtual array of $N_V = 1{\cdot}2 = 2$ virtual elements [see (35)], forming a horizontal ULA, is available. In our work, the following values of the radar parameters have been selected: 1) $\mu = 0.78$ MHz/ms; 2) overall number of samples per chirp $N = 256$; 3) ADC sampling frequency $f_s = 1$ MHz; and 4) chirp duration interval $T_0 \approx 60$ ms. In this case, the ramp-up time is $T = N/f_s = 256$ μs, the bandwidth of the radiated signal is $B = 200$ MHz, and the maximum unambiguous distance is $R_{\max} = 192$ m. Therefore, this radar device can be employed for long-range applications but achieves a lower range resolution than the TI IWR1843 radar.

A short measurement campaign was also conducted in an office environment (see Section VI-B). In that case, an XM112 PCR UWB radar has been employed (see Fig. 18). This device, manufactured by Acconeer,[24] operates at the frequency $f_0 = 60$ GHz and is of SISO type. Its PRI T_0 is equal to 76.9 ps, its transmission frame consists of $N_c = 621$ pulses, and its range resolution is equal to 0.5 mm. Acquiring our measurements from the XM112 UWB radar, a minimum (maximum) range $R_m = 50$ cm ($R_M = 80$ cm) has been assumed since the distance of the monitored subject from the radar itself always belonged to the interval $[R_m, R_M]$.

B. Data Acquisition

The typical differences between the datasets analyzed in the technical literature about radar-based monitoring of vital signs concern (see Table 6):

1) the overall number of subjects involved in the data acquisition procedure;
2) the heterogeneity of the acquired dataset and, in particular, the positions of the involved subjects with respect to the employed radar (e.g., sitting and lying down) and their physical conditions (e.g., in a rest condition, under strain, sleeping, and so on).

[24]See https://www.acconeer.com/company/ for further details.

The overall number of subjects ranges from few units to a few dozens. Readers should keep in mind that the analysis of deterministic and ML methods does not usually require a large number of measurements, whereas that of DL techniques needs large and heterogeneous datasets. For instance, the measurements analyzed in [100] have been acquired from ten people (more precisely, six males and four females), whose distance from the employed radar system ranged from 20 to 80 cm. On the contrary, a much larger dataset was needed to train and test an LSTM network in [101]. In the last case, the overall acquisition time of the whole dataset is equal to 18 900 s (corresponding to approximately 5 h); moreover, the acquired measurements refer to 30 different subjects.

The heterogeneity of the acquired dataset can be improved by observing the considered subjects in different positions (e.g., in front of the radar with the chest facing toward the antennas or on its left/right side) but always at a fixed distance from the employed radar systems [29]. Subjects can also be placed at different distances from radar systems, but, in this case, their angular coordinates should not change (see, e.g., [100, Sec. III]).

The measurements analyzed in most of the technical literature refer to people breathing at rest. However, especially in last years, contactless systems based on radar technology have been employed for HR and BR monitoring of subjects in different breathing conditions. For instance, the measurements of the dataset employed in [102] have been acquired in apnea, during the Valsalva maneuver[25] and in two different positions (tilt-up and tilt-down).

The selection of proper reference sensors represents another important technical issue to be considered before starting a measurement campaign. In fact, the data collected from reference sensors are always required for the validation of deterministic algorithms [67], [103] or for training LB methods [91]. In the measurement campaigns described in the technical literature, various medical instruments, such as electrocardiographs and wearable sensors, have been used. Wearable sensors include elastic bands with built-in electrodes [104], MEMS, pulse oximeters, or Bragg grating sensors [105]. Most of the commercially available wearable sensors are easy to use since they provide excellent user interfaces and APIs for Python or MATLAB programming environments. However, an important issue to be considered before selecting a specific reference sensor is the possibility of accurately synchronizing the timing of its measurements with that of the data provided by the employed radar device.

A long measurement campaign is being conducted by the authors of this article at the Cardiology Division, Department of Biomedical, Metabolic and Neural Sciences, University of Modena and Reggio Emilia (Hospital of

[25]The Valsava maneuver is performed by moderately forceful attempted exhalation against a closed airway; this can be practically implemented by expiring against a closed glottis.

Fig. 19. ***Photograph of the setup employed in our measurement campaigns conducted in the hospital; both the IWRxx43 and the P2G radars are used.***

Modena), on healthy adult volunteers.[26] The experimental setup adopted in this case is shown in Fig. 19. The two FMCW radar sensors described in Section VI-A are mounted on a wooden bar, which, in turn, is put on a tripod. Moreover, their antenna arrays are oriented toward the chest of each subject, always lying down a bed, whose upper part is slightly tilted. The typical vertical (horizontal) distance d_h (d_v) between the radars (the tripod) and the subject under test is approximately equal to 75 cm (50 cm); our tripod allows to move up or down the radars so that the distance between them and the monitored subject can be modified. In our measurements, different positions are being considered for the subject under test. In practice, he/she is sitting or lying down on the bed with different tilting angles; in the first case, his/her movements are very small and this makes the estimation of HR and BR potentially very accurate, whereas, in the second one, the tension of his/her muscles may affect the estimation of vital sign parameters. In our setup, the reference sensor is the Shimmer3 device manufactured by Shimmer [106]. This device, controlled by means of a simple user interface, is able to send data over a Bluetooth connection and is equipped with five electrodes (right hand side midaxillary, left-hand side midaxillary, right leg, left leg, V1; see [106, p. 6, Fig. 3-2]), which need to be placed in specific positions of the chest of the subject under test. In our acquisitions, the reference ECG signal is read from the voltage difference between the left leg and RHS midaxillary (LL-RA) electrodes. The breathing signal, instead, is generated by measuring the impedance between these two electrodes; in practice, these electrodes are used to inject a weak high-frequency (10 kHz) alternating current in the chest tissues and the voltage variations due to chest displacement are measured. Then, an estimate of the chest impedance variations is obtained by computing the ratio between the measured voltage and the injected current; finally, breathing dynamics are inferred from such variations (further details about this method can be found in [107]).

Due to the availability of a proper API, Shimmer3 measurements can be easily synchronized in time with those acquired through the IWRxx43 radar or the P2G radar so that data acquisition can be accomplished in real time. In fact, the Shimmer3 device offers the possibility of sharing the time reference (namely, the CPU timestamp) with our radar devices; this has allowed us to synchronize the reference and the probing signals with great accuracy. As already mentioned above, in our experiment, each data acquisition refers to an observation interval lasting $T_F = 60$ s. However, since the radars and the reference sensor are characterized by different frame rates, the samples of each of the two signals (namely, the ECG and breathing signals) provided by the Shimmer3 sensor are stored in a sequence of vectors, each having size $N_{c,S} = 15317$, whereas the received signal samples provided by the IWRxx43 (P2G) radar are stored in a 3-D matrix of size $N \times N_V \times N_{c,\mathrm{TI}} = 256 \times 4 \times 997$ ($N \times N_V \times N_{c,\mathrm{P2G}} = 256 \times 2 \times 933$). It is also worth mentioning that, in general, if the construction of a dataset requires that acquisitions originating from the given reference sensor and those coming from the employed radar device have the same length, a subsampling or upsampling procedure can be adopted for the reference or the radar signals.

Independently of the nature of the algorithm to be tested on the acquired measurements, it is highly recommended to build up a reasonably large dataset since the chest dynamics of distinct subjects can exhibit very different characteristics. Moreover, in our measurement campaigns, in order to guarantee a sufficient variability in the generated dataset, the subjects under test are being observed in different conditions. In practice, the following conditions are considered in our data acquisitions: 1) breathing normally, at rest; 2) during inspiratory (expiratory) apnea (for as long as he/she could, ending the acquisition with normal breathing); 3) hyperventilating (for as long as he/she could); 4) during the Valsalva maneuver; and 5) after making an effort. In the last case, the subject under test is required to move up a step and down from it for at least one minute).

As already mentioned in Section VI-A, an additional measurement campaign has also been conducted in a different environment and, in particular, in one of the research laboratories of the Department of Engineering "Enzo Ferrari." The experimental setup adopted in this case is shown in Fig. 20. An XM112 IR-UWB radar has been mounted on a small tripod, which, in turn, has been positioned on an office desk in front the chest of the monitored subject (sitting on chair at a horizontal distance

[26]Original data will be made available upon submission of a reasonable request to the authors.

Fig. 20. ***Photograph of the setup employed in our measurement campaign conducted in a university laboratory.***

d_h approximately equal to 70 cm). Our measurements have been acquired from five healthy subjects; the resulting dataset consists of $\bar{N} = 45$ waveforms, each referring to an observation interval that lasts $T_F = 60$ s and represented by $N_{c,\mathrm{AC}} = 5926$ complex samples. The Shimmer3 device has been employed again as a reference sensor and its output has been synchronized with that of the XM112 device. The data collected by the reference sensor have been stored in a vector of size $N_{c,S} = 15\,317$, assuming an average frame rate equal to 100 samples per second.

C. Numerical Results

In this section, the estimation methods described in Section V-A are applied to the measurements acquired through our three radar devices described in Section VI-A. Our objective is estimating the BR and HR in the following two scenarios: 1) a single subject lying down on a bed at a distance $R_{\mathrm{ref}} = d_v = 0.75$ cm from the radar sensor (see Fig. 19) and 2) a single subject sitting on chair at a horizontal $d_h = 70$ cm from the radar sensor (see Fig. 20). In our study, emphasis is put on the extraction of HR from radar measurements since this represents a substantially more challenging task than BR estimation.

Let us focus now on the first scenario. In this case, the signal samples acquired through the four (two) VAs of the IWRxx43 (P2G) radar in the kth chirp interval with $k = 0, 1, \ldots, N_{c,x} - 1$ and $x =$ TI (P2G) are processed by a beamforming algorithm [45]; this allows to constructively combine the echoes impinging on the RX array along a specific direction and to produce a single Nth dimensional column vector $\mathbf{x}_k$; this vector feeds the range estimation and bin selection block shown in Fig. 10. The processing accomplished by the last block is based on (62) (a tape meter is used to compute the reference range R_{ref}). Moreover, this block produces the couple $(\hat{l}\,[k],\ \hat{\psi}[k])$, consisting of the bin index $\hat{l}\,[k]$ and the phase estimate $\hat{\psi}[k]$, for any k. It is worth mentioning that: 1) an estimate $\hat{R}[k]$ of the target range is evaluated as

$$\hat{R}\,[k] = \hat{l}\ [k]\ K_m \tag{85}$$

where

$$\hat{l}\ [k] = \arg \max_{l_m \le \bar{l} \le l_M} |X\,[l, k]\,|^2 \tag{86}$$

$X[l, k]$ is defined by (62), $l_m = 21$, $l_M = 33$, $K_m = 32.6$ m ($l_m = 2$, $l_M = 3$, and $K_m = 2.6$ m) for $x =$ TI ($x =$ P2G) and 2) $N_0 = 512$, $R_m = 0.65$ m, and $R_M = 1$ m have been selected for both radar systems. Note that $\hat{R}[k]$ (85) does not necessary coincide with the reference range R_{ref} since the following conditions hold.

1) Some errors are unavoidably introduced in the range measurement procedure. In fact, it is not easy to identify exactly the point of the chest on which the beam radiated by the employed radar is focused since the antennas of both radar devices are not highly directive.
2) The range estimate $\hat{R}[k_1]$ computed in the k_1th chirp interval may be slightly different[27] from the estimate $\hat{R}[k_2]$ obtained in the k_2th chirp interval, with $k_1 \neq k_2$.

The elements of the unwrapped phase vector

$$\hat{\boldsymbol{\psi}} \triangleq [\hat{\psi}\,[0]\,, \hat{\psi}\,[1]\,, \ldots, \hat{\psi}\,[N_{c,x} - 1]]^T \tag{87}$$

computed on the basis of the measurements that have been acquired through the TI (P2G) radar in a single observation interval are represented by the red (green) line

[27]Note that, in principle, information about chest displacement is contained in the sequence $\{\hat{R}[0], \hat{R}[1], \ldots, \hat{R}[N_{c,x} - 1]\}$, but, in general, its elements are too noisy for reliable detection of vital signs.

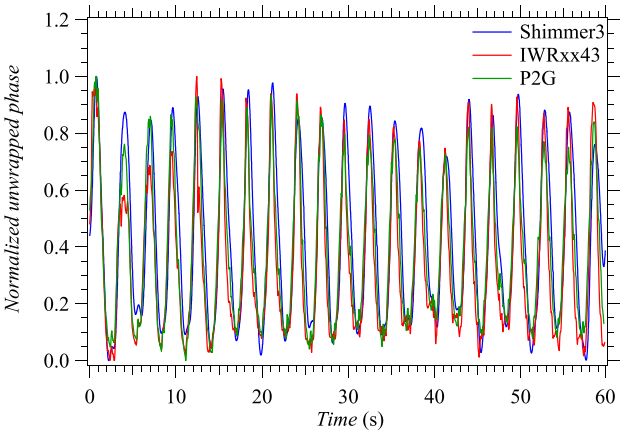

Fig. 21. ***Representation of the normalized unwrapped phase extracted from our IWRxx43 radar measurements (red line) and P2G radar measurements (green line). The breath signal acquired through our reference sensor is also shown (blue line).***

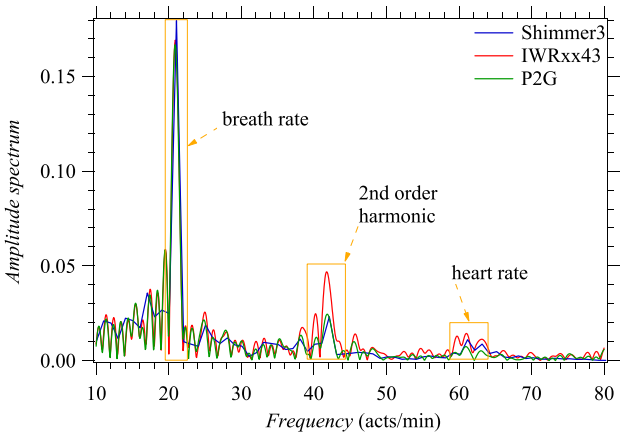

Fig. 22. *Representation of the amplitude spectrum of (a) breath signal acquired through our reference sensor (blue line) and (b) normalized unwrapped phase extracted from our IWRxx43 radar measurements (red line) and P2G radar measurements (green line).*

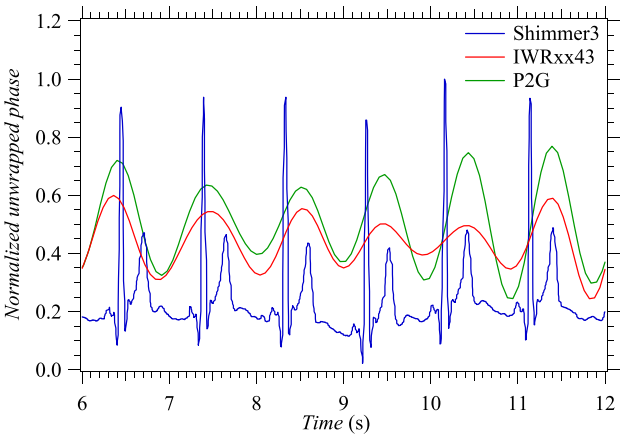

Fig. 23. *Representation of the heart signal (normalized unwrapped phase) extracted from our IWRxx43 radar measurements (red line) and P2G radar measurements (green line). The ECG signal acquired through our reference sensor is also shown (blue line).*

in Fig. 21 (note that in order to ease the interpretation of these results, the elements of the two phase vectors have been normalized[28]); in this case, AD followed by DC offset removal and phase unwrapping is employed. The results shown in Fig. 21 deserve the following comments: 1) the two radar signals represent the dynamics of the chest due to both breathing and cardiac activities and 2) the phase trajectories computed based on the measurements provided by the two radars overlap, even if these devices operate at different frequencies and exhibit similar evolutions as the signal provided by our reference sensor (Shimmer3; see the blue line appearing in Fig. 21). The amplitude spectrum generated by applying an FFT of order $N_0' = N_{c,S} = 15\,317$ to each of the signals represented in Fig. 21 is shown in Fig. 22. These results evidence that: 1) the spectral peak associated with breathing (in correspondence of 21 acts/min) is much larger than the one related to heart beat (visible at approximately 61 acts/min) and 2) the second-order harmonic of breathing is clearly visible at approximately $21 \times 2 = 42$ acts/min, whereas its third harmonic is expected at $21 \times 3 = 63$ acts/min.

The heart signal can be extracted from the unwrapped phase through BPF [28]. In this case, a fourth-order bandpass Butterworth is used to select the spectral components whose frequencies belong to the interval [0.91, 3] Hz; its output is shown, for both radars, in Fig. 23 (the ECG signal generated by the reference sensor is also represented). Note that, in the considered observation interval, the peak-to-peak period of the radar waveforms is comparable to the NN peak interval characterizing the ECG signal.[29] However, the heart and the ECG signal are not perfectly aligned; this suggests that the heart frequency, i.e., the distance between two consecutive peaks, is not completely stable during the observation time. This is confirmed by the amplitude spectrum of the bandpass filter output generated in response to the two radar signals; the resulting two spectra are represented in Fig. 24, where the amplitude spectrum of the response of the same bandpass filter to the breathing signal acquired by the reference sensor is also shown. Note that, in all these amplitude spectra, three spectral peaks are visible between 60 and 70 acts/min, i.e., in the frequency range in which the spectral contribution due to heartbeat is expected. This is due to the fact that: 1) the third-order harmonic of the breathing signal is close to the fundamental frequency of the heart beat so that the spectral contribution of the former signal may partially overlap with that of the latter one; 2) as suggested by

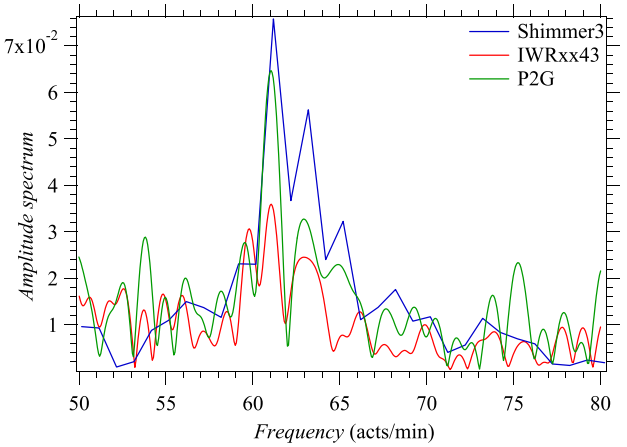

Fig. 24. *Representation of the amplitude spectrum of (a) heart signal acquired through our reference sensor (blue line) and (b) normalized unwrapped phase extracted from our IWRxx43 radar measurements (red line) and P2G radar measurements (green line).*

[28] A min–max normalization has been applied to the vector $\hat{\psi}$ (87); the kth element $\bar{\psi}[k]$ of the normalized phase vector is evaluated as $\bar{\psi}[k] = (\hat{\psi}[k] - \min(\hat{\boldsymbol{\psi}}))/(\max(\hat{\boldsymbol{\psi}}) - \min(\hat{\boldsymbol{\psi}}))$, with $k = 0, 1, \ldots, N_{c,x} - 1$.

[29] In an ECG signal, NN intervals are represented by the time intervals between adjacent peaks resulting from sinus node depolarizations.

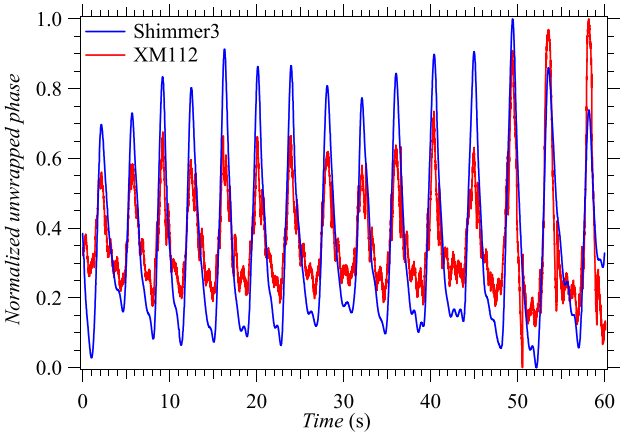

Fig. 25. ***Representation of the normalized unwrapped phase extracted from our XM112 radar measurements (red line). The breath signal acquired through our reference sensor is also shown (blue line).***

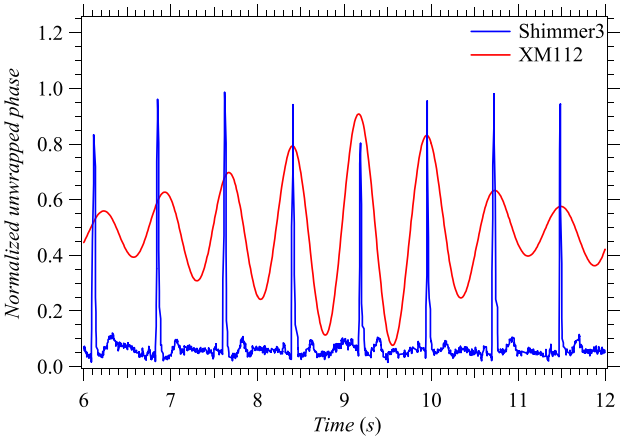

Fig. 27. ***Representation of the heart signal (normalized unwrapped phase) extracted from our XM112 radar measurements (red line). The ECG signal acquired through our reference sensor is also shown (blue line).***

the time-domain signals shown in Fig. 21, the HR changes during our observation interval (lasting 60 s) and this entails some spectral broadening. In principle, the last phenomenon can be mitigated by reducing the duration of the observation interval over which spectra are computed; however, an excessive shortening of this interval may lead to an inaccurate estimation of the frequency components due to heart activity.

Let us take into consideration now the second scenario. The signal processing chain employed in this case is represented in Fig. 9. The elements of a normalized unwrapped phase vector $\hat{\psi}$ (87), referring to a single observation interval and available after DC offset removal, are shown, together with the breath signal generated by our reference sensor, in Fig. 25. From these results, it is easily inferred that: 1) the phase evolution follows the dynamic of the chest of the monitored subject and 2) the dynamic of heart manifests itself as small fluctuations in the observed phase. The amplitude spectra generated by applying an FFT of order $N_0' = N_{c,S} = 15\,317$ to each of the signals appearing in Fig. 25 are shown in Fig. 26. The estimate of the BR, $\hat{b}_r = 13.8$ acts/min, is easily found by identifying the position of the main spectral peak; the amplitude of this peak is higher than that of the peak originating from heart, which is visible at the frequency $\hat{h}_r = 78$ acts/min. Note also that, similar to what has been observed in the first scenario, in the amplitude spectrum, three spectral peaks are visible between 70 and 80 acts/min, i.e., in the frequency range in which the spectral contribution due to heartbeat is expected. This is mainly due to the fact that the HR changes during the observation interval. In our signal processing chain, a fourth-order bandpass Butterworth filter has been employed to extract the heart signal from the unwrapped phase. This filter allows us to select the spectral components belonging to the interval [0.91, 3] Hz; its output is shown in Fig. 27, where the ECG signal generated by our reference sensor is also represented. Note that, in the considered observation interval, the peak-to-peak period of the radar waveform is comparable to the NN peak interval characterizing the ECG signal.

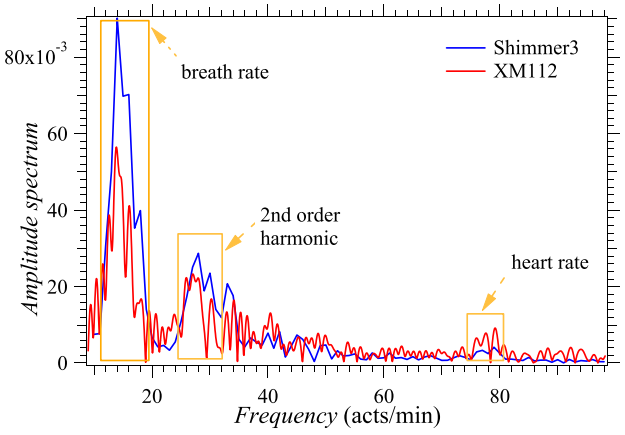

Fig. 26. ***Representation of the amplitude spectrum of (a) breath signal acquired through our reference sensor (blue line) and (b) unwrapped phase extracted from our XM112 radar measurements (red line).***

Finally, it is worth pointing out that the use of a bandpass filter represents a conceptually simple solution to the problem of extracting the HR components from the phase signal provided by a radar device. Actually, this filter needs to be adapted to the specific conditions of the patient under test. If his/her BR increases unexpectedly (e.g., in the case of hyperventilation), the spectral components associated with the breathing activity may not be canceled by this filter and may overlap with the components due to heart beat.

D. Estimation Accuracy

Let us suppose that an $\bar{N}$-dimensional set $\mathcal{D} \triangleq \{(\hat{b}_r\,,\,\hat{h}_r\,,\,b_r\,,\,h_r);\ r = 0, 1, \ldots, \bar{N}-1\}$, where $\hat{b}_r$ and $\hat{h}_r$

denote the estimates of the BR b_r and of HR h_r, respectively, is available after that all our radar-based measurements have been processed. Then, the accuracy achieved in vital sign estimation can be assessed by evaluating the MAE

$$\hat{\varepsilon}_{m,x} \triangleq \frac{1}{\bar{N}} \sum_{i=0}^{\bar{N}-1} |\hat{x}_r[i] - x_r[i]| \tag{88}$$

the PAE

$$\hat{\varepsilon}_x \triangleq \arg \max_{0 \le i \le \bar{N}-1} |\hat{x}_r[i] - x_r[i]| \tag{89}$$

and the RMSE

$$\bar{\varepsilon}_x \triangleq \sqrt{\frac{\sum_{i=0}^{\bar{N}-1} (\hat{x}_r[i] - x_r[i])^2}{\bar{N}}} \tag{90}$$

where $x = b$ ($x = h$) if BR (HR) is considered. Other relevant parameters are represented by the CV

$$\bar{\gamma}_x \triangleq \frac{\bar{\varepsilon}_x}{\frac{1}{\bar{N}} \sum_{i=0}^{\bar{N}-1} \hat{x}_r[i]} \tag{91}$$

and the Pearson coefficient

$$\bar{\rho}_x \triangleq \frac{\sum_{i=0}^{\bar{N}-1} (\hat{x}_r[i] - \bar{x}_r)}{\sqrt{\sum_{i=0}^{\bar{N}-1} (\hat{x}_r[i] - \bar{x}_r)^2}} \frac{\sum_{i=0}^{\bar{N}-1} (x_r[i] - \bar{x}'_r)}{\sqrt{\sum_{i=0}^{\bar{N}-1} (x_r[i] - \bar{x}'_r)^2}} \tag{92}$$

where

$$\bar{x}_r = \frac{1}{\bar{N}} \sum_{i=0}^{\bar{N}-1} \hat{x}_r[i] \tag{93}$$

$$\bar{x}'_r = \frac{1}{\bar{N}} \sum_{i=0}^{\bar{N}-1} x_r[i] \tag{94}$$

$x = b$ ($x = h$) if BR (HR) is considered and $x_r[i]$ represents the BR (HR) provided by the adopted reference sensor. Note that the value of the parameter ρ_x (92) falls in the interval $[-1, 1]$; a positive (negative) unitary value is found when the two available datasets (namely, the dataset generated through the employed radar device and that acquired from the reference sensor) exhibit a positive (negative) correlation, whereas a null value means that they are completely uncorrelated.

Typical values of the MAE, the RMSE, the CV, and the Pearson coefficient evaluated in radar-based monitoring of vital signs can be found in [67], [108], and [27]. In those articles, a reasonable estimation accuracy is achieved if: 1) the MAE and RMSE for BR (HR) estimation are in the order of some acts (beats) per minute; 2) the CV is close to 5% for both BR and HR estimation; and 3) the Pearson coefficient is greater than 70%. It is also important to remember that estimation accuracy can be improved through the development of a proper measurement setup; for instance, a small laser device can be employed to verify that the employed radar device is really pointing toward the center of the chest of the patient under test. Another relevant technical issue to be considered is represented, as already mentioned in Section VI-C, by the availability of an accurate synchronization between the radar and the reference sensor; unluckily, if the radar and reference devices have independent local clocks, full synchronization cannot be achieved and an accurate evaluation of the parameters defined above is not possible.

Table 4 RMSE ($\bar{\varepsilon}_x$), PAE ($\hat{\varepsilon}_x$), MAE ($\hat{\varepsilon}_{m,x}$), CV ($\bar{\gamma}_x$), and Pearson Coefficient (ρ_x) Referring to the BR (HR) Estimates $\{\hat{b}_r\}$ ($\{\hat{h}_r\}$) Computed Based on the Dataset Acquired in Our First Scenario (the Measurement Unit, m.u., Is Specified for Each Parameter)

Errors	m.u.	TI Radar	P2G Radar
$(\bar{\varepsilon}_b\,,\,\bar{\varepsilon}_h)$	acts/ min	(0.75 , 1.90)	(1.15 , 1.70)
$(\hat{\varepsilon}_b\,,\,\hat{\varepsilon}_h)$	acts/min	(2.80 , 4.80)	(5.50 , 4.00)
$(\hat{\varepsilon}_{m,b}\,,\,\hat{\varepsilon}_{m,h})$	acts/min	(0.45 , 1.60)	(0.60 , 1.40)
$(\bar{\gamma}_b\,,\,\bar{\gamma}_h)$	%	(4.40 , 3.24)	(6.80 , 2.90)
$(\bar{\rho}_b\,,\,\bar{\rho}_h)$	%	(90 , 82)	(84 , 85)

Let us now analyze some results obtained based on a limited set of the measurements acquired in the first scenario described in Section VI-B (and involving the IWRxx43 and P2G FMCW radars, and the Shimmer3 reference sensor). We assume that the following conditions hold.

1) All our measurements have been acquired from 13 young healthy subjects lying down on a bed and each of them refers to an observation interval lasting 60 s.
2) The HR and BR estimates have been computed by resorting to the processing chain described in Fig. 9 and in Section V-A1.
3) The size of the dataset $\mathcal{D}_{\rm TI}$ ($\mathcal{D}_{\rm P2G}$) referring to the IWRxx43 (P2G) radar is $\bar{N} = 45$ (on the average, three distinct measurements have been acquired from each subject).

The values of MAE, PAE, RMSE, and CV evaluated based on the available datasets are listed in Table 4, whereas the pairs $\{(b_r\,,\,\hat{b}_r)\}$ ($\{(h_r\,,\,\hat{h}_r)\}$) are represented on a Cartesian plane in Fig. 28 (Fig. 29) for both the IWRxx43 and P2G FMCW radars. Moreover, in Figs. 28 and 29, the lines generated through a linear fitting of the available pairs are also shown. These results deserve the following comments.

1) The estimates of BR and HR evaluated through both our radar devices are reasonably accurate.
2) Radar based-estimates are highly correlated with the measurements provided by our reference sensor.

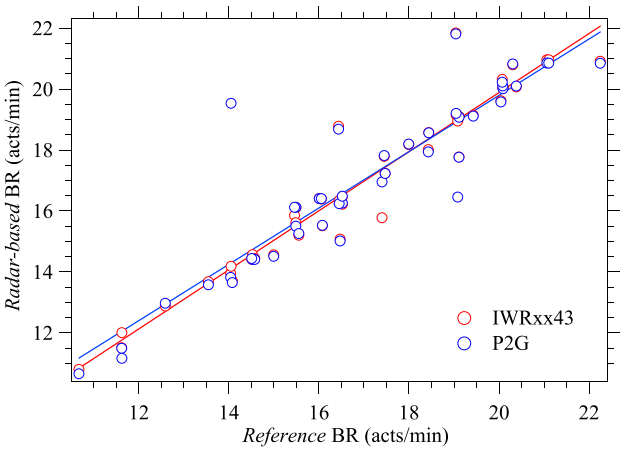

Fig. 28. *Representation of 45 couples $\{(b_r, \hat{b}_r)\}$; the BRs estimated through an IWRxx43 (P2G) radar are identified by a red (blue) marker.*

3) The IWRxx43 radar achieves a better accuracy on BR estimation than the P2G radar; on the other hand, the latter device outperforms the former one in HR estimation.
4) The accuracy of the HR estimates is worse than those of BR estimates since the latter rely on stronger and cleaner spectral information (see Figs. 24 and 26). Note also that the RMSEs and peak errors of HR are in the order of few acts/min.

As far as the last issue is concerned, it is important to keep in mind that: 1) the HR frequency may overlap with (or be very close to) the third-order harmonic of breath and 2) the displacement due to heart is very small and may be not fully detected by our radar devices, if they are not accurately oriented toward the chest of the subject under test.

Let us now analyze some results obtained based on all the measurements acquired in the second scenario described in Section VI-B (and involving the XM112 UWB radas and the Shimmer3 reference sensor). We assume that the HR and BR estimates have been computed through the processing chain described in Fig. 9 and in Section V. The pairs $\{(b_r, \hat{b}_r)\}$ and $\{(h_r, \hat{h}_r)\}$ obtained in this case are represented in Fig. 30, whereas the corresponding values of the parameters defined in this section are listed in Table 5. Comments similar to those expressed for the first scenario also apply to these results. In fact, the estimation errors estimated in the last case are comparable with those listed in Table 4 and referring to the two FMCW radars we employed.

Table 5 RMSE ($\bar{\varepsilon}_x$), PAE ($\hat{\bar{\varepsilon}}_x$), MAE ($\hat{\bar{\varepsilon}}_{m,x}$), CV ($\bar{\gamma}_x$), and Pearson Coefficient (ρ_x) Referring to the BR (HR) Estimates $\{\hat{b}_r\}$ ($\{\hat{h}_r\}$) Computed Based on Our Dataset Acquired in Our Second Scenario (the Measurement Unit, m.u., Is Specified for Each Parameter)

Errors	m.u.	XM112
$(\bar{\varepsilon}_b\ ,\ \bar{\varepsilon}_h)$	acts/ min	$(0.87\ ,\ 1.32)$
$(\hat{\varepsilon}_b\ ,\ \hat{\varepsilon}_h)$	acts/min	$(4.1\ ,\ 3.9)$
$(\hat{\varepsilon}_{m,b}\ ,\ \hat{\varepsilon}_{m,h})$	acts/min	$(1.32\ ,\ 1.75)$
$(\bar{\gamma}_b\ ,\ \bar{\gamma}_h)$	%	$(10.1\ ,\ 2.38)$
$(\bar{\rho}_b\ ,\ \bar{\rho}_h)$	%	$(78.8\ ,\ 97.5)$

VII. APPLICATIONS OF THE RADAR TECHNOLOGY TO VITAL SIGNS MONITORING

In this section, we propose a synopsis of the technical literature concerning the following specific issues: 1) the monitoring of HR and BR; 2) the experimental setups adopted in vital sign monitoring; and 3) the monitoring of heart sounds.

A. HR and BR Monitoring

The use of radar systems for monitoring HR and BR has been investigated by several research groups, whose work

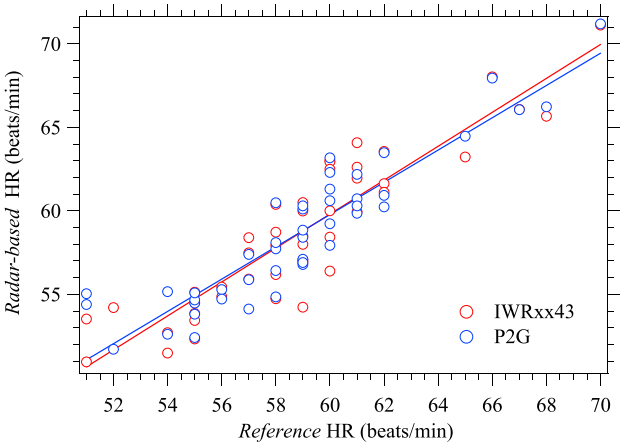

Fig. 29. *Representation of 45 couples $\{(h_r, \hat{h}_r)\}$; the HRs estimated through an IWRxx43 (P2G) radar are identified by a red (blue) marker.*

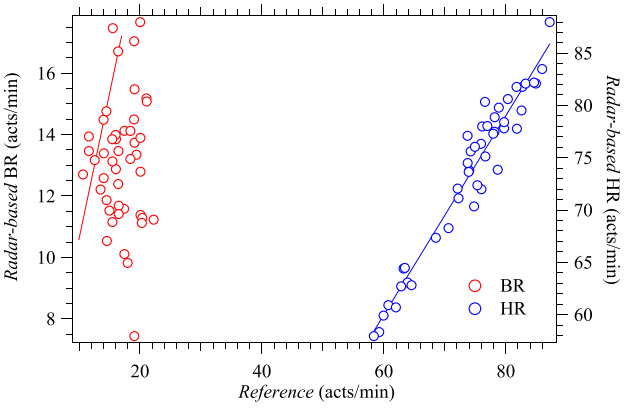

Fig. 30. *Representation of 45 couples $\{(b_r, \hat{b}_r)\}$ and $\{(h_r, \hat{h}_r)\}$ estimated on the basis of the measurements acquired through an XM112 UWB radar.*

has allowed to assess the performance achieved by different radar prototypes operating at distinct frequencies and radiating heterogeneous signals. As far as the use of the radar technologies described in Section IV-A is concerned, it is worth mentioning that the following conditions hold.

1) CW Doppler radars operating at 2.4, 5.8, and 24 GHz have been employed to measure respiration, heartbeat, or motion activity in [3], [109], [110], and [15]; in [111]; and in [88], [112], and [27], respectively. In [113], instead, a 24-GHz CW radar sensor is employed for cuffless blood pressure measurement, whereas in [114], a dual radar system operating at 5.8 and 120 GHz is adopted to measure respiration, heartbeat, HRV, blood pressure, and other vital parameters.
2) FMCW radars operating in the C- and X-bands at 24, 60, 77, and 122 GHz have been used to simultaneously estimate of the vital parameters of multiple people in [29], [115], and [116]; in [117] and [108]; in [67] and [38]; and in [118], respectively.
3) SFCW radars operating at frequencies lower than 3 GHz and in the X-band have been exploited for the estimation of the vital signs parameters of single or multiple people in [119] and [120] and in [121] and [122], respectively.
4) IR-UWB radars operating in the C-, X-, and E-bands and having large bandwidths (2–3 GHz) have been employed to measure vital parameters with high accuracy in [28], [74], [123], [124], [125], and [91].

MB and LB methods have been employed for the processing of the measurements provided by the above mentioned radar systems; moreover, such measurements have been acquired over population of different sizes. Essential information about the adopted processing methods and the size of the involved population are summarized in Table 6; note that, in this table, the size N_p of the population (low, L, medium, M, or high, H) on which it has been tested has been specified.[30] Some details about the most important processing methods and the main results achieved through their use are provided in the following.

1) CW Doppler Radars: Three novel deterministic techniques for estimating vital signs have been developed in [109], where a radar system operating at 2.4 GHz has been tested on a (single) human subject located at a fixed distance. These techniques are based on: 1) the FFT processing of the time-domain phase signal estimated through AD (see the block diagram represented in Fig. 9 and in Section V-A); 2) the computation of the autocorrelation of the phase vector $\hat{\psi}$ (48) to estimate the period of the time-domain phase signal; and 3) the FFT processing of the abovementioned autocorrelation. The last two techniques are shown to achieve a better accuracy than the first one. Other interesting results are offered in [3], in which a deterministic method based on the block diagram appearing in Fig. 9 is adopted to process the measurements acquired through an mm-wave Doppler radar. In that article, it is shown that the HR estimated based on an ECG is highly correlated with that estimated based on the measurements acquired through the devised radar system.

Some potential benefits originating from the use of ML methods are illustrated in [110], where the problem of recognizing and classifying breathing disorders of various patients during their sleep is investigated. Five ML techniques, namely, SVM, LDA, K-NN, DT, and ensemble learning techniques, trained on a manually selected set of features, are tested; the obtained results evidence that all the considered techniques are able to achieve a high accuracy in the classification of breathing disorders.

2) FMCW Radars: In [117], the BR and HR of a single person have been measured through an FMCW radar and an ECG; moreover, a video camera has also been used to inspect the chest dynamics of the patient under test. A dataset composed by the measurements acquired from six different people has been used for validating the adopted signal processing methods. Two different methods have been tested: one based on the FFT (similar to the one described by the block diagram shown in Fig. 9) and the other one based on the computation of the autocorrelation of the phase vector $\hat{\psi}$ (48). The obtained results have evidenced that: 1) both BR and HR can be accurately extracted from radar measurements and 2) the estimation of HR in the presence of the respiration harmonics can be challenging. Methods similar to the ones employed in [117] have been successfully exploited in [108] and [118], for identifying the vital parameters of ten subjects that experience different sleep scenarios and for simultaneously estimating the vital signs of multiple people, respectively. In [116], a system for measuring blood pressure is described; results on human subjects reveal that radar-based arterial pulse detection is very promising for future applications in blood pressure detection and monitoring.

3) SFCW Radars: An FFT-based estimation method, similar to the one described in Section V-A, has been employed in [119] and [120] to estimate the BR and HR of multiple subjects in a room; these subjects have been sitting on a chair or lying down in a bed and have been characterized by different orientations. In [120], radar-based estimates have been compared with the HR and BR estimates provided by a contact reference sensor. The employed radar system has been shown to achieve the best performance when the chest of the subject under test is in front of it; however, even if this condition is not met, radar-based estimates are still sufficiently accurate. In [119], the performance of radar-based monitoring in scenarios in which obstacles, characterized by different shapes and materials (like walls), are placed between the radar and the subject under test is evaluated. Finally, an SFCW radar system has been employed in [121] and [122] to simultaneously

[30] In this table, the population size is low, medium, or high if $1 < N_p \leq 10$, $10 < N_p \leq 20$, or $N_p > 20$, respectively.

Table 6 Classification of the References Cited in Sections VII-A and VII-B Based on: 1) the Size of the Acquired Dataset (L, M, and H Correspond to $1 < N_p \leq 10$, $10 < N_p \leq 20$, and $N_p > 20$, Respectively, Where N_p Denotes the Overall Number of Acquisitions); 2) the Position of the Subject/Subjects Under Test; 3) the Employed Radar Technology; and 4) the Category of the Adopted Signal Processing Method

Ref. no.	Dataset size	Position of the monitored subjects			Radar technology				Freq.	Signal proc.	
		sitting	lying down	other	CW	FMCW	SFCW	UWB	GHz	MB	LB
[109]	H	✓			✓				2.4	✓	
[111]	H	✓			✓				5.8	✓	
[3]	L			✓	✓				2.4	✓	
[110]	M		✓		✓				2.4		✓
[88]	M	✓			✓				24		✓
[112]	M		✓		✓				24	✓	
[27]	L		✓		✓				24	✓	
[15]	L			✓	✓				2.4	✓	
[113]	L			✓	✓				2.4	✓	
[114]	L	✓			✓				5.8,120	✓	
[116]	M			✓		✓			60	✓	
[117]	L		✓			✓			24	✓	
[118]	L	✓	✓			✓			122	✓	
[67]	L		✓			✓			77	✓	
[29]	L	✓				✓			5.8	✓	
[108]	M	✓				✓			24	✓	
[115]	L			✓		✓			10	✓	
[119]	M		✓				✓		0.3-1.3	✓	
[120]	M	✓					✓		2.4	✓	
[121]	L						✓		9.0	✓	
[122]	L						✓		5.8	✓	
[38]	L	✓				✓		✓	77	✓	
[74], [123]	L	✓						✓	6.8	✓	
[124]	L	✓		✓				✓	4.3	✓	
[125]	H		✓					✓	94	✓	
[28]	H	✓						✓	7.25		✓
[91]	H	✓						✓	79		✓

estimate the vital signs of multiple people. It is also worth mentioning that the estimation method devised in [122] consists in applying a CWT to the phase vector $\hat{\psi}$ (48) in order to separate the breath contribution from the one due to heart.

4) IR-UWB Radars: An estimator based on autocorrelation of the phase vector $\hat{\psi}$ (48) and an FFT-based estimator (similar to the one described by the block diagram of Fig. 9) have been employed in [124] and [125], respectively, where the raw data acquired through an IR-UWB radar system have been processed to extract the vital signs of different subjects. The accuracy achieved by an IR-UWB radar system in vital sign estimation has been compared with that of an FMCW radar system in [38]; the latter system is shown to outperform the former one due to its ability to perform clutter suppression. Note that, as shown in [123], noise and clutter affecting the measurement acquired through an IR-UWB radar can be mitigated by means of Kalman filtering.

B. Radar Setups in Real-World Scenarios

Radar systems can be potentially exploited for remote monitoring of vital signs as conveniently and as easily as wearable devices in heterogeneous scenarios. Readers should not forget, however, that essential requirements for their adoption in real-world applications are represented by their ease of use and accuracy. Various results about the accuracy of radar systems for vital sign monitoring in real-world (and often challenging) scenarios can be found in [6], [27], [29], [67], [108], [115], and [126]; note that works [6], [29], [67], and [108] concern FMCW radar systems, whereas works [27], [115], and [126] concern CW Doppler and IR-UWB radars. More specifically, pioneering experiments regarding tracking of human vital signs in real scenarios using FMCW radar systems have

been described in [6], while the use of radar systems in a hospital for measuring the vital signs of patients has been investigated in [29], [67], and [27], whereas more challenging scenarios have been considered in [115], [126], and [108]. The use of an IR-UWB radar for through-the-wall BR and HR estimation has been proposed for a single subject and multiple subjects in [127] and [128], respectively. A brief description of the experimental setup adopted in the measurement campaigns conducted by the authors of the articles cited above and of the main results extracted from their experimental data is provided below.

1) The use of an MIMO FMCW radar in an hospital bedroom has been investigated in [67]. The radar device has been positioned on the ceiling of a room, in front of the bed on which a static subject was lying down; moreover, the monitored subject was facing up the radar during the data acquisition process, which lasted 40 min. A good correlation between the BR and HR acquired through a reference sensor and their estimates provided by the radar system has been found. Note that the scenario considered in this case is that of a typical hospital room in which vital signs monitoring concerns patients at rest; for this reason, this task is accomplished in the absence of random movements of their chests.
2) An FMCW radar endowed with a custom array of antennas has been employed to estimate the vital signs of a person sitting on a chair in [29]. The analyzed measurements have been acquired on five subjects (three males and two females), not suffering from any cardiac or respiratory pathology, whose age ranged from 25 to 63 years. These subjects have been positioned in front of the radar with different orientations (their chest, their left, their back, and right side facing the radar antenna). The employed system has been able to accurately detect BR and HR, regardless of chests patient orientation toward the radar antenna.
3) A custom-designed CW radar system placed under a bed mattress has been employed in [27] to continuously measure the vital parameters of various patients without restricting their movements. The developed system has been able to detect the activity of each patient (i.e., entering the bed, getting out of it, or moving inside it) and to continuously measure his/her vital signs in different positions.
4) An FMCW radar has been employed for the estimation of the vital signs of a person experiencing different sleep conditions in [108]. In this case, the radar device has been positioned on the ceiling of a room in front of the bed on which a static patient was lying down in different positions or was performing simple activities; this allowed to emulate real-life sleep conditions. The measurements have been acquired on 11 patients (whose age ranged from 25 to 55 years); a good correlation has been found between the radar-based estimates of vital signs and those provided by a reference device. These results, together with those illustrated in [27], have evidenced that radar-based systems can be very useful in various healthcare applications (e.g., in the study of sleep apnea, in the monitoring of bedridden patients, and, more in general, in the monitoring of hospitalized patients).
5) The use of a dual-frequency[31] CW microwave radar for vital sign estimation inside an ambulance has been studied in [115]. The measurements have been acquired on eight healthy male subjects whose age ranged from 21 to 24 years. Each of the subjects was lying down on a stretcher contained inside an isolator; therefore, his respiratory and cardiac activities were monitored from outside the isolator. The employed radar system has been able to measure the HR and BR of the monitored subject with good accuracy, in both static and dynamic conditions of the ambulance. Note that the innovative method proposed for vital sign detection could be very useful in other scenarios (e.g., in the monitoring of infectious patients).
6) Various results about the use of an IR-UWB radar system for monitoring the BR of six neonates[32] in a neonatal intensive care unit have been illustrated in [126]. In all the experiments, the employed radar system has been covered with a white plastic cap and has been hung at the end of a specially designed arm placed on the top of a tripod; moreover, it has been placed at a distance of 35 cm from the chest of each subject. Each of the neonates has been placed in a supine position inside an open-air crib, and his/her torso has been covered with a blanket. A high accuracy has been achieved, despite the small movements of the babies under test.
7) Some results about the use of IR-UWB radar systems in vital sign monitoring have been illustrated in [127] and [128]. In particular, in [127], an IR-UWB monostatic radar system operating at 4.3 GHz and having a bandwidth (resolution) of 2.3 GHz (6.5 cm) has been employed for vital signs estimation of a single subject located behind: a gypsum wall, a wooden door, a brick wall; and a load bearing concrete wall. Three different methods have been proposed for extracting vital signs from radar measurements, namely, a DFT-based method for BR estimation, a clutter reduction technique based on the singular value decomposition (SVD), and an STFT for analyzing the temporal evolution of the spectral components of the received signal. The numerical results provided in this article cited above confirm that the proposed methods are achieved similar performance in the considered scenario. In [128], instead, an MIMO IR-UWB radar,

[31] The considered radar system operated at both 10 and 24 GHz.

[32] In this case, the subjects under test were two males and four females with a median gestational age of 38 weeks and a median birth weight of 3100 g.

equipped with an array of 10 × 10 physical elements and operating at a center frequency of 2 GHz, is employed to detect the vital signs of three male adults (having different heights and weights), sitting in front of the radar system at a distance that does not exceed 2.5 m; both line-of-sight conditions and the presence of a wall hiding them are considered. A simple FFT processing has been considered. The obtained numerical results evidence that an MIMO IR-UWB radar can achieve through-the-wall detection of multiple subjects and estimate their BR and HR, provided that their body movements are quite small.

C. Heart Sounds Monitoring

Currently, the standard reference tool for continuous cardiac monitoring is electrocardiography; it requires touch-based wiring of patient skin. In clinical practice, a series of pathological processes would certainly benefit from contactless monitoring; these conditions may include patients with an infection or a sepsis (e.g., infected by SARS CoV-2) or patients with mental disorders that do not allow conventional monitoring according to cardiology settings. In cardiac intensive units or in intermediate care units, continuous monitoring of heartbeat is a common practice because detection and prevention of critical states of health can lead to timely therapeutic interventions, with the result of a better outcome. In fact, several cardiac conditions could be immediately harmful and potentially fatal (e.g., cardiac arrhythmias, heart attacks, acute heart failure, and stroke), thus requiring prompt detection of cardiac or respiratory anomalies. Recently, in the field of radar-based systems for vital signs monitoring, an effort has been made to take a step forward and, in particular, to detect heart sounds [101], [102], [129]. The classification of normal or abnormal heart sounds has been investigated in [129]. In that article, it has been shown that the heart signal recorded by a custom-designed CW radar system is highly correlated with the signal registered by a phonocardiograph, used as a reference. Based on this correlation, each period of the recorded radar signal can be divided into the different temporal phases of the cardiac activity, namely, into systole and diastole (see Section III-A); this procedure is called heart sound segmentation. After recognizing systole and diastole in the received radar signal, a reliable detection of normal or abnormal heart sounds can be accomplished using an LSTM network for heart sound segmentation; this has been shown in [101], where an heterogeneous dataset of recorded heart sounds and vital signs acquired through a CW Doppler radar has been used [102]. The measurements of this dataset originate from multiple subjects in different positions of their bodies and in various conditions, such as during breath-holding, during speaking, and after postexercise. The obtained results have evidenced that more than 90% of the recordings were of high quality and that the correlation between radar and ECG signals was almost perfect. As far as the impact of body position is concerned, it has been found that, in general, heart sounds can be detected in almost all the considered positions; however, the measurability at a certain position changes from subject to subject. This is partly due to the fact body anatomy, and in particular, heart position inside chest may exhibit some variations from person to person.

Further analysis should be performed to achieve solid results, as these represent only preliminary data about the innovative radar-based detection of heart sounds. This technology could lead to a new way of noninvasive cardiac monitoring and could be revolutionary in the cardiology settings. Currently, during medical visits, cardiologists use a stethoscope for heart evaluation; this tool allows them to check for sounds, which may indicate pathological changes in the heart or the heart valves. However, the validity of the assessment strongly depends on the experience of the physician. An objective, operator-independent and automated analysis of heart sounds accomplished through radar technology would be very useful; note also that, in this case, the availability of large datasets for big data analysis would be very useful.

VIII. CURRENT TRENDS

In this section, the most relevant trends in the ongoing research activities on radar systems for vital signs monitoring are described. In particular, we focus on research activities related to: 1) the techniques for the compensation of RBMs; 2) the impact of body orientation on the detection of vital signs and the quality of their estimates; 3) the detection of HRV; and 4) the exploitation of radar-based monitoring for user identity authentication.

A. Compensation of RBMs and Impact of Body Orientation

The RBMs of any person affect the estimate of his/her vital signs provided by radar devices. These movements, in fact, modulate the radar waveform both in its amplitude and frequency, thus distorting the received echoes. This may significantly affect the quality of the estimates of vital signs generated by radar systems. Consequently, RBMs may represent an important obstacle to the adoption of radar technology in certain scenarios. It is also worth mentioning that, if an mm-wave radar device is employed, the eye blinking of the monitored subject may be detected as a large RBM, resulting in a significant degradation in the quality of the received signal phase; the impact of this disturbance can be substantially mitigated through the use of MIMO radars since these are able to steer their beam toward his/her chest [22].

Recently, two approaches to motion compensation have been proposed. The first approach is a hardware RBM compensation acting at the RF front-end level and, consequently, limiting the risks of saturating radar transceivers in the presence of strong echoes [21]. The second one, instead, consists in accomplishing a digital compensation

after demodulation; this can be implemented more easily and lends itself to a more precise control. For this reason, in the remaining part of this subsection, we focus on the last approach only.

One of the easiest strategies to extract the (weak) vital sign components from the radar measurements and remove the distortion due to RBMs is represented by digital filtering. However, this solution is optimal only when the statistical characteristics of the filter input match prior information on which the design of the filter is based; unluckily, such characteristics are normally unknown. For this reason, a more robust solution has been proposed in [130], where an ANC recursive algorithm is employed, in combination with polynomial fitting, in a CW Doppler radar system. It is important to point out that: 1) polynomial fitting is used to reconstruct the signal components due to RBMs and that must be subtracted from the overall signal provided by the radar receiver and 2) this strategy allows to achieve RBM compensation when a single radar system is used and does not require additional sensors. The use of a multiradar system for canceling RBMs has been proposed in [73]. In this case, two CW Doppler radar systems have been put on opposite sides with respect to the body of the monitored subject; when his/her body was leaning toward one of the radars, it moved away from the other one [73] so that the distance between each radar and the body changed in an opposite manner. Based on this consideration, it has been shown that RBMs can be canceled by combining the measurements provided by the two radars. The main drawbacks of a multiradar approach consist in an increase of system complexity, cost, and power consumption and in the need of a larger room for the experimental setup. A different approach to RBM compensation relies on the use of a hybrid system, including radar and camera [131]. In this case, the information provided by the camera has been used to compensate for the phase distortion due to body movements. Unluckily, this approach has been shown to work well when body movements are regular and deterministic.

As its can be easily inferred from our previous analysis, RBM compensation should be considered as an open research problem since a few solutions are available in the technical literature.

Another open research problem mainly concerns the impact of body orientation on the detectability of HR and BR, and on the quality of their estimates. The breathing movement and the heart dynamics can be detected not only if the radar is positioned in front of the chest of the monitored subject but also when his/her body has a different orientation with respect to the other radar itself, even if some degradation is experienced in the estimation of vital signs [29]. Some interesting methods for correctly estimating BR and HR in the presence of different body orientations have been proposed in [28] and [132]. In particular, the use of an ANN for fusing measurements coming from three different radar sensors, distributed as endpoints of an equilateral triangle, and for compensating the effect of body orientation is investigated in [28]. The obtained results show that the network is able to achieve a 95% score in the classification of six different body orientations and to compensate for them; moreover, an accurate estimate of HR is obtained for every body orientation. The method developed in [132] is also based on the exploitation of a neural network for the compensation of body orientation in the estimation of BR and HR; however, the employed mm-wave radar, mounted on a robot system, allows to acquire four different sitting poses and 180 min of data.

B. HR Variability

The HR estimated by means of a radar system represents a measure of the overall number of heartbeats observed over a given time interval (e.g., over 1 min). However, we should not forget that, within a certain observation interval, the temporal distance between two adjacent heartbeats may not remain constant. This phenomenon, known as HRV, is related to heart–brain interactions and is regulated by the autonomic nervous system [133], [134]. More specifically, HRV reflects beat-to-beat changes in peak RR intervals,[33] which depend on the interrelation between sympathetic and vagal tones. In fact, the sinus node, the principal heart's pacemaker, has its own intrinsic activity; however, several external and internal stimuli altering the autonomic balance influence the final HR [135].

HR changes may originate from a variety of conditions such as mental or physical stress, cardiac or noncardiac diseases, or pharmacological or invasive treatments; the respiration-related fluctuation of HR, known as respiratory sinus arrhythmia, is probably the most commonly investigated component of HRV.

The autonomic nervous system imbalance with increased sympathetic and decreased the vagal tone has been proven to be associated with higher risk of cardiac mortality. Therefore, HRV has become an important and recognized tool in identifying patients at risk of cardiovascular death [136] and can be considered as an indicator for both physiological conditions and pathological processes, such as depression, diabetic neuropathy, and heart failure. Moreover, it can be exploited to monitor postsurgery and postinfarction patients in order to assess the risk of ventricular tachyarrhythmias leading to sudden cardiac death.

Nowadays, different methods can be employed to measure HRV; these include a series of simple bedside reflex tests and more advanced computer-based algorithms for detecting spontaneous peak RR interval changes. The accomplished analysis is usually based on long-term (usually 24 h) Holter ECG recordings or short-term (usually few minutes) ECG recordings and aims at avoiding any influence from external stimuli that could affect autonomic

[33]The RR interval represents the time elapsed between two successive R-waves of the QRS signal on the ECG. It is a function of intrinsic properties of the sinus node as well as autonomic influences.

nervous tone [137]. In general, an accurate analysis of HRV may require a long observation interval in a clinical environment or in home-care scenarios. The assessment of this phenomenon is based on the evaluation of various time- and frequency-domain features (see [108, Table 2, Paragraph 2.6]). Time-domain features aim at quantifying the variability in interbeat intervals (also called NN peak intervals)[34] and include the SDNN peak intervals

$$\mathrm{SDNN} \triangleq \sqrt{\frac{\sum_{i=1}^{\bar{N}} \left(\Delta t^{(i)} - \Delta\bar{t}\right)^2}{\bar{N}}} \tag{95}$$

and the RMSSD

$$\mathrm{RMSSD} \triangleq \sqrt{\frac{\sum_{i=2}^{\bar{N}} \left(\Delta t^{(i)} - \Delta t^{(i-1)}\right)^2}{\bar{N}-1}} \tag{96}$$

where $\bar{N}$ is the total number of beats detected in the heart signal, $\Delta t^{(i)}$ is the duration of the time interval between the $(i+1)$th detected beat and the previous beat, and

$$\Delta\bar{t} \triangleq \frac{\sum_{i=1}^{\bar{N}} \Delta t^{(i)}}{\bar{N}} \tag{97}$$

is the average duration of the interval between two consecutive beats. If an estimate of the probability density function [in the form of a probability mass function (pmf)] of the NN peak intervals is available, a further meaningful feature is represented by the TRI, which is defined as

$$\mathrm{TRI} = \frac{\bar{N}}{\mathcal{P}_{\mathrm{NN,max}}} \tag{98}$$

where $\mathcal{P}_{\mathrm{NN,max}}$ is the maximum of the abovementioned pmf [133].

Frequency-domain features are usually evaluated through FFT processing, and refer to the low-frequency band or the high-frequency band. The former band accounts for modulations whose period ranges from 7 to 25 s, whereas the latter one refers to shorter periods. The presence of a significant component in the HF band is typically a symptom of stress or anxiety.

Radar-based estimation of HRV may represent an appealing and challenging alternative to ECG for monitoring the physical and mental status of patients. However, as far as we know, this topic is addressed by a few articles in the technical literature [3], [15], [108], [118], [138], [139]. More specifically, various results about the use of CW Doppler radars for analyzing HRV and drowsiness can be found in [138], [15], and [3] and. The other articles, instead, involve FMCW radars. In particular, an FMCW radar operating in the K-band has been employed in [108] to monitor HRV in 11 patients of different ages during their sleep. The obtained results evidence that the time and frequency features extracted from the radar signal are correlated with those evaluated based on the measurements acquired from a reference sensor. The effect of the coupling between breathing and heartbeat signals on HRV has been investigated in [118]; in this case, an FMCW radar operating at 122 GHz has been used. Finally, a completely novel approach based on DL (and, in particular, on LSTM neural networks) has been proposed in [139] to accurately estimate HRV, by analyzing the data collected by a custom-designed, six-port, CW Doppler radar operating at 24 GHz.

[34] In the case of a CW radar system, an NN interval can be defined as the temporal distance between two consecutive maxima of the phase vector $\hat{\psi}$ available at the output of the bandpass filter appearing in the block diagram of Fig. 9.

C. Vital Sign-Based Authentication

The capability of radars to accurately estimate the vital signs of a person is attractive not only for monitoring the health status of a patient and detect possible diseases but also for user identity authentication. Nowadays, many people are used to log-in in their own smartphones by simply looking at their camera or due to their fingerprint. These approaches can be classified as what you are methods since they make use of personal traits (biometrics) that are hard to reproduce or mimic. Within this category, facial recognition represents a less robust user authentication method with respect to other physiological biometrics, such as fingerprints or iris scans [140], [141]. Authentication methods exploiting radar-based identification of vital signs, instead, are gaining attention because, unlike other physiological biometric-based approaches (e.g., ECG), they do not require direct contact between the human body and the sensor. Moreover, an identity authentication system based on the recognition of breath or heart traits may be sufficiently robust and reliable, since, as evidenced by various studies, the respiratory personality is unique and is preserved over long periods in adult humans at rest [142], [143]. This can be related to the fact that the physiological structure (e.g., the strength of the diaphragm and intercostal muscles and volume of the thoracic cavity) and the respiratory motions associated with chest movements have specific characteristics for each person.

The use of a CW Doppler radar device for heart- and breathing-based user authentication has been investigated in [140] and [144] and in [145], [146], and [147], respectively. All the proposed methods make use of ML classification algorithms fed by a set of features extracted from the phase vector $\hat{\psi}$ (48). More specifically, in [145], three different sets of features that have been used. The most relevant features of the first set are the BR $\hat{b}_r$ (see Section V-A), the breathing depth, the average speed of exhale, and the average speed of inhale. The other two sets of features, instead, aim at monitoring the ratio of inhale and exhale breathing areas, and the breathing mechanism right after and before the apex (full lung volume). Moreover, it has been shown that a K-NN algorithm, trained over a dataset consisting of measurements lasting 60 s and acquired over

six different subjects, is able to recognize the breathing pattern of different people with a good classification score. Better classification results can be obtained by means of an SVM classifier, as shown in [146] and [147].

Despite these positive results, respiratory-based identity authentication is far from being mature and requires extensive analysis and investigation. In fact, people need to be authenticated under various mental or physical states. Therefore, potential variations occurring in the normal breathing pattern of a person must be considered; ignoring them could reduce the identification accuracy, as observed in [147]. For this reason, a heart-based authentication approach has been proposed in [140]. In this case, the heart signal extracted from the phase vector $\hat{\psi}$ (48) has been segmented in different periods, each encompassing a small number of cardiac cycles; within each period, a set of eight features has been manually extracted. The results obtained through an SVM classifier trained on the data acquired over 78 different subjects have confirmed that an authentication method based on radar-based recognition of cardiac motion is really feasible.

IX. CONCLUSION

Nowadays, a significant body of literature is available in the field of radar-based monitoring of vital signs. This article has offered a broad introduction to this field with the aim of explaining some fundamental concepts, technologies, methods, and results to a wide audience. We really hope that our overview of the available radar technologies, the employed signal processing methods, and the specific applications being considered in medicine will stimulate the interest in radar-based monitoring of vital signs. We believe that radar technology is now mature enough for being considered in the medical field. However, there is still ample room for the development of accurate and computationally efficient estimation techniques and for their implementation on commercial hardware platforms. Readers should also keep in mind that most of the results available in the technical literature refer to a very limited human population and, usually, to healthy subjects. In fact, studies about the monitoring of real patients in realistic medical scenarios are still scarce. Despite this, it has become clear that radar systems can represent a viable alternative to wearable sensors or the only possible option in some critical scenarios, where contactless monitoring is absolutely required. Furthermore, the technological improvements and the advances in processing techniques achieved in recent years have made it possible to overcome various limitations. Therefore, due to their capability of continuous and contactless detection, radars may revolutionize patient monitoring in hospitals and in other healthcare facilities in the near future. ■

Acknowledgment

The authors would like to thank the anonymous reviewers for their comments that really helped them to improve the overall quality of the manuscript.

REFERENCES

[1] J. Ludikhuize, S. M. Smorenburg, S. E. de Rooij, and F. de Jonge, "Identification of deteriorating patients on general wards; measurement of vital parameters and potential effectiveness of the modified early warning score," *J. Crit. Care*, vol. 27, pp. 4247–42413, Aug. 2012.

[2] D. Dias and J. P. S. Cunha, "Wearable health devices-vital sign monitoring, systems and technologies," *Sensors*, vol. 18, no. 8, p. 2414, 2018.

[3] S. Suzuki, T. Matsui, S. Gotoh, Y. Mori, B. Takase, and M. Ishihara, "Development of non-contact monitoring system of heart rate variability (HRV)—An approach of remote sensing for ubiquitous technology," in *Proc. Int. Conf. Ergonom. Health Aspects Work With Comput.*, 2009, pp. 195–203.

[4] C. Gu, C. Li, J. Lin, J. Long, J. Huangfu, and L. Ran, "Instrument-based noncontact Doppler radar vital sign detection system using heterodyne digital quadrature demodulation architecture," *IEEE Trans. Instrum. Meas.*, vol. 59, no. 6, pp. 1580–1588, Jun. 2010.

[5] S. M. M. Islam, F. Fioranelli, and V. M. Lubecke, "Can radar remote life sensing technology help combat COVID-19?" *Frontiers Commun. Netw.*, vol. 2, p. 3, May 2021.

[6] G. Wang, J.-M. Muñoz-Ferreras, C. Gu, C. Li, and R. Gómez-García, "Application of linear-frequency-modulated continuous-wave (LFMCW) radars for tracking of vital signs," *IEEE Trans. Microw. Theory Techn.*, vol. 62, no. 6, pp. 1387–1399, Jun. 2014.

[7] G. Wang, C. Gu, T. Inoue, and C. Li, "A hybrid FMCW-interferometry radar for indoor precise positioning and versatile life activity monitoring," *IEEE Trans. Microw. Theory Techn.*, vol. 62, no. 11, pp. 2812–2822, Nov. 2014.

[8] J. C. Lin, "Noninvasive microwave measurement of respiration," *Proc. IEEE*, vol. 63, no. 10, p. 1530, Oct. 1975.

[9] J. C. Lin, "Microwave sensing of physiological movement and volume change: A review," *Bioelectromagnetics*, vol. 13, no. 6, pp. 557–565, 1992.

[10] T. E. McEwan, "Ultra-wideband radar motion sensor," U.S. Patent 5 361 070, Nov. 1, 1994.

[11] M. Varanini, P. C. Berardi, F. Conforti, M. Micalizzi, D. Neglia, and A. Macerata, "Cardiac and respiratory monitoring through non-invasive and contactless radar technique," in *Proc. Comput. Cardiol.*, Sep. 2008, pp. 149–152.

[12] E. F. Greneker, "Radar sensing of heartbeat and respiration at a distance with applications of the technology," in *Proc. Radar Syst. (RADAR)*, 1997, pp. 150–154.

[13] E. Staderini, "UWB radar in medicine," *IEEE Aerosp. Electron. Syst. Mag.*, vol. 17, no. 1, pp. 13–18, Feb. 2002.

[14] C. Li, J. Lin, and Y. Xiao, "Robust overnight monitoring of human vital signs by a non-contact respiration and heartbeat detector," in *Proc. 28th Annu. IEEE Int. Eng. Med. Biol. Soc. Conf.*, Mar. 2006, pp. 2235–2238.

[15] J.-Y. Kim, J.-H. Park, S.-Y. Jang, and J.-R. Yang, "Peak detection algorithm for vital sign detection using Doppler radar sensors," *Sensors*, vol. 19, no. 7, p. 1575, Apr. 2019.

[16] D. Zito et al., "SoC CMOS UWB pulse radar sensor for contactless respiratory rate monitoring," *IEEE Trans. Biomed. Circuits Syst.*, vol. 5, no. 6, pp. 503–510, Dec. 2011.

[17] A. Droitcour, V. Lubecke, J. Lin, and O. Boric-Lubecke, "A microwave radio for Doppler radar sensing of vital signs," in *IEEE MTT-S Int. Microw. Symp. Dig.*, vol. 1, May 2001, pp. 175–178.

[18] C. Gu, R. Li, S. B. Jiang, and C. Li, "A multi-radar wireless system for respiratory gating and accurate tumor tracking in lung cancer radiotherapy," in *Proc. Annu. Int. Conf. IEEE Eng. Med. Biol. Soc.*, Aug. 2011, pp. 417–420.

[19] C. Li, V. M. Lubecke, O. Boric-Lubecke, and J. Lin, "A review on recent advances in Doppler radar sensors for noncontact healthcare monitoring," *IEEE Trans. Microw. Theory Techn.*, vol. 61, no. 5, pp. 2046–2060, May 2013.

[20] C. Gu, "Short-range noncontact sensors for healthcare and other emerging applications: A review," *Sensors*, vol. 16, no. 8, p. 1169, Aug. 2016.

[21] M. Kebe, R. Gadhafi, B. Mohammad, M. Sanduleanu, H. Saleh, and M. Al-Qutayri, "Human vital signs detection methods and potential using radars: A review," *Sensors*, vol. 20, no. 5, p. 1454, Mar. 2020.

[22] E. Cardillo and A. Caddemi, "A review on biomedical MIMO radars for vital sign detection and human localization," *Electronics*, vol. 9, no. 9, p. 1497, Sep. 2020.

[23] C. Li et al., "A review on recent progress of portable short-range noncontact microwave radar systems," *IEEE Trans. Microw. Theory Techn.*, vol. 65, no. 5, pp. 1692–1706, May 2017.

[24] S. Pisa, E. Pittella, and E. Piuzzi, "A survey of radar systems for medical applications," *IEEE Aerosp. Electron. Syst. Mag.*, vol. 31, no. 11, pp. 64–81, Nov. 2016.

[25] A. D. Droitcour, O. Boric-Lubecke, V. M. Lubecke, J. Lin, and G. T. A. Kovacs, "Range correlation and I/Q performance benefits in single-chip silicon Doppler radars for noncontact cardiopulmonary monitoring," *IEEE Trans. Microw. Theory Techn.*, vol. 52, no. 3, pp. 838–848, Mar. 2004.

[26] S. Voinigescu, *High-Frequency Integrated Circuits* (The Cambridge RF and Microwave Engineering Series). Cambridge, U.K.: Cambridge Univ. Press, 2013.

[27] S. Schellenberger, K. Shi, F. Michler, F. Lurz, R. Weigel, and A. Koelpin, "Continuous in-bed monitoring of vital signs using a multi radar setup for freely moving patients," *Sensors*, vol. 20, no. 20, p. 5827, Oct. 2020.

[28] X. Yang, Y. Yu, H. Qian, X. Zhang, and L. Zhang, "Body orientation and vital sign measurement with IR-UWB radar network," in *Proc. 42nd Annu. Int. Conf. IEEE Eng. Med. Biol. Soc. (EMBC)*, Jul. 2020, pp. 485–488.

[29] G. Sacco, E. Piuzzi, E. Pittella, and S. Pisa, "An FMCW radar for localization and vital signs measurement for different chest orientations," *Sensors*, vol. 20, no. 12, p. 3489, Jun. 2020.

[30] R. O. Bonow, D. L. Mann, D. P. Zipes, and P. Libby, *Braunwald's Heart Disease E-Book: A Textbook of Cardiovascular Medicine*. Amsterdam, The Netherlands: Elsevier, 2007.

[31] J. Hall, *Guyton and Hall Textbook of Medical Physiology*, 13th ed. Philadelphia, PA, USA: Elsevier, 2016.

[32] M. G. Levitzky, "Pulmonary physiology," in *Pulmonary Physiology*, 7th ed. New York, NY, USA: McGraw-Hill, 2007.

[33] S. McGee, "Evidence-based physical diagnosis," in *Evidence-Based Physical Diagnosis*, 4th ed., S. McGee, Ed. Amsterdam, The Netherlands: Elsevier, 2021, p. 4.

[34] M. Nosrati and N. Tavassolian, "Accurate Doppler radar-based cardiopulmonary sensing using chest-wall acceleration," *IEEE J. Electromagn., RF Microw. Med. Biol.*, vol. 3, no. 1, pp. 41–47, Mar. 2019.

[35] D. Groote et al., "Chest wall motion during tidal breathing," *J. Appl. Physiol.*, vol. 83, no. 5, pp. 1531–1537, 1985.

[36] G. Shafiq and K. C. Veluvolu, "Surface chest motion decomposition for cardiovascular monitoring," *Sci. Rep.*, vol. 4, no. 1, p. 5093, May 2014.

[37] A. Albanese, L. Cheng, M. Ursino, and N. W. Chbat, "An integrated mathematical model of the human cardiopulmonary system: Model development," *Amer. J. Physiol.-Heart Circulatory Physiol.*, vol. 310, no. 7, pp. H899–H921, Apr. 2016.

[38] D. Wang, S. Yoo, and S. H. Cho, "Experimental comparison of IR-UWB radar and FMCW radar for vital signs," *Sensors*, vol. 20, no. 22, p. 6695, Nov. 2020.

[39] M. Mercuri, Y.-H. Liu, I. Lorato, T. Torfs, A. Bourdoux, and C. van Hoof, "Frequency-tracking CW Doppler radar solving small-angle approximation and null point issues in non-contact vital signs monitoring," *IEEE Trans. Biomed. Circuits Syst.*, vol. 11, no. 3, pp. 671–680, Jun. 2017.

[40] M. Skolnik, "Role of radar in microwaves," *IEEE Trans. Microw. Theory Techn.*, vol. 50, no. 3, pp. 625–632, Mar. 2002.

[41] S. M. Patole, M. Torlak, D. Wang, and M. Ali, "Automotive radars: A review of signal processing techniques," *IEEE Signal Process. Mag.*, vol. 34, no. 2, pp. 22–35, Mar. 2017.

[42] A. M. Haimovich, R. S. Blum, and L. J. Cimini, "MIMO radar with widely separated antennas," *IEEE Signal Process. Mag.*, vol. 25, no. 1, pp. 116–129, Dec. 2008.

[43] E. Fishler, A. Haimovich, R. Blum, L. Cimini, D. Chizhik, and R. Valenzuela, "Performance of MIMO radar systems: Advantages of angular diversity," in *Proc. 38th Asilomar Conf. Signals, Syst., Comput.*, vol. 1, Nov. 2004, pp. 305–309.

[44] M. A. Richards, *Fundamentals of Radar Signal Processing*. New York, NY, USA: McGraw-Hill, 2005.

[45] J. Li and P. Stoica, "MIMO radar with colocated antennas," *IEEE Signal Process. Mag.*, vol. 24, no. 5, pp. 106–114, Sep. 2007.

[46] C. Pfeffer, R. Feger, C. Wagner, and A. Stelzer, "FMCW MIMO radar system for frequency-division multiple TX-beamforming," *IEEE Trans. Microw. Theory Techn.*, vol. 61, no. 12, pp. 4262–4274, Dec. 2013.

[47] F.-K. Wang, P.-H. Juan, D.-M. Chian, and C.-K. Wen, "Multiple range and vital sign detection based on single-conversion self-injection-locked hybrid mode radar with a novel frequency estimation algorithm," *IEEE Trans. Microw. Theory Techn.*, vol. 68, no. 5, pp. 1908–1920, May 2020.

[48] T. Wu, T. S. Rappaport, and C. M. Collins, "The human body and millimeter-wave wireless communication systems: Interactions and implications," in *Proc. IEEE Int. Conf. Commun. (ICC)*, Jun. 2015, pp. 2423–2429.

[49] F.-K. Wang et al., "Review of self-injection-locked radar systems for noncontact detection of vital signs," *IEEE J. Electromagn., RF Microw. Med. Biol.*, vol. 4, no. 4, pp. 294–307, Dec. 2020.

[50] C.-H. Tseng, T.-J. Tseng, and C.-Z. Wu, "Cuffless blood pressure measurement using a microwave near-field self-injection-locked wrist pulse sensor," *IEEE Trans. Microw. Theory Techn.*, vol. 68, no. 11, pp. 4865–4874, Nov. 2020.

[51] A. Mishra, W. McDonnell, J. Wang, D. Rodriguez, and C. Li, "Intermodulation-based nonlinear smart health sensing of human vital signs and location," *IEEE Access*, vol. 7, pp. 158284–158295, 2019.

[52] Y. Yuan, A. Y.-K. Chen, and C.-T.-M. Wu, "Super-regenerative oscillator-based high-sensitivity radar architecture for motion sensing and vital sign detection," *IEEE Trans. Microw. Theory Techn.*, vol. 69, no. 3, pp. 1974–1984, Mar. 2021.

[53] Y. Yuan and C.-T.-M. Wu, "Non-contact fingertip microwave plethysmography based on near-field sensing with super-regenerative oscillator," in *IEEE MTT-S Int. Microw. Symp. Dig.*, Jun. 2021, pp. 362–365.

[54] B. Park, O. Boric-Lubecke, and V. M. Lubecke, "Arctangent demodulation with DC offset compensation in quadrature Doppler radar receiver systems," *IEEE Trans. Microw. Theory Techn.*, vol. 55, no. 5, pp. 1073–1079, Jun. 2007.

[55] A. Davoli, G. Guerzoni, and G. M. Vitetta, "Machine learning and deep learning techniques for colocated MIMO radars: A tutorial overview," *IEEE Access*, vol. 9, pp. 33704–33755, 2021.

[56] P. Bello, "Time-frequency duality," *IEEE Trans. Inf. Theory*, vol. IT-10, no. 1, pp. 18–33, Jan. 1964.

[57] P. Di Viesti, A. Davoli, G. Guerzoni, and G. M. Vitetta, "Novel deterministic detection and estimation algorithms for colocated multiple-input multiple-output radars," *IEEE Access*, vol. 10, pp. 2216–2255, 2022.

[58] K. Naishadham, J. E. Piou, L. Ren, and A. E. Fathy, "Estimation of cardiopulmonary parameters from ultra wideband radar measurements using the state space method," *IEEE Trans. Biomed. Circuits Syst.*, vol. 10, no. 6, pp. 1037–1046, Dec. 2016.

[59] E. Sirignano, A. Davoli, G. M. Vitetta, and F. Viappiani, "A comparative analysis of deterministic detection and estimation techniques for MIMO SFCW radars," *IEEE Access*, vol. 7, pp. 129848–129861, 2019.

[60] M. Harter, T. Mahler, T. Schipper, A. Ziroff, and T. Zwick, "2-D antenna array geometries for MIMO radar imaging by digital beamforming," in *Proc. Eur. Radar Conf.*, Oct. 2013, pp. 383–386.

[61] J. Selva, "ML estimation and detection of multiple frequencies through periodogram estimate refinement," *IEEE Signal Process. Lett.*, vol. 24, no. 3, pp. 249–253, Mar. 2017.

[62] A. Ahmad, J. C. Roh, D. Wang, and A. Dubey, "Vital signs monitoring of multiple people using a FMCW millimeter-wave sensor," in *Proc. IEEE Radar Conf.*, Oklahoma City, OK, USA, Apr. 2018, pp. 1450–1455.

[63] G. Vinci et al., "Six-port radar sensor for remote respiration rate and heartbeat vital-sign monitoring," *IEEE Trans. Microw. Theory Techn.*, vol. 61, no. 5, pp. 2093–2100, May 2013.

[64] F.-K. Wang et al., "An injection-locked detector for concurrent spectrum and vital sign sensing," in *IEEE MTT-S Int. Microw. Symp. Dig.*, Anaheim, CA, USA, May 2010, pp. 768–771.

[65] Y. Xiao, J. Lin, O. Boric-Lubecke, and M. Lubecke, "Frequency-tuning technique for remote detection of heartbeat and respiration using low-power double-sideband transmission in the Ka-band," *IEEE Trans. Microw. Theory Techn.*, vol. 54, no. 5, pp. 2023–2032, May 2006.

[66] J.-M. Munoz-Ferreras, Z. Peng, R. Gomez-Garcia, G. Wang, C. Gu, and C. Li, "Isolate the clutter: Pure and hybrid linear-frequency-modulated continuous-wave (LFMCW) radars for indoor applications," *IEEE Microw. Mag.*, vol. 16, no. 4, pp. 40–54, May 2015.

[67] M. Alizadeh, G. Shaker, J. C. M. D. Almeida, P. P. Morita, and S. Safavi-Naeini, "Remote monitoring of human vital signs using mm-Wave FMCW radar," *IEEE Access*, vol. 7, pp. 54958–54968, 2019.

[68] C. Gu et al., "Accurate respiration measurement using DC-coupled continuous-wave radar sensor for motion-adaptive cancer radiotherapy," *IEEE Trans. Biomed. Eng.*, vol. 59, no. 11, pp. 3117–3123, Nov. 2012.

[69] I.-S. Lee, J.-H. Park, and J.-R. Yang, "Detrending technique for denoising in CW radar," *Sensors*, vol. 21, no. 19, p. 6376, Sep. 2021.

[70] H. Noguchi, H. Kubo, T. Mori, T. Sato, and H. Sanada, "Signal phase estimation for measurement of respiration waveform using a microwave Doppler sensor," in *Proc. 35th Annu. Int. Conf. IEEE Eng. Med. Biol. Soc. (EMBC)*, Jul. 2013, pp. 6740–6743.

[71] J. Wang, X. Wang, L. Chen, J. Huangfu, C. Li, and L. Ran, "Noncontact distance and amplitude-independent vibration measurement based on an extended DACM algorithm," *IEEE Trans. Instrum. Meas.*, vol. 63, no. 1, pp. 145–153, Jan. 2014.

[72] W. Xu, Y. Li, C. Gu, and J.-F. Mao, "Large displacement motion interferometry with modified differentiate and cross-multiply technique," *IEEE Trans. Microw. Theory Techn.*, vol. 69, no. 11, pp. 4879–4890, Nov. 2021.

[73] C. Li and J. Lin, "Random body movement cancellation in Doppler radar vital sign detection," *IEEE Trans. Microw. Theory Techn.*, vol. 56, no. 12, pp. 3143–3152, Dec. 2008.

[74] X. Hu and T. Jin, "Short-range vital signs sensing based on EEMD and CWT using IR-UWB radar," *Sensors*, vol. 16, no. 12, p. 2025, 2016.

[75] Y. Xu, S. Dai, S. Wu, J. Chen, and G. Fang, "Vital sign detection method based on multiple higher order Cumulant for ultrawideband radar," *IEEE Trans. Geosci. Remote Sens.*, vol. 50, no. 4, pp. 1254–1265, Apr. 2012.

[76] T. K. V. Dai et al., "Enhancement of remote vital sign monitoring detection accuracy using multiple-input multiple-output 77 GHz FMCW radar," *IEEE J. Electromagn., RF Microw. Med. Biol.*, vol. 6, no. 1, pp. 111–122, Mar. 2022.

[77] Y. Wang, Y. Shui, X. Yang, Z. Li, and W. Wang, "Multi-target vital signs detection using frequency-modulated continuous wave radar," *EURASIP J. Adv. Signal Process.*, vol. 2021, no. 1, p. 103, Oct. 2021.

[78] I. Walterscheid, O. Biallawons, and P. Berens, "Contactless respiration and heartbeat monitoring of multiple people using a 2-D imaging radar," in *Proc. 41st Annu. Int. Conf. IEEE Eng. Med. Biol. Soc. (EMBC)*, Jul. 2019, pp. 3720–3725.

[79] S. Wang, S. Kueppers, H. Cetinkaya, and R. Herschel, "3D localization and vital sign detection of human subjects with a 120 GHz MIMO radar," in *Proc. 20th Int. Radar Symp. (IRS)*, Jun. 2019, pp. 1–6.

[80] F. Liang et al., "Detection of multiple stationary humans using UWB MIMO radar," *Sensors*, vol. 16, no. 11, p. 1922, 2016.

[81] X. Shang, J. Liu, and J. Li, "Multiple object localization and vital sign monitoring using IR-UWB MIMO radar," *IEEE Trans. Aerosp. Electron. Syst.*, vol. 56, no. 6, pp. 4437–4450, Dec. 2020.

[82] M. Nosrati, S. Shahsavari, S. Lee, H. Wang, and N. Tavassolian, "A concurrent dual-beam phased-array Doppler radar using MIMO

beamforming techniques for short-range vital-signs monitoring," *IEEE Trans. Antennas Propag.*, vol. 67, no. 4, pp. 2390–2404, Apr. 2019.
[83] H. Rohling, "Radar CFAR thresholding in clutter and multiple target situations," *IEEE Trans. Aerosp. Electron. Syst.*, vol. AES-19, no. 4, pp. 608–621, Jul. 1983.
[84] O. Simeone, *A Brief Introduction to Machine Learning for Engineers*. Norwell, MA, USA: Now Foundations and Trends, 2018.
[85] C. M. Bishop, *Pattern Recognition and Machine Learning (Information Science and Statistics)*. Berlin, Germany: Springer-Verlag, 2006.
[86] J. Saluja, J. Casanova, and J. Lin, "A supervised machine learning algorithm for heart-rate detection using Doppler motion-sensing radar," *IEEE J. Electromagn., RF Microw. Med. Biol.*, vol. 4, no. 1, pp. 45–51, Mar. 2020.
[87] N. T. P. Van, L. Tang, A. Singh, N. D. Minh, S. C. Mukhopadhyay, and S. F. Hasan, "Self-identification respiratory disorder based on continuous wave radar sensor system," *IEEE Access*, vol. 7, pp. 40019–40026, 2019.
[88] N. Malešević, V. Petrović, M. Belić, C. Antfolk, V. Mihajlović, and M. Janković, "Contactless real-time heartbeat detection via 24 GHz continuous-wave Doppler radar using artificial neural networks," *Sensors*, vol. 20, no. 8, p. 2351, Apr. 2020.
[89] K. Shi et al., "Automatic signal quality index determination of radar-recorded heart sound signals using ensemble classification," *IEEE Trans. Biomed. Eng.*, vol. 67, no. 3, pp. 773–785, Mar. 2020.
[90] C.-Y. Huang, G.-W. Fang, H.-R. Chuang, and C.-L. Yang, "Clutter-resistant vital sign detection using amplitude-based demodulation by EEMD-PCA-Correlation algorithm for FMCW radar systems," in *Proc. 49th Eur. Microw. Conf. (EuMC)*, Oct. 2019, pp. 928–931.
[91] S. Wu et al., "Person-specific heart rate estimation with ultra-wideband radar using convolutional neural networks," *IEEE Access*, vol. 7, pp. 168484–168494, 2019.
[92] A. Bin Obadi, P. J. Soh, O. Aldayel, M. H. Al-Doori, M. Mercuri, and D. Schreurs, "A survey on vital signs detection using radar techniques and processing with FPGA implementation," *IEEE Circuits Syst. Mag.*, vol. 21, no. 1, pp. 41–74, 1st Quart., 2021.
[93] O. Biallawons and J. Klare, "Person localization by detection of breathing with the MIMO radar MIRA-CLE Ka," in *Proc. EUSAR 10th Eur. Conf. Synth. Aperture Radar*, Jun. 2014, pp. 1–4.
[94] S. Gabriel, R. Lau, and C. Gabriel, "The dielectric properties of biological tissues: III. Parametric models for the dielectric spectrum of tissues," *Phys. Med. Biol.*, vol. 41, pp. 2271–2293, Dec. 1996.
[95] M. G. Amin, *Radar for Indoor Monitoring: Detection, Classification, and Assessment*, M. G. Amin, Ed. Boca Raton, FL, USA: CRC Press, 2017.
[96] M. Zhadobov, N. Chahat, R. Sauleau, C. L. Quement, and Y. L. Drean, "Millimeter-wave interactions with the human body: State of knowledge and recent advances," *Int. J. Microw. Wireless Technol.*, vol. 3, no. 2, pp. 237–247, 2011.
[97] L. Ren, S. Nahar, A. E. Fathy, T. Phan, N. Tran, and O. Kilic, "Investigation of vital signs monitoring errors due to subject's orientation, clothing and distance from a SFCW radar," in *Proc. IEEE Int. Symp. Antennas Propag. (APSURSI)*, Jun. 2016, pp. 1171–1172.
[98] *Texas Instrument Inc*. Accessed: Feb. 17, 2023. [Online]. Available: https://www.ti.com/
[99] *Infineon GmbH*. Accessed: Feb. 17, 2023. [Online]. Available: https://www.infineon.com/
[100] Q. Liang et al., "Research on non-contact monitoring system for human physiological signal and body movement," *Biosensors*, vol. 9, no. 2, p. 58, Apr. 2019.
[101] K. Shi et al., "Segmentation of radar-recorded heart sound signals using bidirectional LSTM networks," in *Proc. 41st Annu. Int. Conf. IEEE Eng. Med. Biol. Soc. (EMBC)*, Jul. 2019, pp. 6677–6680.
[102] K. Shi et al., "A dataset of radar-recorded heart sounds and vital signs including synchronised reference sensor signals," *Scientific Data*, vol. 7, no. 1, p. 50, Feb. 2020.
[103] Y. Ding, X. Yu, C. Lei, Y. Sun, X. Xu, and J. Zhang, "A novel real-time human heart rate estimation method for noncontact vital sign radar detection," *IEEE Access*, vol. 8, pp. 88689–88699, 2020.
[104] *Hexoskin Device*. Accessed: Feb. 17, 2023. [Online]. Available: https://www.hexoskin.com/
[105] M. Fajkus, "Alternative fiber optic sensor based on Bragg grating for heart rate monitoring," *Int. J. Biosensors Bioelectronics*, vol. 4, no. 5, pp. 231–233, Oct. 2018.
[106] *Shimmer Sensing*. Accessed: Feb. 17, 2023. [Online]. Available: http://shimmersensing.com/
[107] A. K. Gupta, "Respiration rate measurement based on impedance pneumography," Texas Instrum. Incorp., Dallas, TX, USA, Appl. Rep. SBAA181, Feb. 2011.
[108] E. Turppa, J. M. Kortelainen, O. Antropov, and T. Kiuru, "Vital sign monitoring using FMCW radar in various sleeping scenarios," *Sensors*, vol. 20, no. 22, p. 6505, Nov. 2020.
[109] R. Ichapurapu, S. Jain, M. U. Kakade, D. Y. C. Lie, and R. E. Banister, "A 2.4GHz non-contact biosensor system for continuous vital-signs monitoring on a single PCB," in *Proc. IEEE 8th Int. Conf. (ASIC)*, Oct. 2009, pp. 925–928.
[110] H. Zhao et al., "A noncontact breathing disorder recognition system using 2.4-GHz digital-IF Doppler radar," *IEEE J. Biomed. Health Inform.*, vol. 23, no. 1, pp. 208–217, Jan. 2019.
[111] M. Li and J. Lin, "Wavelet-transform-based data-length-variation technique for fast heart rate detection using 5.8-GHz CW Doppler radar," *IEEE Trans. Microw. Theory Techn.*, vol. 66, no. 1, pp. 568–576, Jan. 2018.
[112] F. Michler et al., "A clinically evaluated interferometric continuous-wave radar system for the contactless measurement of human vital parameters," *Sensors*, vol. 19, no. 11, p. 2492, May 2019.
[113] T.-J. Tseng and C.-H. Tseng, "Noncontact wrist pulse waveform detection using 24-GHz continuous-wave radar sensor for blood pressure estimation," in *IEEE MTT-S Int. Microw. Symp. Dig.*, Los Angles, CA, USA, Jun. 2020, pp. 647–650.
[114] L. Wen, Y. Gao, C. Gu, and J. Mao, "PhysioChair: A dual-frequency radar system for noninvasive and continuous detection of physiological signatures," *IEEE Sensors J.*, vol. 22, no. 8, pp. 8224–8233, Apr. 2022.
[115] S. Suzuki et al., "A non-contact vital sign monitoring system for ambulances using dual-frequency microwave radars," *Med. Biol. Eng. Comput.*, vol. 47, no. 1, pp. 101–105, Jan. 2009.
[116] J. E. Johnson, O. Shay, C. Kim, and C. Liao, "Wearable millimeter-wave device for contactless measurement of arterial pulses," *IEEE Trans. Biomed. Circuits Syst.*, vol. 13, no. 6, pp. 1525–1534, Dec. 2019.
[117] L. Anitori, A. de Jong, and F. Nennie, "FMCW radar for life-sign detection," in *Proc. IEEE Radar Conf.*, May 2009, pp. 1–6.
[118] E. Antolinos, F. García-Rial, C. Hernández, D. Montesano, J. I. Godino-Llorente, and J. Grajal, "Cardiopulmonary activity monitoring using millimeter wave radars," *Remote Sens.*, vol. 12, no. 14, p. 2265, Jul. 2020.
[119] L. Liu and S. Liu, "Remote detection of human vital sign with stepped-frequency continuous wave radar," *IEEE J. Sel. Topics Appl. Earth Observ. Remote Sens.*, vol. 7, no. 3, pp. 775–782, Mar. 2014.
[120] L. Ren, L. Kong, F. Foroughian, H. Wang, P. Theilmann, and A. E. Fathy, "Comparison study of noncontact vital signs detection using a Doppler stepped-frequency continuous-wave radar and camera-based imaging photoplethysmography," *IEEE Trans. Microw. Theory Techn.*, vol. 65, no. 9, pp. 3519–3529, Sep. 2017.
[121] W. C. Su, M. C. Tang, R. El Arif, T. S. Horng, and F.-K. Wang, "Stepped-frequency continuous-wave radar with self-injection-locking technology for monitoring multiple human vital signs," *IEEE Trans. Microw. Theory Techn.*, vol. 67, no. 12, pp. 5396–5405, Dec. 2019.
[122] Z. Zhang, Y. Nian, J. Chen, and M. He, "An experimental study to optimize the stepped-frequency continuous-wave radar parameters for noncontact multi-target vital sign monitoring," in *Proc. IEEE Int. Conf. Comput. Electromagn. (ICCEM)*, Mar. 2019, pp. 1–4.
[123] F. Khan and S. H. Cho, "A detailed algorithm for vital sign monitoring of a stationary/non-stationary human through IR-UWB radar," *Sensors*, vol. 17, no. 2, p. 290, 2017.
[124] H. Shen et al., "Respiration and heartbeat rates measurement based on autocorrelation using IR-UWB radar," *IEEE Trans. Circuits Syst. II, Exp. Briefs*, vol. 65, no. 10, pp. 1470–1474, Oct. 2018.
[125] J.-Y. Park et al., "Preclinical evaluation of a noncontact simultaneous monitoring method for respiration and carotid pulsation using impulse-radio ultra-wideband radar," *Sci. Rep.*, vol. 9, no. 1, p. 11892, Aug. 2019.
[126] J. D. Kim et al., "Non-contact respiration monitoring using impulse radio ultrawideband radar in neonates," *Roy. Soc. Open Sci.*, vol. 6, no. 6, Jun. 2019, Art. no. 190149.
[127] S. Singh, Q. Liang, D. Chen, and L. Sheng, "Sense through wall human detection using UWB radar," *EURASIP J. Wireless Commun. Netw.*, vol. 2011, no. 1, p. 20, Jun. 2011.
[128] Z. Li, T. Jin, Y. Dai, and Y. Song, "Through-wall multi-subject localization and vital signs monitoring using UWB MIMO imaging radar," *Remote Sens.*, vol. 13, no. 15, p. 2905, Jul. 2021.
[129] C. Will et al., "Radar-based heart sound detection," *Sci. Rep.*, vol. 8, no. 1, Jul. 2018, Art. no. 11551.
[130] Z.-K. Yang, H. Shi, S. Zhao, and X.-D. Huang, "Vital sign detection during large-scale and fast body movements based on an adaptive noise cancellation algorithm using a single Doppler radar sensor," *Sensors*, vol. 20, no. 15, p. 4183, Jul. 2020.
[131] C. Gu, G. Wang, Y. Li, T. Inoue, and C. Li, "A hybrid radar-camera sensing system with phase compensation for random body movement cancellation in Doppler vital sign detection," *IEEE Trans. Microw. Theory Techn.*, vol. 61, no. 12, pp. 4678–4688, Dec. 2013.
[132] P. Zhao et al., "Heart rate sensing with a robot mounted mmWave radar," in *Proc. IEEE Int. Conf. Robot. Autom. (ICRA)*, May 2020, pp. 2812–2818.
[133] Task Force of the European Society Organization Electrophysiology, "Heart rate variability," *Circulation*, vol. 93, no. 5, pp. 1043–1065, Mar. 1996.
[134] F. Shaffer and J. P. Ginsberg, "An overview of heart rate variability metrics and norms," *Frontiers Public Health*, vol. 5, p. 258, Sep. 2017.
[135] K. C. Bilchick and R. D. Berger, "Heart rate variability," *J. Cardiovascular Electrophysiol.*, vol. 17, no. 6, pp. 691–694, 2006.
[136] M. K. Lahiri, P. J. Kannankeril, and J. J. Goldberger, "Assessment of autonomic function in cardiovascular disease: Physiological basis and prognostic implications," *J. Amer. College Cardiol.*, vol. 51, no. 18, pp. 1725–1733, 2008.
[137] I. Cygankiewicz and W. Zareba, "Heart rate variability," in *Autonomic Nervous System* (Handbook of Clinical Neurology), R. M. Buijs and D. F. Swaab, Eds. Amsterdam, The Netherlands: Elsevier, 2013, vol. 117, pp. 379–393.
[138] O. Boric-Lubecke, W. Massagram, V. M. Lubecke, A. Host-Madsen, and B. Jokanovic, "Heart rate variability assessment using Doppler radar with linear demodulation," in *Proc. 38th Eur. Microw. Conf.*, Oct. 2008, pp. 420–423.
[139] K. Shi et al., "Contactless analysis of heart rate variability during cold pressor test using radar interferometry and bidirectional LSTM networks," *Sci. Rep.*, vol. 11, no. 1, p. 3025, Feb. 2021.
[140] J. Liu, Y. Chen, Y. Dong, Y. Wang, T. Zhao, and Y.-D. Yao, "Continuous user verification via

respiratory biometrics," in *Proc. IEEE INFOCOM Conf. Comput. Commun.*, Jul. 2020, pp. 1–10.
[141] J. Chauhan, Y. Hu, S. Seneviratne, A. Misra, A. Seneviratne, and Y. Lee, "BreathPrint: Breathing acoustics-based user authentication," in *Proc. 15th Annu. Int. Conf. Mobile Syst., Appl., Services*, Jun. 2017, pp. 278–291.
[142] D. F. Proctor and J. B. Hardy, "Studies of respiratory air flow; significance of the normal pneumotachogram," *Bull Johns Hopkins Hosp.*, vol. 85, no. 4, pp. 253–280, 1949.
[143] G. Benchetrit, S. A. Shea, T. P. Dinh, S. Bodocco, P. Baconnier, and A. Guz, "Individuality of breathing patterns in adults assessed over time," *Respirat. Physiol.*, vol. 75, no. 2, pp. 199–209, Feb. 1989.
[144] F. Lin, C. Song, Y. Zhuang, W. Xu, C. Li, and K. Ren, "Cardiac scan: A non-contact and continuous heart-based user authentication system," in *Proc. 23rd Annu. Int. Conf. Mobile Comput. Netw.*, Oct. 2017, pp. 315–328.
[145] A. Ragman, V. M. Lubecke, O. Boric-Lubecke, J. H. Prins, and T. Sakamoto, "Doppler radar techniques for accurate respiration characterization and subject identification," *IEEE J. Emerg. Sel. Topics Circuits Syst.*, vol. 8, no. 2, pp. 350–359, Jun. 2018.
[146] S. M. M. Islam, A. Rahman, N. Prasad, O. Boric-Lubecke, and V. M. Lubecke, "Identity authentication system using a support vector machine (SVM) on radar respiration measurements," in *Proc. 93rd ARFTG Microw. Meas. Conf. (ARFTG)*, Jun. 2019, pp. 1–5.
[147] S. M. M. Islam, A. Sylvester, G. Orpilla, and V. M. Lubecke, "Respiratory feature extraction for radar-based continuous identity authentication," in *Proc. IEEE Radio Wireless Symp. (RWS)*, Jan. 2020, pp. 119–122.

ABOUT THE AUTHORS

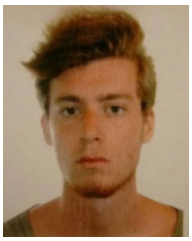

Giacomo Paterniani received the B.S. degree in biomedical engineering from the University of Bologna, Bologna, Italy, in 2018, and the M.S. degree (cum laude) in electronic engineering from the University of Modena and Reggio Emilia, Modena, Italy, in 2021.

Currently, he is enrolled as a Research Fellow in "vital signs monitoring" at the University of Modena and Reggio Emilia. His main research interests lie in the area of frequency-modulated continuous-wave (FMCW) radars, with an emphasis on the development of novel detection and estimation algorithms for vital signs estimation.

Giorgio Guerzoni received the B.S. and M.S. degrees in electronic engineering from the University of Modena and Reggio Emilia, Modena, Italy, in 2016 and 2018, respectively, where he is currently working toward the Ph.D. degree in information and communication technology.

His main research interests lie in the areas of multiple-input–multiple-output (MIMO) radars and machine learning, with an emphasis on the development of novel detection and estimation algorithms.

Daria Sgreccia graduated (cum laude) from the School of Medicine, University of Bologna, Bologna, Italy, in 2015. She completed her training and fellowship (cum laude) in cardiology at the University of Modena and Reggio Emilia, Modena, Italy.

She is currently a Cardiologist at the Cardiology Division, University Hospital of Modena, Modena. She is involved as a Research Fellow at the Cardiology Division, Department of Biomedical, Metabolic and Neural Sciences, University of Modena Reggio Emilia. Her scientific activity is mainly devoted to clinical management, epidemiology, physiopathology of cardiac arrhythmias, particularly atrial fibrillation, and atrial signal monitoring.

Pasquale Di Viesti (Graduate Student Member, IEEE) received the bachelor's and master's degrees (cum laude) in electronic engineering from the University of Modena and Reggio Emilia, Modena, Italy, in 2016 and 2018, respectively. He is currently working toward the Ph.D. degree in automotive for intelligent mobility at the University of Bologna, Bologna, Italy.

He is currently a Postdoctoral Research Fellow with the University of Modena and Reggio Emilia. His main research interests lie in the area of statistical signal processing and multiple-input–multiple-output (MIMO) radars.

Alessandro Davoli (Graduate Student Member, IEEE) received the B.S. and M.S. degrees (cum laude) in electronic engineering from the University of Modena and Reggio Emilia, Modena, Italy, in 2016 and 2018, respectively. He is currently working toward the Ph.D. degree at the University of Bologna, Bologna, Italy, with a focus on automotive for intelligent mobility.

He is currently a Postdoctoral Research Fellow with the University of Modena and Reggio Emilia. His main research interests lie in the area of multiple-input–multiple-output (MIMO) radars, with an emphasis on the development of novel detection and estimation algorithms for automotive applications.

Anna Chiara Valenti graduated (cum laude) from the School of Medicine, University of Rome, Rome, Italy, in 2015. She completed her training and fellowship (cum laude) in cardiology at the University of Modena and Reggio Emilia, Modena, Italy.

She is currently a Cardiologist at the Cardiology Division, University Hospital of Modena. She is involved as a Research Fellow at the Cardiology Division, Department of Biomedical, Metabolic and Neural Sciences, University of Modena Reggio Emilia. Her scientific activity is in mainly devoted to clinical management, epidemiology, physiopathology of cardiac arrhythmias, and particularly atrial fibrillation.

Marco Vitolo graduated from the School of Medicine, University of Turin, in 2015, and he completed his training and fellowship in cardiology at the University of Modena and Reggio Emilia, Modena, Italy.

Since January 2020, he has become a Research Fellow of the Liverpool Centre for Cardiovascular Science, University of Liverpool. He is currently a Cardiologist at the Cardiology Division, University Hospital of Modena, Modena. His scientific activity is mainly focused on cardiac arrhythmias and clinical electrophysiology, particularly on atrial fibrillation. He is actively involved in clinical research as subinvestigator of several international randomized clinical trials and multicenter international prospective registries on atrial fibrillation and cardiac arrhythmias.

Prof. Vitolo is a member of national and international scientific societies, such as the European Society of Cardiology (ESC), the European Heart Rhythm Association (EHRA), and the Italian Association of Arrhythmology and Cardiac Pacing (AIAC).

Giorgio M. Vitetta (Senior Member, IEEE) received the Dr.Ing. degree (cum Laude) in electronic engineering and the Ph.D. degree from the University of Pisa, Pisa, Italy, in 1990 and 1994, respectively.

He holds the position of Full Professor of Telecommunications at the University of Modena and Reggio Emilia since 2001. His main research interests lie in the broad areas of wireless and wired data communications, localization systems, multiple-input–multiple-output (MIMO) radars, and the smart grid. He has coauthored more than 100 papers published on international journals and the proceedings of international conferences, and has coauthored the book *Wireless Communications: Algorithmic Techniques* (John Wiley, 2013).

Dr. Vitetta has served as an Area Editor for IEEE TRANSACTIONS ON COMMUNICATIONS and an Associate Editor of IEEE WIRELESS COMMUNICATIONS LETTERS and IEEE TRANSACTIONS ON WIRELESS COMMUNICATIONS.

Giuseppe Boriani graduation in medicine (cum laude) from the University of Bologna, Bologna, Italy, in 1984, and the Ph.D. degree in cardiovascular physiopathology from the University of Milan, Milan, Italy, in 1993.

He is currently a Full Professor of cardiovascular diseases at the University of Modena and Reggio Emilia, Modena, Italy. He is also the Director of the Post-graduate School in Cardiology and the Director of the Course for Cardiocirculatory Physiopathology and Cardiovascular Perfusion Techniques, University of Modena and Reggio Emilia. Previous representative of the European Heart Rhythm Association (EHRA) and the European Society of Cardiology (ESC) from 2013 to 2016 within the European Network for Health Technology Assessment (EUNEHTA) promoted by the European Community. He is ranked in EXPERTSCAPE (https://expertscape.com/) a worldwide score of experts based on scientific publications in the last ten years (as per February 12, 2022): Expert in Artificial Pacemakers: # 1 in the worldwide rank; Expert in Cardiac Resynchronization Therapy: # 5 in the worldwide rank; and Expert in Implantable Defibrillators: # 5 in the worldwide rank. He is included in the Top 2% Scientists list, published by Stanford University, after analysis of a database that contains 160 000 names selected from 8 000 000 researchers who stand out worldwide for scientific authority based on the number of publications and citations in the relevant subject areas. Scientific activity is mainly devoted to arrhythmias and use of electronic devices (implantable or wearables) for cardiac monitoring, clinical electrophysiology, heart failure, cardiomyopathies, clinical cardiology, pharmacoeconomics, clinical pharmacology of antiarrhythmic agents and antithrombotics, and monitoring of the arrhythmic effects of the drugs used in oncology and health economics.

Open Access funding provided by 'Università degli Studi di Modena e Reggio Emilia' within the CRUI CARE Agreement